Design and Investigation of Microelectromechanical (MEMS) Varactors

Dissertation

zur Erlangung des akademischen Grades
Doktor der Ingenieurwissenschaften
(Dr.-Ing.)
der Technischen Fakultät
der Christian-Albrechts-Universität zu Kiel

Maxim Shakhray

Itzehoe
2005

1. Gutachter	Prof. Dr. Anton Heuberger
2. Gutachter	Prof. Dr. Helmut Foell
Datum der mündlichen Prüfung	02.05.2005

This thesis is dedicated
to all my teachers from Russia and Germany
and to my wife.

Acknowledgements

In the chronological order, first I would like to thank Prof. Dr. Helmut Foell, who gave me the idea to perform my PhD study at Fraunhofer ISiT. This idea came to realisation by a kind permission of Prof. Dr. Anton Heuberger. I am grateful to Both Mr. Heuberger and Mr. Foell, as they agreed to be *Gutachter* for my thesis.

My sincerest gratitude goes to Dr. Thomas Lisec. Without his constant help and support through the whole time I have spent at ISiT, this thesis would hardly come into the world. The same applies to Christoph Huth, who helped me a lot with measurement instrumentation and whom I owe my present ability to speak and write in German.

Dr. Manfred Weiss provided me with fruitful discussions of theoretical issues and helped me with simulation. Dr. Helmut Bernt was very kind to read the preliminary version of the thesis and to offer significant suggestions about it.

Finally, I would like to express my gratitude to my colleagues Dr. Bernd Wagner, Lothar Schmidt, and Mikhail Gruschko for their kind help and discussions.

Table of Contents

1. Introduction.

In this section general importance of the topic will be described, along with the basic information about varactors.

1.1 RF MEMS Overview

In the recent years wireless communication has led to an explosive development of consumer and military applications of radio frequency (RF), microwave and millimetre wave circuits and systems. Applications include wireless personal (hand-held) communication systems such as mobile phones, wireless local area networks (WLANs), satellite communications and automotive radar. Future hand-held and ground communications systems as well as communications satellites will require very low weight, volume and power consumption in addition to higher data rates and increased functionality. Increasing the level of integration, improvements in size have been achieved. Currently, in a mobile phone, all active functions are already integrated, also in the RF front-end with 3–4 radio frequency integrated circuits (RFICs) per terminal on average. Today, continuing integration and chip scaling can only marginally influence the size reduction [1-3]. Moreover, in spite of many years of research, the IC industry is facing a technological barrier to further miniaturisation. Nowadays, a situation has been reached when the presence of rather bulky expensive off-chip (or discrete) passive RF components, such as high-*Q* inductors, capacitors, varactor diodes and ceramic filters, plays a limiting role in further size reduction. Passive components are essential in RF systems and are used for matching networks, LC tank circuits (in voltage controlled oscillators - VCOs), attenuators, power dividers, filtering, switching, decoupling purposes and as reference resonators. On-chip passive components, fabricated along with the active elements as part of the semiconductor wafer in various RFIC technologies such as BiCMOS, SiGe and GaAs, did not result in components with the required high-quality factors offered by the off-chip passives [4].

Particularly troublesome is the absence of on-chip counterparts for more specific off-chip passives. For example, in the RF front-end of heterodyning transceivers, this concerns very high-*Q* (>10 000) quartz crystal reference resonators, high-*Q* ceramic and surface acoustic wave (SAW) filters, high-*Q* varactor diodes and to some extent the PIN diode or FET switches. For these components, an on-chip version or an on-chip alternative solution with the same functional characteristics is not readily available or simply unrealisable and therefore non-existent. Until now, passive components remain the most important obstacle in integration and miniaturisation of wireless communication systems. This in particular becomes apparent after inspection of the printed wiring boards (PWBs) in state-of-the-art wireless communication systems. It is found that a large portion of the board area is occupied by the off-chip passives. In a typical cell phone for instance, 90–95% of the total number of components are passive components, taking up 80% of the total transceiver board area, and being responsible for 70% of the cost [4]. Reduction of the space taken up by the passives is achieved by using very small discrete passive components, by integrating passive components (either on-chip or off-chip) [3, 5-6] or by implementing novel transceiver architectures in which fewer passives are needed [7-8]. Integration of the standard fixed passives as resistors (R), capacitors (C), inductors (L), transmission lines (T-lines), and their combinations such as LC-type filters, couplers, power dividers and modulators, is already under development for over a decade. Additional advantage is expected from an extension of the existing library of fixed passives with variable passives as switches, varicaps and tunable filters. In addition, there is a need to integrate miniaturised high-*Q* resonators and filters to replace the bulky

SAW and ceramic (dielectric resonator) filters and probably also the quartz- crystal reference resonators. Perhaps the only technology at present with the potential to enable the integration of all these passives is micromachining or MEMS (micro-electro-mechanical system or structure) technology [9-10]. When applying MEMS to high-frequency circuits (radio frequency, microwave or millimetre wave), the technology is commonly referred to as RF MEMS [11]. RF MEMS is currently under development in laboratories around the world and offers the potential to build a multitude of miniaturised components such as switches, tunable capacitors (varactors), high-*Q* inductors, film bulk acoustic resonators (FBAR), dielectric resonators, transmission line resonators and filters, and mechanical resonators and filters. Research on RF-MEMS continues at both the device level and the system level. The use of MEMS technology opens new perspectives for various wireless applications to achieve integrated solutions for improving performance, compactness and also cost. MEMS technology may revolutionise the choices made in the architecture of transceiver systems and/or radar antennas.

1.2 Varactor Applications

Varactors find several applications in RF systems, of which the most frequently cited is in RF VCOs. Other applications include tuneable matching networks, tuneable filters, loaded-line phase-shifters. We will dwell on VCO here. An RF VCO plays a key role in modulation and demodulation processes in a wireless transceiver (e.g. a mobile phone). In the reception mode the VCO is used to convert the high-frequency incoming signal to a low-frequency band, where the further signal processing techniques are applied to extract the desired information, for example human voice or data. In the transmission mode it performs the opposite function, transferring the low frequency information onto a high-frequency carrier. In Fig. 1-1 [12] a schematic structure of a heterodyne RF receiver front-end, including an RF VCO, is shown.

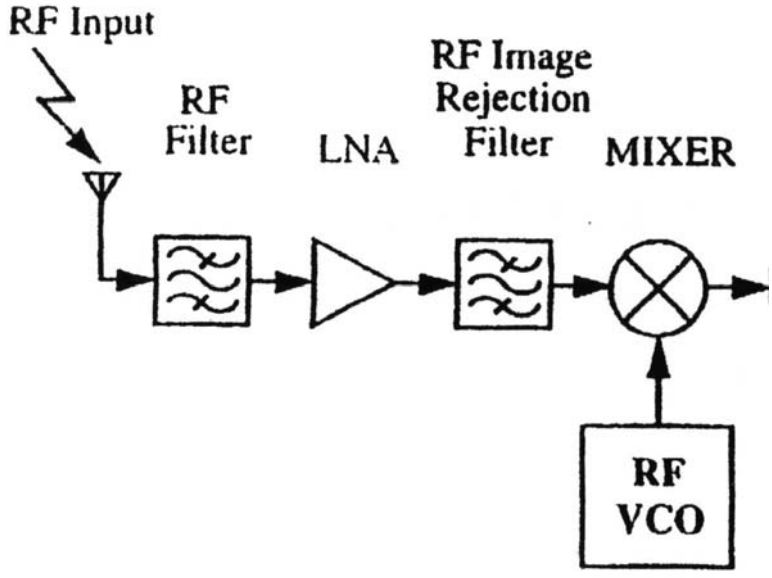

Fig. 1-1. Schematic of a receiver front-end (part) [12]

After filtering, amplifying and again filtering, the received signal passes through a mixer, where demodulation takes place. The carrier frequency to be subtracted is generated in an RF

VCO. There exist three types of VCOs suitable for integration [13]. These are LC-oscillators, ring oscillators, and relaxation oscillators (multivibrators). Among them only LC-oscillators are close to fulfil the phase noise requirements stated for high performance wireless applications. An LC resonator usually consists of an inductor (with inductance L) and a varactor (with variable capacity C_V), as shown in Fig. 1-2. [12]

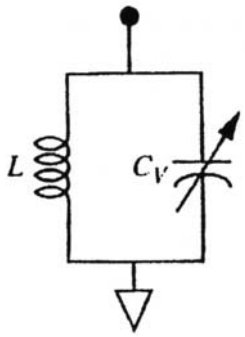

Fig. 1-2. LC-resonator (tank), including a varactor, as RF VCO [12]

Two principal VCO characteristics are the tuning range and the phase noise. The tuning range defines the bandwidth – a set of working frequencies of the transceiver. The tuning range can be defined as $(f_{max} - f_{min})/f_C$, where f_{max} is the maximum frequency achievable with the VCO, f_{min} - the minimum frequency achievable with the VCO, and f_C – the carrier frequency of the signal. The resonance frequency of the VCO shown in Fig. 1-2 is expressed in Eq. 1.1:

$$f = \frac{1}{2\pi\sqrt{LC_v}} \qquad (1.1)$$

One can see that the tuning range is determined by the variation of the varactor capacity. The minimum tuning range of an RF VCO needed for a common wireless application is typically a small fraction of the carrier frequency, around 3%. For example, the GSM-900 standard covers 890 MHZ to 915 MHz. However, manufacturing limitations would introduce device and parasitics mismatch, resulting in a shifted oscillator output frequency. To overcome this problem, either a trimming technique is required or the VCO tuning range needs to be widened, reaching about 5% of the carrier frequency. This is a so called narrow-band VCO. Tuning range of a wide-band VCO comprises 10 and more per cent of the carrier frequency.

In addition to VCO tuning range, the phase noise performance is another key parameter for high-performance communication systems because the phase noise of an oscillator would ultimately determine the selectivity of a wireless transceiver, i.e., the ability to receive one particular channel of interest in the presence of neighbouring interferers. An ideal VCO produces a single peak in its power spectrum, with the entire output power concentrated at the centre frequency, which can be tuned through an external controlling voltage source. However, in reality a VCO output signal has a power spread in the vicinity of the centre frequency causing non-zero spectral width. Fig. 1-3 [12] presents a typical oscillator output power spectrum.

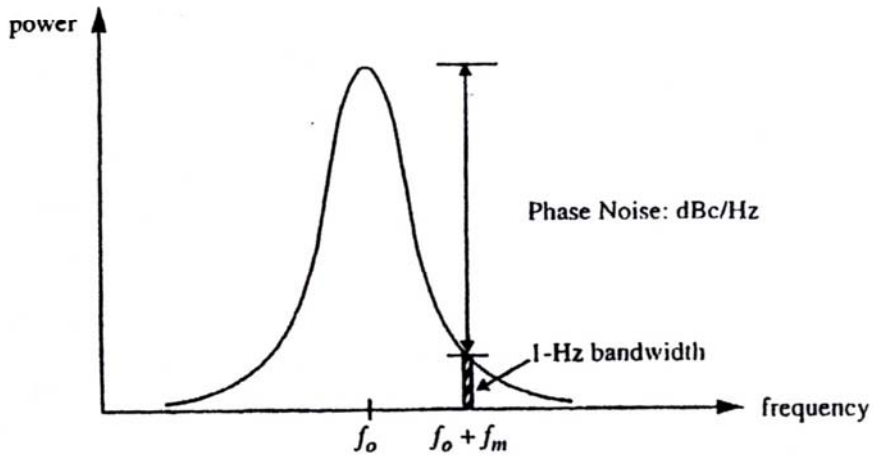

Fig. 1-3. Typical VCO power spectrum [12].

The frequency f_m is an offset frequency from the oscillator centre frequency f_0. Phase noise is usually specified in dBc/Hz at a given offset frequency, where dBc refers to the noise power level in dB relative to the carrier power. Hence, an oscillator phase noise at a given offset frequency can be found from the ratio of the noise power in a 1-Hz bandwidth to the carrier power. In Fig. 1 this will be the ratio of the rectangle area with 1-Hz bandwidth at the offset frequency f_m to the carrier power at f_0. The phase noise of an LC-resonator can be expressed as

$$L(f_m) = \frac{FkT}{2Q^2 P_{rf}} \left(\frac{f_0}{f_m} \right)^2, \qquad (1.2)$$

where F is the device excess noise factor, kT – the thermal power, Q – the quality factor of the loaded resonator, P_{rf} – the oscillator RF output power, f_0 – the oscillator centre frequency, f_m – the offset frequency of interest. Among these parameters Q is the most important, because it is squared. The resonator quality factor is defined by the quality factors of the components it contains, i.e., of the inductor and the varactor [12].

1.3 Varactor Main Characteristics

There are several possible characteristics of a varactor, among which two are considered the most important (as we saw in section 1.2): capacity ratio C_r, which is the ratio between the maximum and minimum capacities achievable with a certain varactor,

$$C_r = \frac{C_{\max}}{C_{\min}} \qquad (1.3)$$

and quality factor Q, which represents RF losses in the varactor. By definition, the quality factor of a varactor or any other passive component is [13]

$$Q = 2\pi \frac{\left| E_{C,\max} - E_{L,\max} \right|}{E_{dis}}, \qquad (1.4)$$

where $E_{C,max}$ is the maximum capacitive energy stored in the varactor, $E_{L,max}$ – the maximum inductive energy stored in the varactor, E_{dis} - the energy dissipated per cycle, when a sinusoidal signal (voltage or current) is assumed to be applied to the component. From Eq. 1.4 it is seen that as losses are included in the denominator, a large Q is desirable. If a varactor is operated far below the self resonance frequency, which is normally the case, the stored inductive energy is negligible, and Eq. 1.4 reduces to

$$Q = 2\pi \frac{E_{C,\max}}{E_{dis}} \qquad (1.5)$$

If a varactor is modelled as an ideal capacitor with a resistor in series (which gives general understanding to the first approximation), than the quality factor can be expressed as

$$Q = \frac{1}{R_S \cdot \omega \cdot C_S}, \qquad (1.6)$$

where R_S is the ideal resistance in series with capacity, $\omega = 2\pi f$ – the angular frequency of the applied signal, and C_S – the ideal capacity in series. Obviously, smaller resistance is required to obtain a higher quality factor. Since Q depends on frequency, the quality factor is normally defined for a certain frequency or a range of frequencies. A more general model includes a combination of the already presented series model with the parallel model, where the ideal capacity is connected with its parasitic resistance in parallel.

Typical numerical values will be given in the following sections. Other varactor characteristics include CV-curve, absolute capacity, actuation voltage, and self-resonance frequency.

1.4 Semiconductor Varactors and MEMS Perspective

At present, mass-production takes advantage of semiconductor varactors, where the capacity is changed with the width of the depletion region. They can be divided into off-chip and on-chip ones. Actually, the only off-chip varactor used is the varactor diode. On-chip varactors include pn-junctions and MOS varactors. When compared, off-chip varactor diodes generally allow for higher quality factor values, but are bulkier. On the contrary, the on-chip varactors are compact but often possess lower Q values.

For example, Tilmans et al. [4] report a varactor fabricated in 0.5 micron CMOS technology with Q = 5 at 4 GHz and a varactor fabricated in 0.35 micron BiCMOS technology with Q = 20 at 4.7 GHz. At the same time Q values of at least 40 are expected from off-chip discrete varactors. Comparison of several CMOS varactors can also be found in [13] (Table 1-1). According to [14], semiconductor varactors presently achieve capacity ratios between 4 and 6, and Q values of up to 100 for frequencies between 0.5 and 5 GHz.

The quality factor values achieved with on-chip semiconductor varactors are often considered insufficient, whereas off-chip varactors might pose difficulties for miniaturisation of the newly developed systems. MEMS varactors are considered prospective because of their

ability to achieve high *Q* values of 100 to 400 at the frequencies of interest thanks to the use of highly conductive materials [14]. While varactors based on pn-junction can be only used with one polarity (reverse bias), MEMS varactors take advantage of both polarities. They also can be inexpensively produced on Si, glass or ceramic substrates.

Varactor Type	**CMOS Process**	**Layout**	C_r	Q_{min}
pn-junction	0.5 μm	Single-ended quadratic p^+	1.3	110
	0.5 μm	Single-ended rectangular p^+	1.4	50
	0.5 μm	Balanced rectangular p^+	1.4	83
MOS Standard Mode pMOS	0.5 μm	Balanced l_g = 0.5 μm	1.7	18
MOS Accumulation Mode nMOS	0.5 μm	Single-ended $l_{g,eff}$ = 1.95 μm	3.4	10
	0.35 μm	Single-ended	1.8	15
	0.5 μm	Balanced l_g = 0.5 μm	2.0	43

Table. 1-1. Performance of different CMOS varactors at 2 GHz*.

*) Included performance data are originally measured at different frequencies (1-2.5 GHz), but have subsequently been projected to 2 GHz to enable a comparison (the quality factor is assumed to be inversely proportional to frequency, the capacity ratio is assumed to be independent of the frequency). The capacity ratio corresponds to 1.8-2 V tuning voltage range. l_g is the drawn gate length, $l_{g,eff}$ – the effective gate length [13].

1.5 Aim of the Work

The aim of the present work was mostly formulated within the MELODICT project [15]. In essence, the goal was to design and investigate surface-micromachined electrostatically driven MEMS varactors with continuous capacity change based on Ni as structural material. The specifications were also set in MELODICT project: continuous capacity change with capacity ratio C_r between 1.3 and 10. It is obvious from comparison with the capacity ratio data of semiconductor varactors (section 1.4), that the upper target – the capacity ratio of 10 - is a very ambitious aim.

2. State of the Art

In this section the most important developments in the field of MEMS varactors will be presented.

2.1 Continuous Capacity Change and Actuation Mechanisms

In MEMS varactors any of the parameters from

$$C = \frac{\varepsilon_0 \varepsilon A}{d} \qquad (2.1)$$

can be varied depending on the varactor type. Thus, there are varactors based on a variation of the dielectric media between the plates [16], on a variation of the overlapping plates area [17-18], and on a variation of the gap between the plates [19-23]. To realise this, various actuation principles employed in MEMS technology are used. The most popular among them are the electrothermal drive [24], the piezoelectric drive [25], and the electrostatic drive (which is most widely used) [16, 19-23]. Electrothermal and piezoelectric drives allow to achieve good values of the tuning ratio (2.7 [24], 3.1 [25]) and of the quality factor (200-300 at 10 GHz [24], 210 at 1 GHz [25]) and a linear CV-characteristic. However, these actuation types consume power and their switching time is normally larger than that for the electrostatic drive. Additionally, their design and technology are normally more complicated.

Below only varactors with electrostatic drive will be considered, since they were the target of the investigation.

2.2 Variation of the Effective Dielectric Constant

This rather exotic function principle was described in [16]. Fig. 2-1 presents conceptual and perspective-view schematic of the tuneable capacitor design.

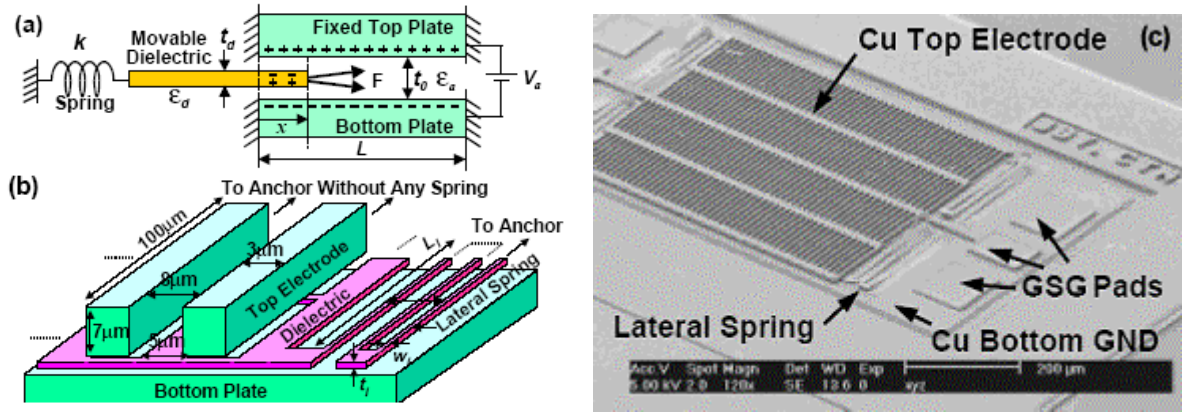

Fig. 2-1. Varactor with variable dielectric. Conceptual schematic (a) and actual structure with lateral spring (b). SEM photo of the fabricated device (c) [16].

As shown, the structure features a bottom capacitor plate fixed to the substrate, and a top capacitor plate suspended above the former, but rigidly anchored to the substrate, and unable

to move. Both plates are constructed of copper to minimise their total series resistance, and thus maximise the device *Q*. A dielectric slab is suspended between the two plates and anchored to the substrate outside the two plates via spring structures. This dielectric is free to move, and can be electrostatically displaced to alter either the overlap between it and the capacitor plates, or the fringing fields between them. In the former case, when a DC bias is applied between the two plates, the charges on the capacitor plates exert an electrostatic force on the induced charges in the dielectric, which pull the dielectric into the gap, as shown in Fig. 2-1 (a).

The authors also point out that the vertical motion of the dielectric (which was not designed initially) offers a respectable amount of capacitance change as well (Table 2-1). Tuning in this mode is due to fringing fields between the asymmetrical metal-to-dielectric gaps (and not due to dielectric variation).

Working mode	**C_{max}/C_{min}**	**Q (frequency)**	**$Q_{converted}$ (at 2 GHz)**
Lateral	1.077	291 (1 GHz)	146
Vertical	1.4	218 (1 GHz)	109

Table 2-1. Main characteristics of the varactor with variable dielectric in two working modes.

The dielectric constant variation principle is also used in thin-film (non-MEMS) ferroelectric-based varactors described in [26-28]. In such varactors one uses the ability of ferroelectrics ($BaTiO_3$, $PbTiO_3$, $Ba_xSr_{1-x}TiO_3$ [26, 28], $SrTiO_3$ [27]) to change their dielectric constants in response to applied voltage. A varactor reported in [28] reaches a capacity ratio of 3.4 (no quality factor was reported).

2.3 Plate Area Variation

This varactor type is represented by the comb-drive varactors (Fig. 2-2 [4]).

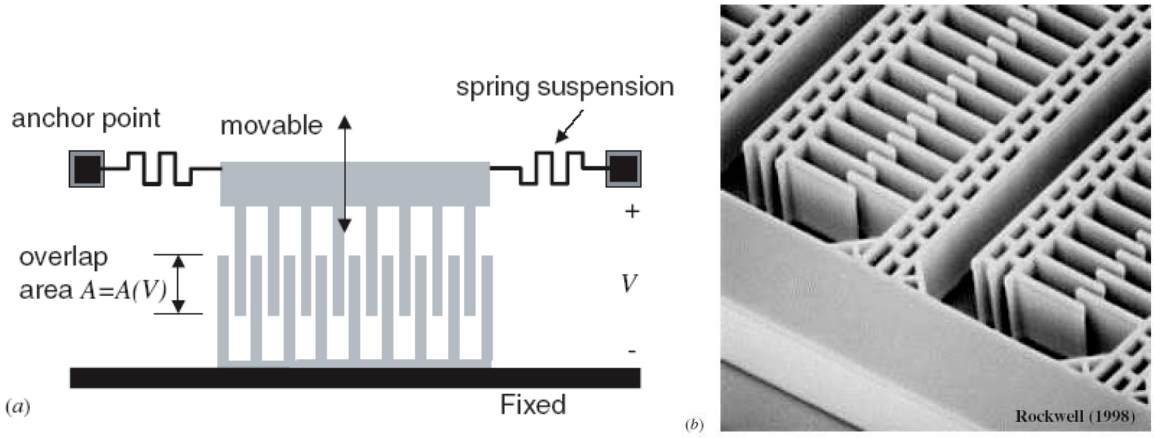

Fig. 2-2. Varactor based on plate area variation (comb-like varactor). Schematic representation of the top-view (a) and SEM photo of a practical implementation (b) from Rockwell Science Center [4]

One of the combs is fixed whereas the other one can move towards it and back [17, 29] or parallel to it (up and down) [Seok, Choi, Chun]. As the movable comb changes its position,

the overlap area of the comb fingers also changes, which leads to a change in capacity. Usually such varactors are made of silicon with the help of deep reactive ion etching (DRIE). Since the resistance of silicon is comparatively high, quality factors of the varactors are not large. Metallic constructions generally have higher quality factors. However, to produce metallic comb-drive varactors one needs use of LIGA or a similar high aspect ratio lithography method (which is quite expensive and not readily available in an average lab), because vertical structure dimensions are larger than horizontal ones. To improve the quality factors, researchers deposit metallic layers on top of silicon structures. Main characteristics of several comb-like varactors are given in the Table 2-2.

Varactor type	**C_{max}/C_{min}**	**Q (frequency)**	**$Q_{converted}$ (at 2 GHz)**
[17] (lateral)	3	34 (0.5 GHz)	8.5
[29] (lateral)	8.4	36 (2 GHz)	36
[18] (vertical)	1.1	4 (2 GHz)	4

Table 2-2. Main characteristics of several comb-drive varactors.

One can immediately see the improvement of the *Q* value from pure silicon [18] to Al-metallised silicon [17, 29]. There is no theoretical limit of the capacity ratio for comb-like varactors. The practical limitations are imposed by the springs tensibility and the lateral instability of the moving comb which makes it stick to the fixed comb. An important advantage of comb-like varactors is flexibility in absolute capacity value. It can be easily varied with the number of fingers used.

2.4 Gap Variation

This kind of MEMS varactors usually has a movable membrane (fixed at one or two ends) and one or several electrodes actuating it (they also can play a role of the second capacitor plate or a signal line) and is very similar to a MEMS switch in design. It is often called a parallel-plate varactor. Schematic of a MEMS varactor, where the membrane is fixed at both ends (fixed-fixed membrane as opposed to cantilever membrane) is shown in Fig. 2-3.

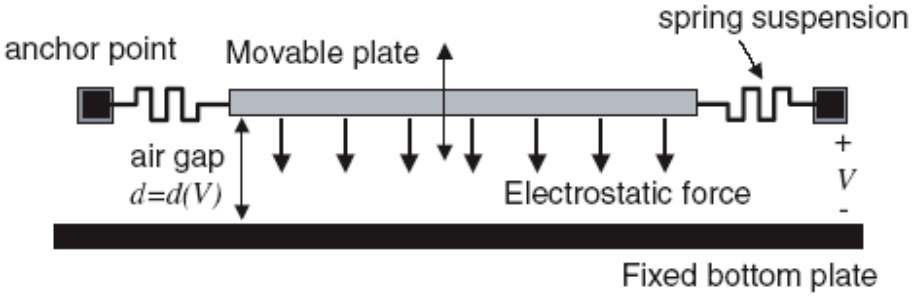

Fig. 2-3. Schematic side-view illustrating the working principle of a fixed-fixed membrane varactor [4]

As the voltage between the membrane and the electrode below is increased, the membrane starts deflecting (bending in reality, as it is fixed at both ends) towards the electrode. During this step the electrostatic force and the restoring mechanical force are in equilibrium. This equilibrium exists, however, only if the gap between the membrane and the electrode is larger than 2/3 of the initial gap (for details see section 4.2.1). As soon as the gap gets smaller (and simultaneously the applied voltage overcomes a certain threshold), the pull-in occurs and the

membrane falls onto the electrode. If now we start to decrease the voltage, the membrane will not return to the initial position at once, but will stay on the electrode till the voltage reaches another threshold. Thus the membrane behaviour (and also capacity behaviour with respect to the applied voltage) is described with a hysteresis curve. A simulated CV hysteresic curve is shown in Fig. 2-4.

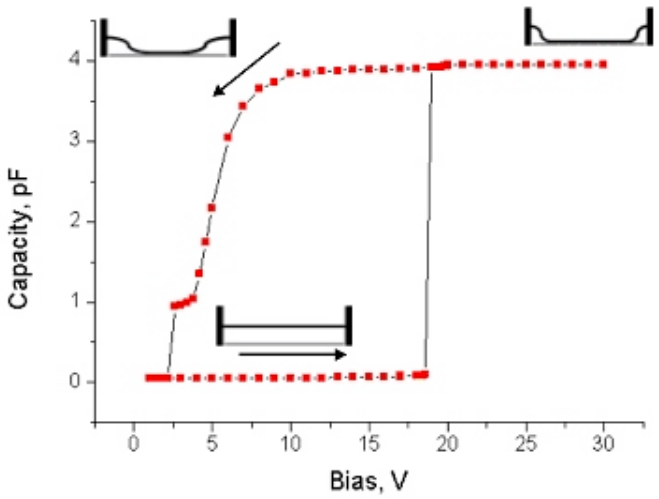

Fig. 2-4. Simulated CV hysteresic curve of a varactor with variable gap [30]. The small schematics show the corresponding positions of the membrane.

One can see that the capacity decreases gradually as the voltage is decreased. This is due to the fact that the membrane bends rather than always stays flat, i.e. it gradually detaches from the underlying electrode. There exist two voltage ranges where equilibrium of forces is maintained and continuous change of the capacity is possible: below the first threshold (so called pull-in voltage) and above the second threshold (so called release voltage). Both of them are used to achieve capacity change needed in a varactor.

If “the upper third” of the gap between the membrane and the electrode (i.e., the direct path of the hysteresis) is used, then the theoretical tuning range is limited to 50% of the initial capacity (tuning ratio 1.5). In order to increase the range, several designs were proposed. A two-level membrane, for instance [21], where the central part of the membrane is situated closer to the sensing electrode than the side parts which are attracted downwards by the electrodes (no voltage is applied to the sensing electrode, Fig. 2-5). One third of the larger gap d_2, which the membrane can travel without a pull-in, can be made equal or even larger than the central gap d_1. Thus the centre of the membrane can travel the whole gap height without a pull-in.

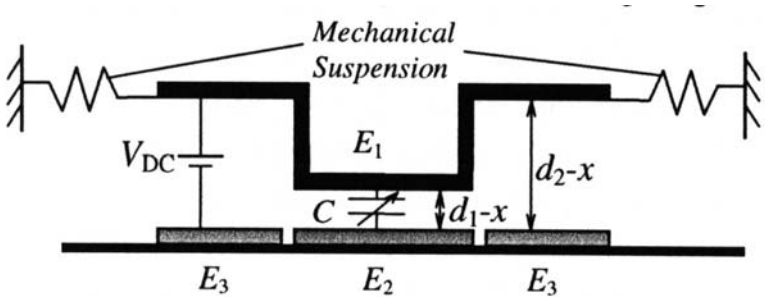

Fig. 2-5. Schematic side-view of a modified parallel-plate varactor using “the upper third” [21].

A similar principle is used in [19], where the signal line (which plays the role of the second capacitor plate) is situated closer to the flat membrane than the side electrodes which actuate the membrane (Fig. 2-6).

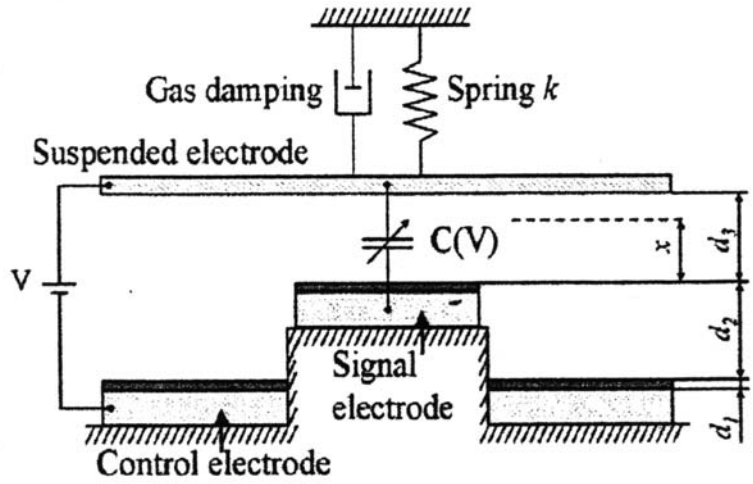

Fig. 2-6. Schematic side-view of a modified parallel-plate varactor using “the upper third” [19]

In [20] the authors suggested a three-plate varactor, where electrodes are situated not only beneath, but also above the movable membrane. There is still only 1/3 of the lower gap, which can be travelled without a pull-in, but additionally there is 1/3 of the upper gap, which also can be travelled without a pull-in (Fig. 2-7).

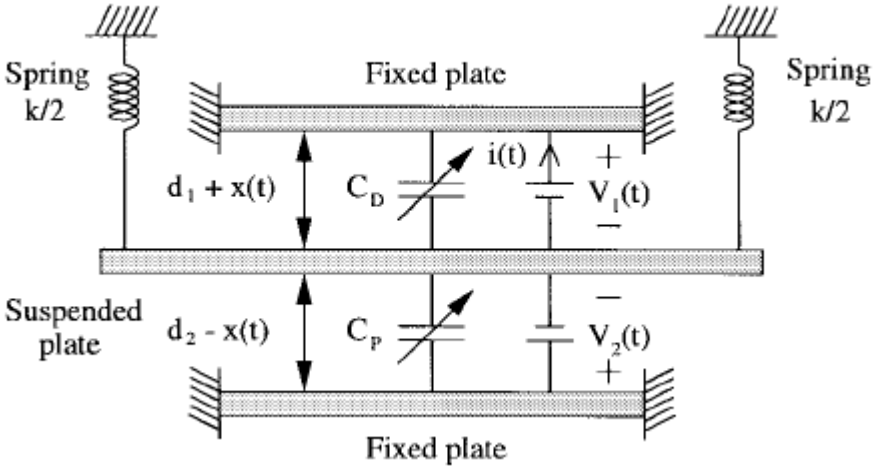

Fig. 2-7. Schematic side-view of a modified parallel-plate varactor using “the upper third” [20]

When using the reverse path (“back-curve”) of the hysteresis one often speaks of an S-shape varactor. Such a varactor with a membrane fixed at one side (a cantilever-type varactor) is described in [22] (Fig. 2-8).

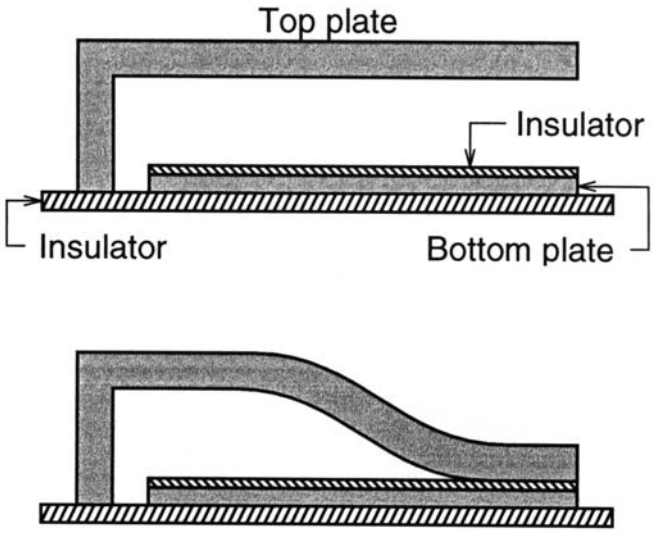

Fig. 2-8. Schematic side-view of a cantilever S-shape varactor using “the back-curve” in free state (top) and after pull-in (bottom). Membrane forming S-shape can be seen [22]

After the free end of the membrane goes through pull-in, the membrane obtains an S-shape (Fig. 2-8). With increasing voltage an increasing part of the membrane becomes gradually attached to the underlying electrode (being separated by a dielectric layer). The achievable capacity ratio is defined by two lengths: maximum attachment length (can be approximated by the whole membrane length, since lateral membrane dimensions are usually much larger than the gap) and minimum attachment length (or detachment length, since smaller length will lead to complete release of the membrane to the initial position). For a simulation of the detachment length one usually uses numerical methods.

Below the main characteristics of the varactors described above are given (Table 2-3). One can easily see the difference in quality factors between the two types of materials – polysilicon and metals. The quality factor of the varactor number 3 is several times larger than those of polysilicon structures. Losses which correpond to decrease of the quality factor originate not only from the varactor itself, but also from the silicon substrate on which the varactor and signal line are situated. Authors in [19] report that they managed to increase the quality factor up to 119 by removing the substrate from beneath the signal line. The supporters of the polysilicon structures emphasise, however, that polysilicon is advantageous for integration of the MEMS structures with active microelectronics and seek ways to raise the quality factor (most often through deposition of a metal layer (e.g. Au) upon the polysilicon layer).

	Varactor type	**C_{max}/C_{min}**	**Q (frequency)**	**$Q_{converted}$ (at 2 GHz)**
1	One-gap parallel-plate varactor [20] (poly-Si)	1.5	20 (1 GHz)	10
2	Two-level membrane varactor [21] (permalloy)	1.698		-
3	Two-level electrode varactor [19] (Au)	2.25	53 (2 GHz)	53
4	Three-plate varactor [20] (poly-Si)	1.87	15.4 (1 GHz)	7.7
5	S-shape varactor [22] (poly-Si)	1.46	6.5 (1.5 GHz)	4.875

Table 2-3. Main characteristics of varactors with variable gap.

An array of switches can also be used as a varactor, and a certain switching voltage will activate an individual pull-in. For instance, in [31] switching voltages in the array are determined by stiffness of the springs which depends on their width (Fig. 2-9). The authors report attaining a tuning ratio of 4 at a quality factor 140 at 0.75 GHz ($Q_{converted}$ = 52.5 at 2 GHz). The relatively high quality factor is due to the choice of the membrane material - Au. However, with this approach only a quasi-continuous capacity change can be achieved.

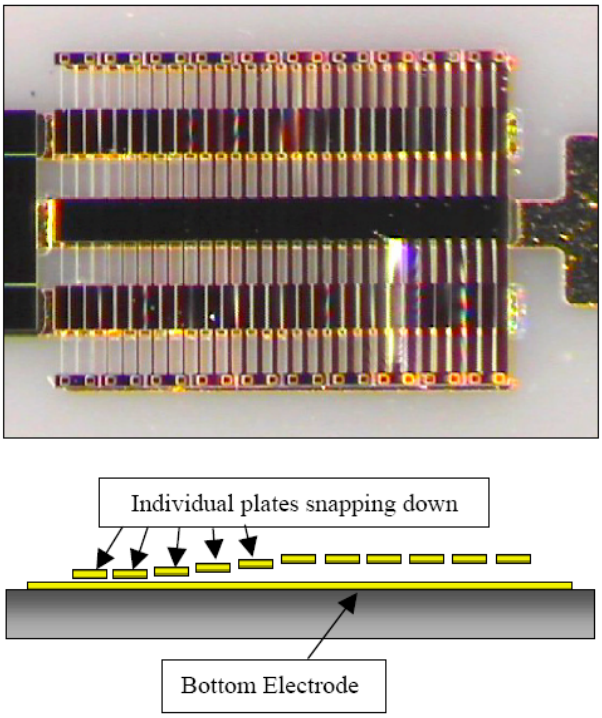

Fig. 2-9. Top-view (top) and schematic cross-section illustrating the working principle of a switch array-based MEMS varactor [31]

3. Technology and General Design Principles

The technology used to manufacture the varactors in the work and design principles common for all varactor types presented further are described in this section.

3.1 Technology

The technology used was adopted from an already existing process, which was developed for the fabrication of RF MEMS switches. The process is based on Ni as structural material, Cu sacrificial layers and wet release etching (Fig. 3-1).

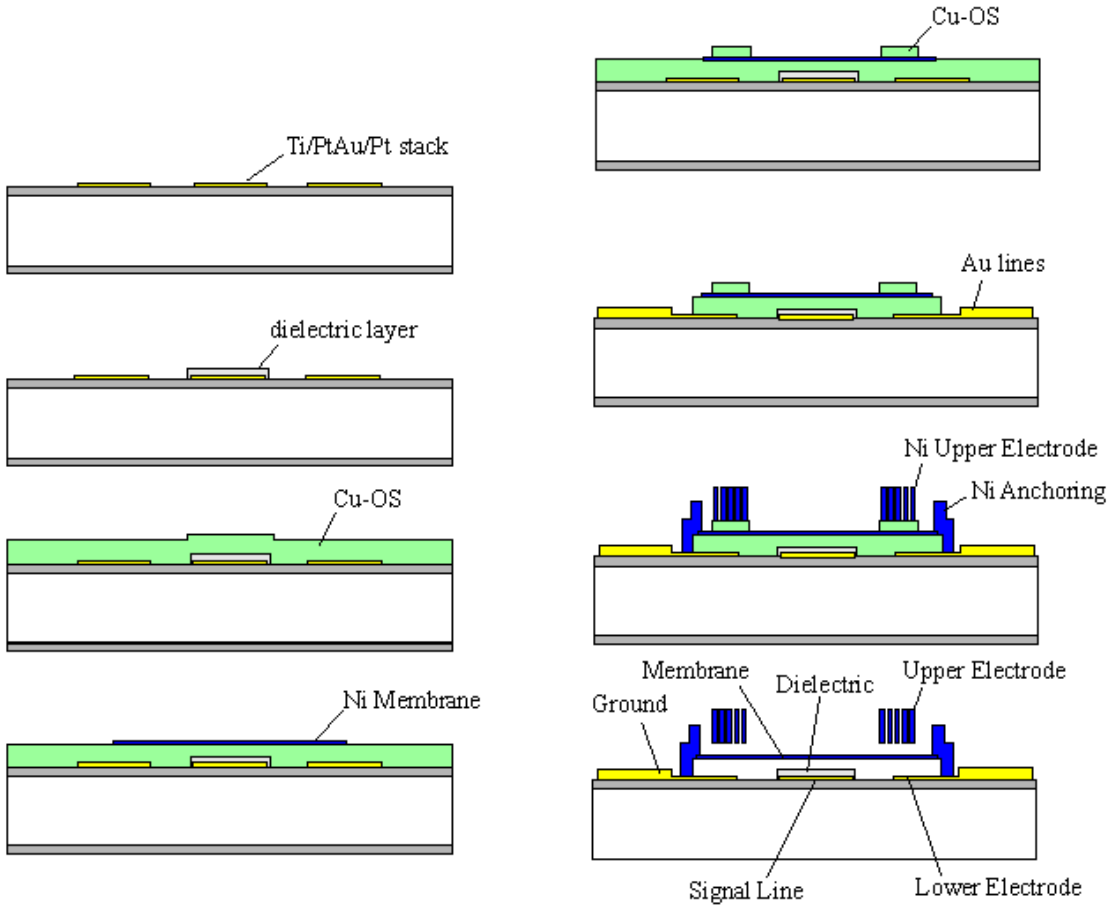

Fig. 3-1. Technology used in the investigation (left column top to bottom, then right column top to bottom)

The process starts with an oxidised silicon wafer. Silicon oxide must isolate the varactors from the conductive silicon substrate. In the next step, a thin highly conductive metal stack is deposited to form underpath - signal lines (fixed capacitor plates) and ground lines, and lower electrodes (if needed). Then a dielectric layer is deposited upon the signal line to prevent short-circuit between the movable membrane and the signal line (it is necessary in case of S-shape varactors, but optional in case of parallel-plate varactors). A copper sacrificial layer is deposited and polished. In the next step a Ni membrane is deposited on top of the sacrificial layer. Optionally, a second sacrificial layer is deposited on top of the membrane (required for three-plate parallel-plate varactors). Then the sacrificial layers are structured and a thick gold layer is deposited to form contact pads and strengthen the lines. A thick Ni layer is deposited

in one step to form suspensions for the membrane (anchoring) and upper electrodes (if needed). Finally, the sacrificial layers are etched away to result in a free-standing structure. The whole process requires 8 masks. It is important to notice that the presented process is a low-temperature one. The step with the highest temperature is the dielectric deposition, which takes place at 300-400°C. This enables integration of the devices with CMOS circuitry. Some details are summarised in the Table 3-1 below.

Substrate	Silicon Resistivity > 3 kOhm/cm 675 μm single-side polished or 508 μm thick double-side polished
Oxide	Thermal oxide 2 μm
Underpath	Ti/Pt/Au/Pt stack Evaporation and lift-off Lift-off
Dielectric layer	100-200 nm PE-Si_3N_4 structured by RIE
Sacrificial layer 1	Up to 3 μm evaporated Cu CMP polishing Wet etching
Sacrificial layer 2	Electroplated Cu Wet etching
Membrane	Electroplated Ni Ti/Au plating base
Thick gold	Electroplated
Suspensions and upper electrodes	Electroplated Ni

Table 3-1. Technology details.

3.2 General Design Principles

Before describing the design of certain structures, common design principles will be given. They include a bridge-like design, typical for varactors based on gap variation principle (Fig. 3-2), special suspension structures, and perforation patterns.

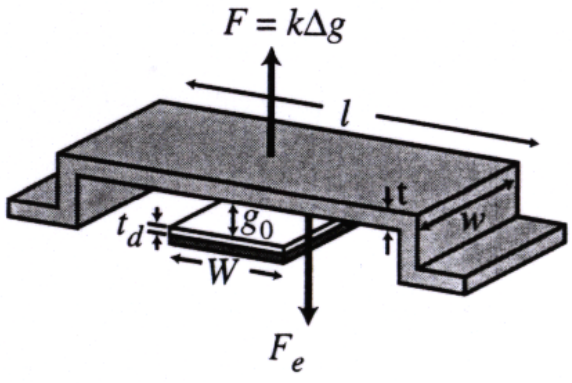

Fig. 3-2. Schematic view of a bridge-like structure typical for varactors based on gap variation principle [14] (see section 5.2 for notation and details)

The suspension structures (Fig. 3-3) are aimed at compensating thermal stress arising during various heating processes in fabrication and packaging. One sees a schematic top-view of a part of a varactor membrane adjacent to the support and the support itself.

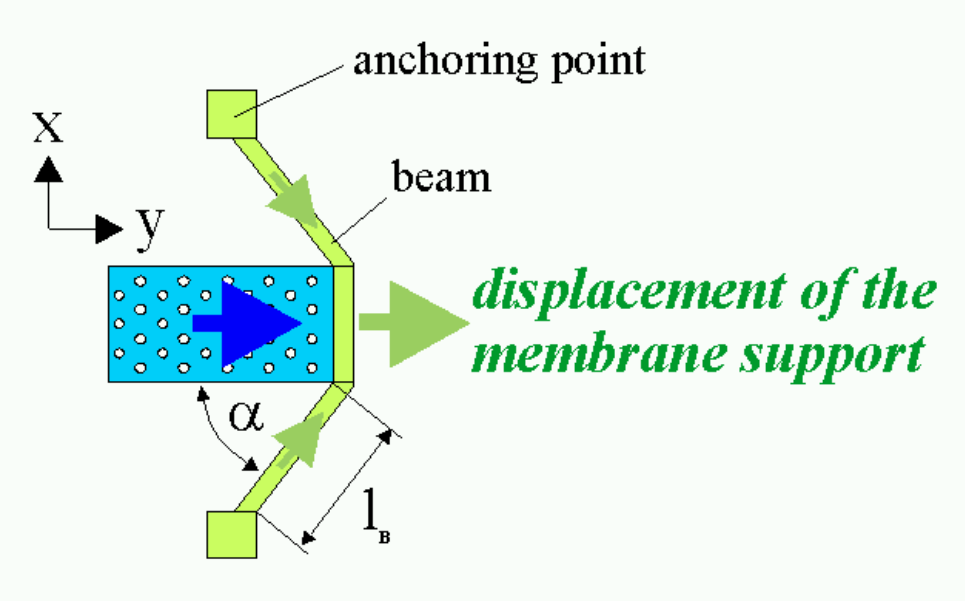

Fig. 3-3. Schematic top-view of special suspension structure used in the investigation. Adjacent part of the membrane with perforation pattern is also shown.

The suspension consists of two anchoring posts (points) and three sections (one central and two beams) and can be characterised by the beam length l_B and the angle α between the beam and the membrane. When heating takes place, thermal expansion results in compressive stress in a membrane, if both ends of the membrane are laterally fixed. The presented suspension however is also subject to thermal expansion, and the latter expansion is supposed to compensate the stress in the membrane. The suspension used in our investigation has l_B = 122 μm and α = 49°.

In Fig. 3-3 one can also see the perforation pattern used in design of all investigated devices. They are shown as white spots in the blue membrane area. The holes reduced the Ni surface to about 82% of the initial area. The main purpose of perforation holes is to allow for faster release etch since they enlarge the contact surface of the to be etched sacrificial layer. They also reduce the squeeze film damping and increase the switching speed of MEMS devices [14]. See section 5.2.4 for further details about perforation holes. Apart from the membrane, perforation was also used in upper electrodes – again for effective etching purposes. Perforation holes in the upper electrodes are situated exactly above such holes in the membrane, but have larger diameter.

4. Measurement Techniques

The varactors produced were investigated by two types of experiments: optical measurements and low-frequency measurements (10 kHz). We had no opportunity to perform high-frequency measurements (several GHz), therefore no data for quality factors of the varactors are available. But they are supposed to be high due to the highly conductive Ni used as a structural material.

4.1 Optical Measurements

The optical measurements were performed with help of a white-light interferometer and a voltage source. The voltage was supplied to a varactor under investigation through manipulators, which had needles at the ends, as can be seen in Fig. 4-1. The wafer and the manipulators were fixed on a metallic plate with help of scotch tape and magnets, respectively.

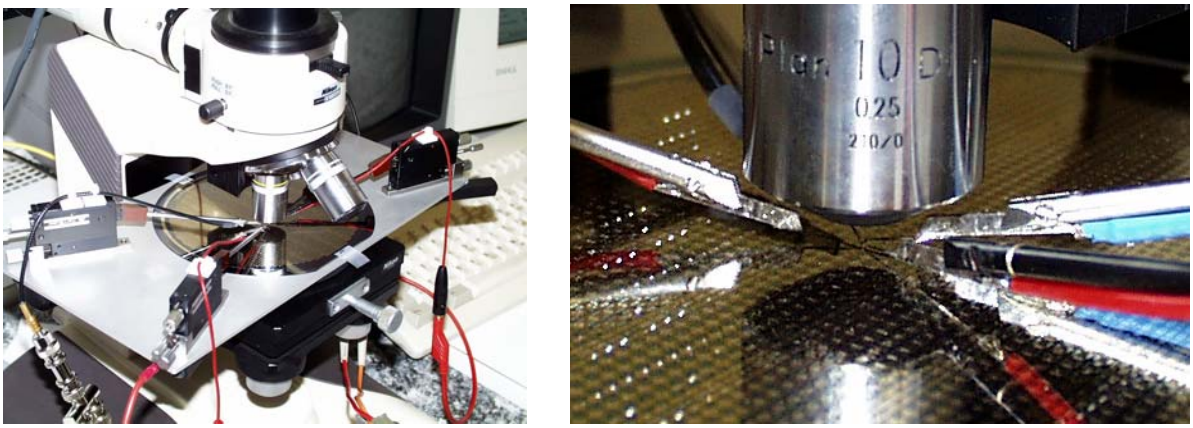

Fig. 4-1. View of the optical measurement setup (left) and zoomed view of the manipulator hands ending with needles (right).

When a voltage from the voltage source was fixed, the interferometer allowed us to obtain a profile of the movable membrane. In Fig. 4-2 one can see a screenshot of the interferometer software with the membrane profile and the varactor top-view (this is how the interferometer „sees“ the varactor)

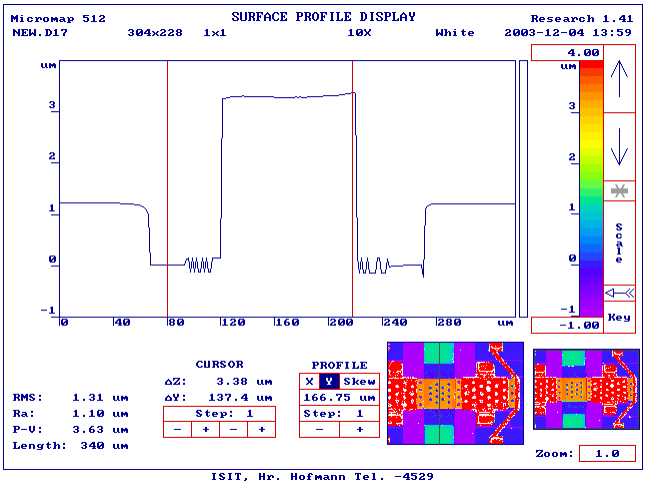

Fig. 4-2. Screenshot of the interferometer software during measurement.

From the profile one can read the height of the membrane above the signal line (two red level lines in Fig. 4-2). Averaged height forms a point on the height-voltage plot. After several measurements at different voltages one can plot a height-voltage graph for a certain varactor, as shown in Fig. 4-3.

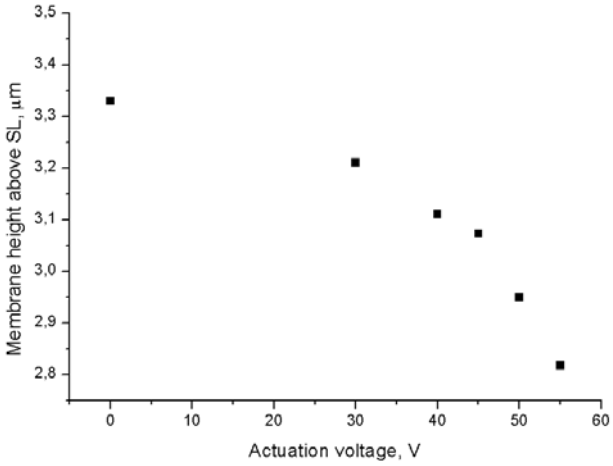

Fig. 4-3. Height-voltage plot as a result of series of optical measurements.

Such a plot can be fitted with a theoretical height-voltage curve according to the model.

The voltage could be tuned up to 110 V DC with resolution of up to 0.1 V. The height could be measured with a resolution of about 10 nm. The accuracy was spoilt by noise of about ±25 nm, but it could be corrected through simultaneous measurement of the membrane height next to the suspension, where no height change was expected. Each measurement took several minutes, which put a limitation on the density of experimental points. Most of the height change falls onto the high voltage region – close to the collapse, thus more points were measured there. To measure the collapse voltage, one needs to collapse the membrane, which might defect the varactor. Reasons for the latter can be dielectric charging (described in section 5.5.3) or even burning after the touchdown. The setup also allowed us to measure the capacity with an LCR-meter (see section 4.2) simultaneously with optical measurements.

4.2 Low-Frequency Measurements

The measurements were performed on a standard Suess microprober complemented with a voltage source and a HP LCR-meter. The wafer was vacuum-fixed on a movable chuck. Voltage and probing RF signal were supplied through manipulators with needles at the ends, as shown in Figs. 4-4, 4-5. Microscope and video-camera provided visual observation of the measured devices through oculars and on a display.

Fig. 4-4. View of the Suess microprober used for low-frequency measurements. Microscope and a video-camera are mounted above the wafer-holder.

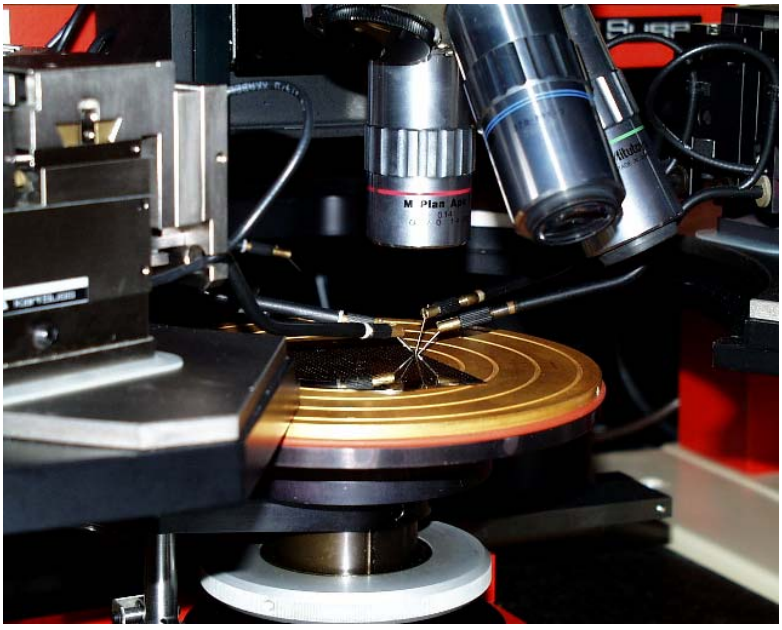

Fig. 4-5. Zoomed view of manipulator hands ending with contact needles. Microscope lenses are seen above the wafer-holder.

The LCR-meter measured the capacity of the varactor. The result of the measurement was a CV-curve, as shown in Fig. 4-6.

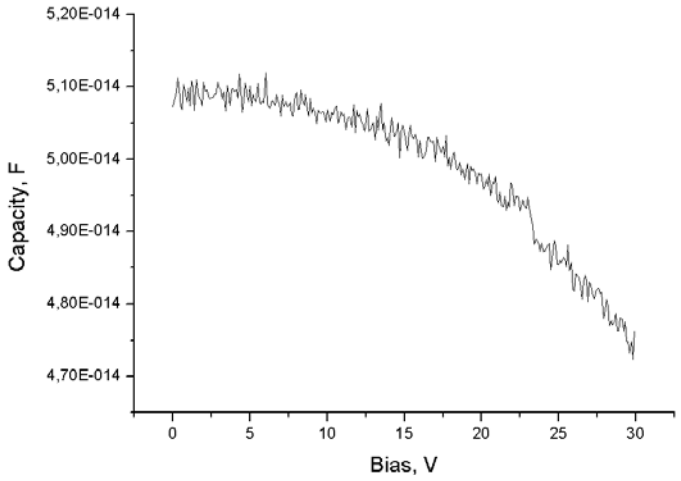

Fig. 4-6. CV-curve as a result of a low-frequency measurement.

The measurements were performed on-wafer at the frequency of the probing signal of 10 kHz. The range of frequencies was limited by the LCR-meter used to 20 Hz – 1 MHz. The choice of the frequency was set by the accuracy from one side (at lower frequencies the accuracy gets worse) and the voltage-dependent capacitive behaviour of the substrate from the other side (at higher frequencies capacity change induced by the substrate was comparable to the capacity change induced by the varactor). As an example, at 100 kHz the capacitive behaviour of the varactor showed polarity dependence. Additionally, capacity was observed to vary with light intensity.

The observed capacitive behaviour of the substrate is due to the Si-oxide-metal stack present. To get rid of these effects, we lowered the frequency down to 10 kHz. At this frequency parasitic capacity variation (with light and applied voltage) was negligible (it was checked on dummy structures, without a varactor bridge). The resolution of the low-frequency measurements was better than 0.5 fF, and the accuracy was about ±1 fF.

In all measurements performed with parallel-plate varactors (see section 5.2.3), a low-frequency signal of 1 V effective amplitude (equivalent to 1 V DC) was used. For S-shape varactor measurements, the amplitude of the low-frequency signal was varied between 1 and 20 V (maximum amplitude possible with the LCR-meter).

5. Parallel-Plate Varactor

Design, modelling, experimental results and discussion of the problems regarding the parallel-plate varactor will be given in this section.

5.1 Design

Two principles were utilised for the design of the parallel-plate varactor. First, the three-plate configuration (described in section 2.4, Fig. 5-1) had to improve the capacity ratio of the varactor in excess of the theoretical 1.5 limit.

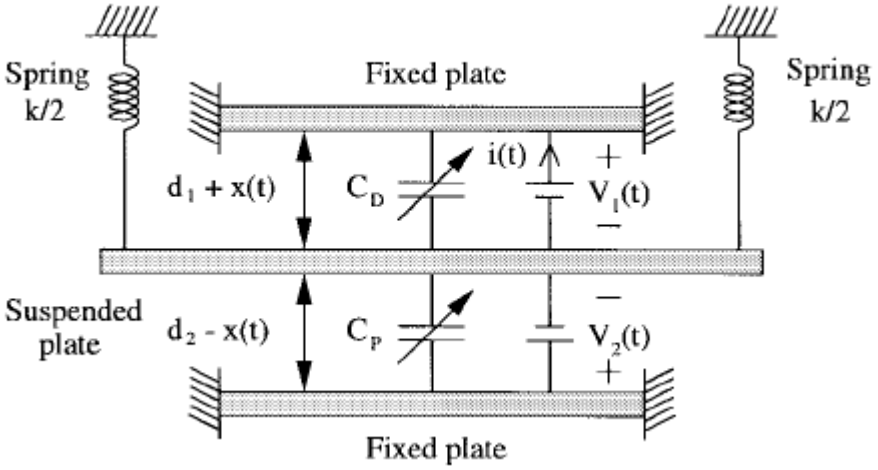

Fig. 5-1. Schematic side-view of a modified parallel-plate varactor using “the upper third” [20]

Second, use of electrodes situated beneath the ends of the membrane had to result in so called leveraged bending effect, described in [32] (Fig. 5-2). This effect should lead to large membrane deflection in the middle, where the capacity is sensed in our case. In this way the capacity ratio had to be further increased.

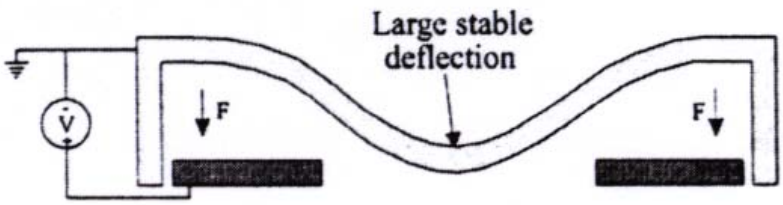

Fig. 5-2. Schematic side-view of a MEMS bridge with side electrodes demonstrating the leveraged bending effect [32]

Side-view schematic of the designed parallel-plate varactor can be seen in Fig. 5-3. A movable membrane is suspended with the help of two posts (the suspension structure is not depicted for sake of simplicity) between two sets of electrodes. There are two side electrodes

situated below the membrane. They must pull the membrane down electrostatically, if bias is applied to them (force is shown with red arrows), whereas the membrane is grounded. The capacity is sensed by the central electrode, which forms the second varactor plate. All of them are covered with dielectric to prevent short-circuit upon contact after pull-down (although the structure is not supposed to reach pull-in, it normally takes place in testing, since the complete CV curve is desirable). Apart from them, there are two upper side electrodes, which must pull the membrane upwards.

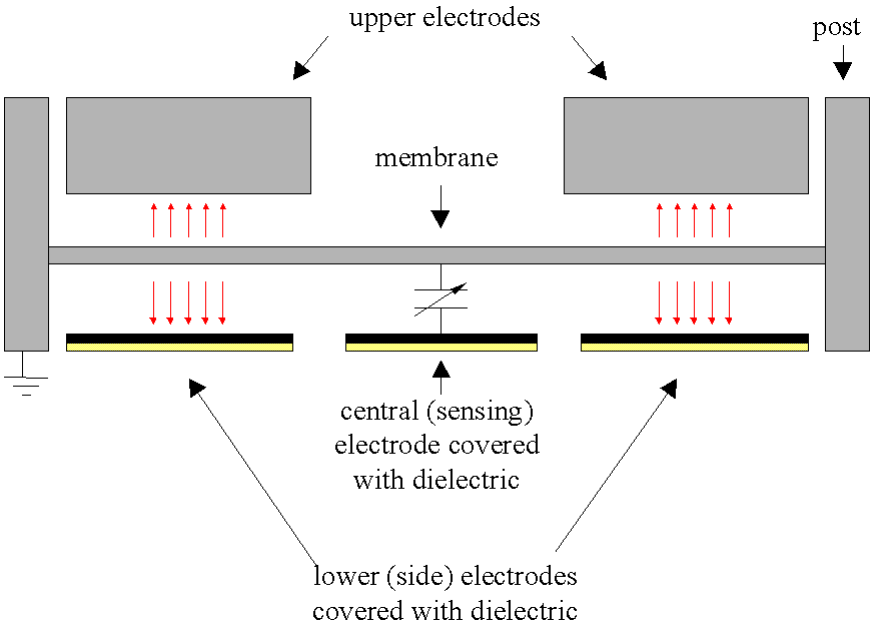

Fig. 5-3. Side-view schematic of the designed parallel-plate varactor.

Geometric and material parameters for the basic configuration are given in Table 5-1. Theoretical capacity ratio for this configuration is 1.9.

Membrane	Thickness	1 μm
	Length	500 μm
	Width	100 μm
	Perforation hole diameter (ligament efficiency)	10 μm (0.642)
	Young's modulus (Ni)	170 GPa
Central electrode	Width*	100 μm
	Dielectric thickness	200 nm
	Dielectric constant (Si_3N_4)	7.5
	Gap	2.5 μm
Lower side electrodes	Length**	132 μm
	Gap	2.5 μm
Upper side electrodes	Length***	150 μm
	Gap	2 μm
	Perforation hole diameter	14 μm

Table 5-1. Geometric and material parameters for the basic parallel-plate varactor configuration

*) as the electrode is actually a part of the signal line situated perpendicular to the membrane, the important geometric parameter is called “width”
**) width of the electrode corresponds to the membrane width; end of the electrode is situated exactly below the membrane’s fixed end
***) width of the electrode corresponds to the membrane width; there is a 25 μm gap between the electrodes and the suspension structures

SEM photo of a fabricated parallel-plate varactor is shown in Fig. 5-4.

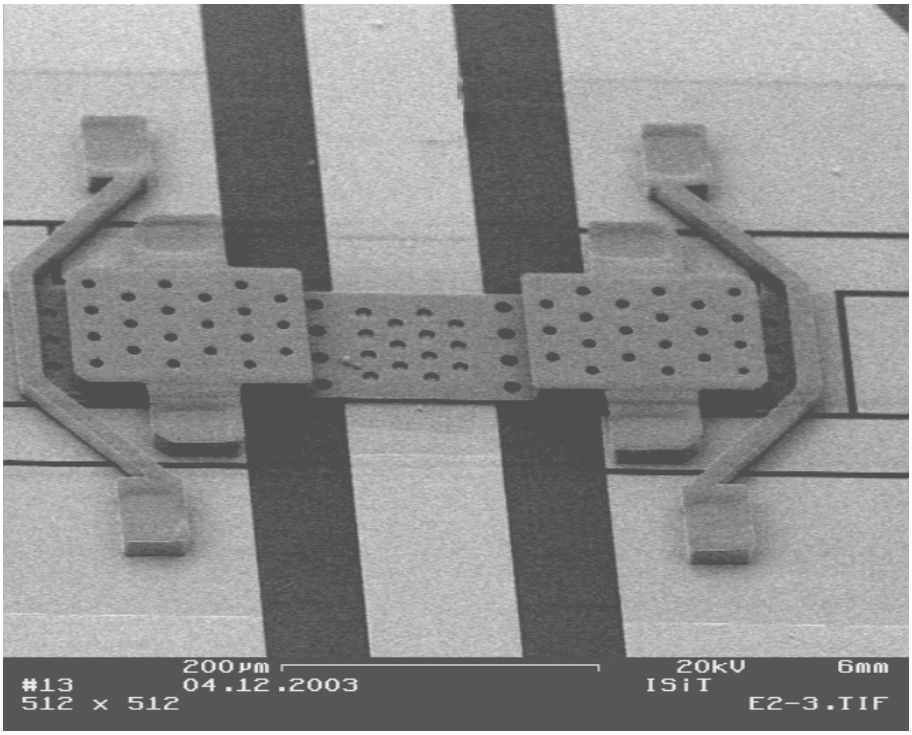

Fig. 5-4. SEM photo of a fabricated parallel-plate varactor in basic configuration.

Thick upper electrodes above the membrane are visible. They are fixed on the substrate with posts on either side of the electrodes. Suspension structures are fixed with similar posts.

Due to non-homogeneity of the deposition processes over a wafer, the following thickness values were measured on manufactured devices (Table 5-2)

	Designed, μm	**Measured range, μm**	**Average, μm**
Lower gap	2.5	2.3÷2.7	2.56
Membrane	1	0.9÷1.2	0.96
Upper gap	2	1.9÷2.1	2.05
Dielectric	0.2	0.18÷0.2	0.19

Table 5-2. Comparison of the designed and manufactured thickness values.

5.2 Analytical model

The aim of the model is to predict the CV-curve for a certain varactor configuration. Modelling a bridge-like MEMS varactor with electrostatic drive can be divided into two main parts: the mechanical part (where mechanical reaction to an arbitrary force is considered) and

the electrical part (where electrostatic force is specified). Sometimes the mechanical part is considered first [14], which might be not intuitive. Thus, we will consider the electrical part first. Finally, case studies will be presented .

5.2.1 Electrical part

In Fig. 5-5 one can see a 3D schematic of a bridge-like MEMS varactor (or a switch, which is actually the same). The membrane (of length *l*, width *w*, and thickness *t*) is suspended on two posts above an actuating electrode (of width *W*) covered (which is optional in case of varactors) with dielectric (of thickness t_d). The gap between the membrane and the dielectric is g_0. If a potential difference is applied between the membrane and the electrode, the electrostatic force F_e pulls the membrane down. The electrostatic force is counteracted with mechanical force as a membrane reaction to deformation.

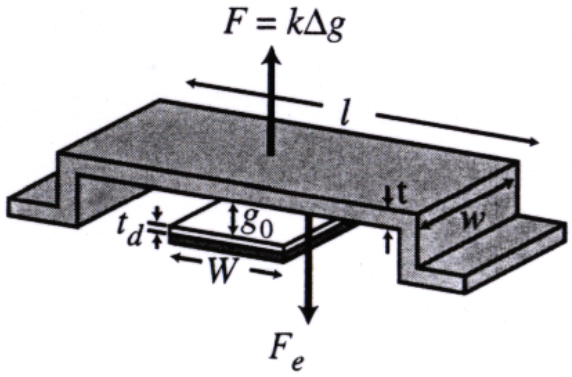

Fig. 5-5. Parallel-plate device in consideration [14]

The aim of the consideration is to find a dependence between the voltage (or potential difference between the electrode and the membrane, since the membrane is usually grounded) and the position of the membrane. To do so we will write the force equation for equilibrium

$$F_e + F_{mech} = 0\,, \qquad (5.1)$$

where F_{mech} is a mechanical restoring force. The mechanical force is described by Hooke's law

$$F_{mech} = k\Delta g\,, \quad (5.2)$$

where k is the linear spring constant (which is to be found in the mechanical part), and Δg – vertical deflection of the membrane. Let us first consider a homogeneous dielectric between the plates (i.e., unlike in Fig. 5-5, only air, for instance, and no other dielectric layer on the electrode), so that $\Delta g = (g_0 - g)$, where g_0 is the initial gap between the membrane and the underlying electrode, and g – actual gap between the membrane and the electrode when the membrane is deflected. To describe the electrostatic force we first will consider the energy of a capacitor [33].

$$W_e = \frac{C(\Delta\varphi)^2}{2} = \frac{\varepsilon_0 \varepsilon A V^2}{2g}, \qquad (5.3)$$

where C is the capacity, $\Delta\varphi$ and V - the potential difference between the plates, ε_0 – permittivity of vacuum, ε - permittivity of the dielectric between the plates, A – area of the plates, and g – gap between the plates. For simplicity one and the same gap between the membrane and the electrode is assumed over the whole area contributing to the capacity. This is a good approximation when the actuating electrode is situated beneath the centre of the membrane, whereas for the case of side electrodes the approximation is not valid, as we will see later (indeed, the beam ends always stay fixed, whereas other points deflect). The electrostatic force acting on the plates of a capacitor is a spatial derivative of the energy

$$F_e = \frac{\partial}{\partial g} W_e = \frac{\partial}{\partial g}\left(\frac{\varepsilon_0 \varepsilon A V^2}{2g}\right) = -\frac{1}{2}\frac{\varepsilon_0 \varepsilon A V^2}{g^2}. \quad (5.4)$$

Now we can get back to the force equilibrium equation

$$F_e + F_{mech} = -\frac{1}{2}\frac{\varepsilon_0 \varepsilon A V^2}{g^2} + k(g_0 - g) = 0 \quad (5.5)$$

$$\frac{1}{2}\frac{\varepsilon_0 \varepsilon A V^2}{g^2} = k(g_0 - g) \quad (5.6)$$

$$V = \sqrt{\frac{2k}{\varepsilon_0 \varepsilon A} g^2 (g_0 - g)} \quad (5.7)$$

Unfortunately, the dependence between the gap and the voltage is non-linear and allows a simple form only for *V(g)*. When plotted, the height-voltage dependence looks like shown in Fig. 5-6 [14].

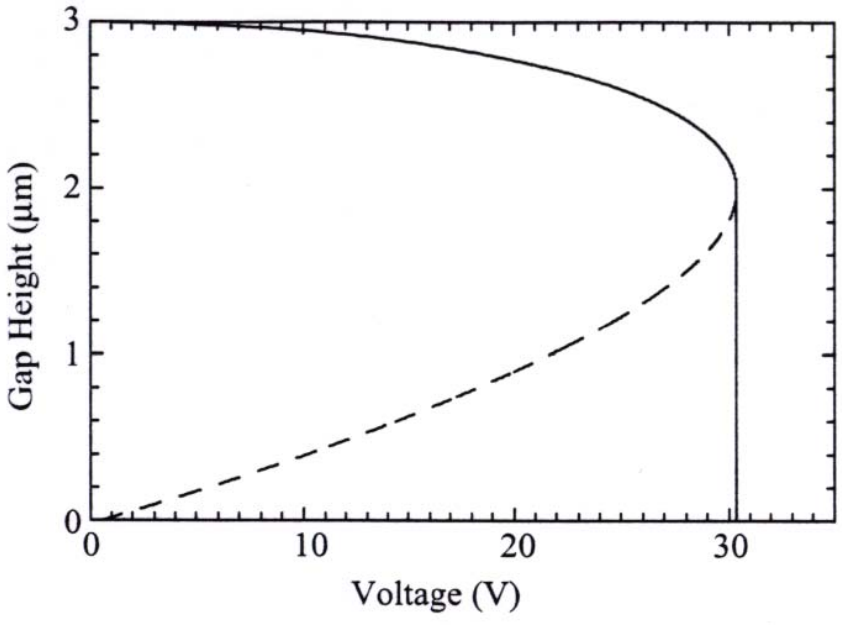

Fig. 5-6. Theoretical height-voltage curve for a parallel-plate device [14]

One can see that at a certain height the derivative of V by g becomes zero. Simple calculation shows that it happens when the gap is 2/3 of the initial value. At this height the equilibrium between the forces holds no more, since the electrostatic force rises faster that the mechanical one, and collapse (or pull-down) takes place: the membrane falls down to the underlying electrode. Knowing the initial height, one can calculate the pull-down voltage as follows

$$V_{pull-down} = V(2/3g_0) = \sqrt{\frac{8k}{27\varepsilon_0 A} g_0^3} \quad (5.8)$$

If a dielectric layer of thickness t_d and dielectric constant of ε is added into the model (and the rest of the gap between the plates - g - is filled with air), the formulae change as follows

$$C = \frac{\varepsilon_0 A}{g + \frac{t_d}{\varepsilon}}$$

$$F_e = -\frac{1}{2}\frac{\varepsilon_0 A V^2}{\left(g + \frac{t_d}{\varepsilon}\right)^2} \quad (5.9\text{-}5.12)$$

$$V = \sqrt{\frac{2k}{\varepsilon_0 A}\left(g + \frac{t_d}{\varepsilon}\right)^2 (g_0 - g)}$$

$$V_{pull-down} = V\left(\frac{2}{3}g_0 + \frac{1}{3}\frac{t_d}{\varepsilon}\right) = \sqrt{\frac{8k}{27\varepsilon_0 A}\left(g_0 + \frac{t_d}{\varepsilon}\right)^3}$$

The unknown quantity, as was already noticed, is the spring constant *k*. We will find it in the mechanical part of the consideration.

5.2.2 Mechanical part

There are at least two approaches to find the spring constant needed to describe the deflection of the membrane. The first one is based on beam equations from Landau and Lifshitz [34] and the second one was presented by Rebeiz in [14] with reference to [35]. Both give similar results, which only differ in coefficients when intrinsic stress is included. The first method will be only briefly reviewed here according to [30]. All the calculations were performed according to the method presented by Rebeiz. We will compare both approaches for a case of a fixed-fixed beam of rectangular cross-section and length *l* with point force applied to it as shown in Fig. 5-7 [14] (only the direction of the Y-axis is different in the first approach)

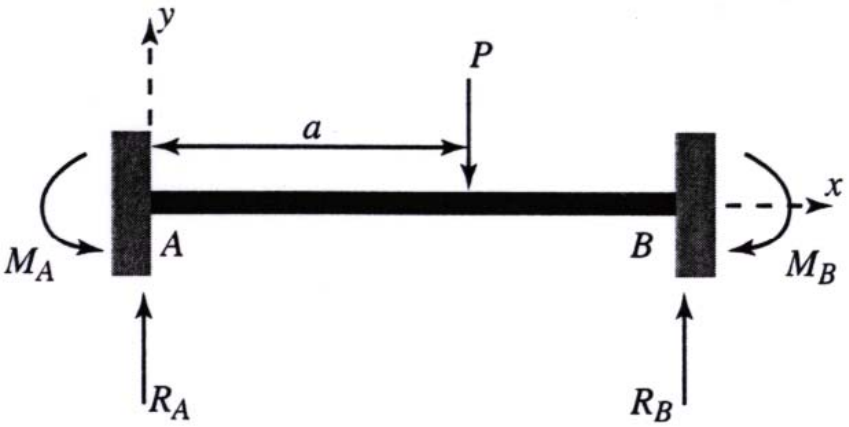

Fig. 5-7. Fixed-fixed beam with concentrated vertical load *P* [14]

M_x and R_x are the reaction moments and the vertical reactions at the beam ends, respectively.

The first method starts with the beam equation from [34] for a point force

$$E\,I\,y''''(x) - T\,y''(x) = P\delta(x-a)\,, \quad (5.13)$$

where *y(x)* is the beam vertical deflection as a function of point position along the beam length, *E* – Young's modulus of the beam material, *P* – point force applied to beam at point *a*, δ - delta-function. *I* is the moment of inertia; for a rectangular cross-section we have $I = wt^3/12$, where *w* and *t* are the beam width and thickness, respectively. The force produced by the residual tensile stress is $T = wt(1-\nu)\sigma$, where ν is the Poisson's ratio, and σ - the residual tensile stress. The boundary conditions are as follows

$$0 = y(A) = y'(A) = y(B) = y'(B)\,, \quad (5.14)$$

The solution for $a = l/2$ (i.e. when the force is applied to the centre of the beam, which is often the case) is

$$y(x) = \frac{P}{2\sqrt{\frac{T}{E\,I_z}}\,T}\left\{\sqrt{\frac{T}{E\,I_z}}\,x - \sinh\left(\sqrt{\frac{T}{E\,I_z}}\,x\right) + \left(\cosh\left(\sqrt{\frac{T}{E\,I_z}}\,x\right) - 1\right)\tanh\frac{\sqrt{\frac{T}{E\,I_z}}\,l}{4}\right\} \quad (5.15)$$

If a deflection of the centre of the beam is considered (which is usually the case), then

$$y(l/2) = \frac{P}{T}\left\{\frac{l}{4} - \frac{\tanh\left(\frac{l}{4}\sqrt{\frac{T}{E\,I_z}}\right)}{\sqrt{\frac{T}{E\,I_z}}}\right\} \quad (5.16)$$

The spring constant is found from Hooke's law and a Taylor series expansion (assumed *T* is small):

$$k = \frac{P}{y(l/2)} = \frac{T}{\left\{\frac{l}{4} - \frac{\tanh\left(\frac{l}{4}\sqrt{\frac{T}{EI_z}}\right)}{\sqrt{\frac{T}{EI_z}}}\right\}} \approx \frac{16\, w\, t^3\, E}{l^3} + \frac{24\, wt(1-\nu)\sigma}{5\, l} \quad (5.17)$$

One can see that there are two components of the spring constant: one depending on the Young's modulus of the beam material, and the other one depending on the residual tensile stress in the beam.

Rebeiz in [14] looked for the two spring constant components separately. To find the first one (depending on the Young modulus) he used the same model as mentioned above. His starting with equation and solution (with reference to [Roark-Young]) were:

$$\begin{aligned} EI\frac{d^2y}{dx^2} &= M_A + R_A x \\ M_A &= -\frac{Pa}{l^2}(l-a)^2 \\ R_A &= \frac{P}{l^3}(l-a)^2(l+2a) \\ y(x) &= \frac{M_A x^2}{2EI} + \frac{R_A x^3}{6EI} \end{aligned} \qquad \text{for } x \le a \qquad (5.18)$$

If the deflection in the centre is of interest, then

$$y(l/2) = \frac{P}{4Ewt^3}\left(l^3 - 6al^2 + 9a^2 l - 4a^3\right) \quad (5.19)$$

For point force applied to the centre of the beam ($a = l/2$)

$$y(l/2) = -\frac{Pl^3}{16Ewt^3} \quad (5.20)$$

Then the spring constant is

$$k_1 = -\frac{P}{y(l/2)} = \frac{16Ewt^3}{l^3}, \quad (5.21)$$

which is identical to what we obtained with the first approach.

To find the second spring constant component, which depends on the residual tensile stress, Rebeiz suggests modelling the membrane as a stretched wire (Fig. 5-8 [14])

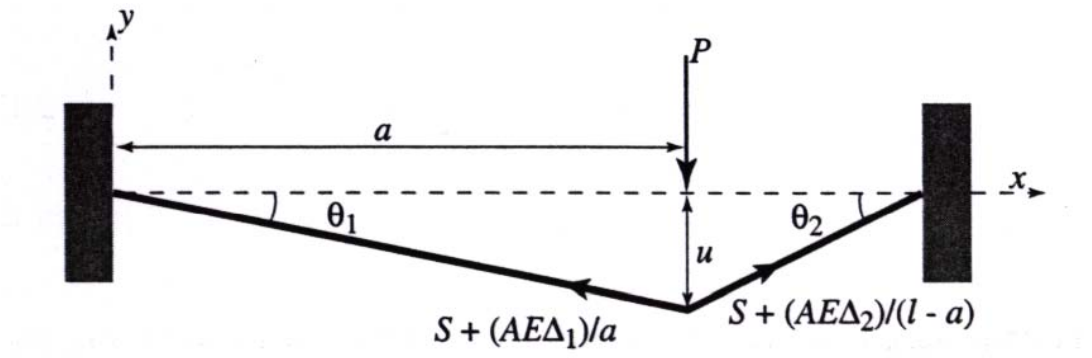

Fig. 5-8. Beam modelled as a stretched wire with concentrated vertical load *P* [14].

Here the stress-induced force is denoted as $S = wt(1-\nu)\sigma$, A is the cross-section area of the beam. Under a vertical point force the beam deflects by u at the location of the applied force. The beam stretching (or elongation) due to deflection is the difference in length between the stretched and the initial length and consists of two parts (to the left and to the right of the force location)

$$\begin{aligned} \Delta_l &= \sqrt{a^2 + u^2} - a \\ \Delta_r &= \sqrt{(l-a)^2 + u^2} - (l-a) \end{aligned} \qquad (5.22)$$

The stretching results in the following stress-induced force increase

$$\begin{aligned} S + \frac{AE\Delta_l}{a} \\ S + \frac{AE\Delta_r}{(l-a)} \end{aligned} \qquad (5.23)$$

By equating the applied force to the forces in the beam projected onto the vertical direction and assuming a small u (see Appendix 1) one can obtain the following equation

$$u = \frac{Pa(l-a)}{Sl}, \qquad (5.24)$$

where the additional force due to stretching is neglected. From this equation the deflection at the centre of the beam (see Appendix) is found to be

$$y = -\frac{P}{2S}(l-a) \qquad (5.25)$$

If the force is also applied to the centre of the beam, then

$$y = -\frac{Pl}{4S} \qquad (5.26)$$

and the spring constant is

$$k_2 = -\frac{P}{y} = \frac{4S}{l} = \frac{4wt(1-\nu)\sigma}{l} \qquad (5.27)$$

One can see that the numerical coefficient (4) differs from the one obtained in the first approach (24/5 = 4.8). It is hard to say which approximation is better, unless one knows the stress value precisely enough. For further calculations the second approach was chosen.

5.2.3 Case studies

In reality one applies distributed forces, not point forces. Mathematically, the transition from a point force to a distributed force is realised through integration of Eq. 5-19 by *a* over the membrane length, where the distributed force is applied. Let us consider the case, when a distributed force is applied to the central part of the beam, as shown in Fig. 5-9.

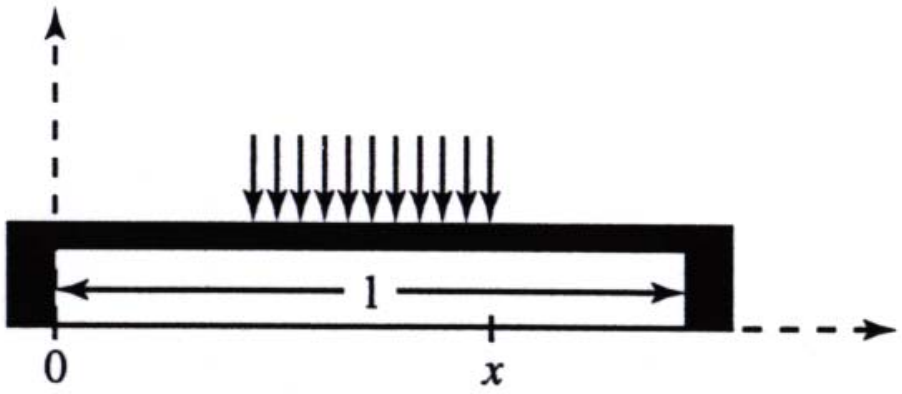

Fig. 5-9. Fixed-fixed beam with force evenly distributed about the centre of the beam [14]

In this case integration from *l/2* to *x* should be performed and the integral should be doubled due to symmetry considerations. The result is

$$k_1 = 32Ew\left(\frac{t}{l}\right)^3 \frac{1}{8(x/l)^3 - 20(x/l)^2 + 14(x/l) - 1}$$
$$k_2 = 8\sigma(1-\nu)w\left(\frac{t}{l}\right)\frac{1}{3-2(x/l)} \qquad (5.28\text{-}5.29)$$

When the force is distributed across the edges of the beam, as shown in Fig. 5-10.

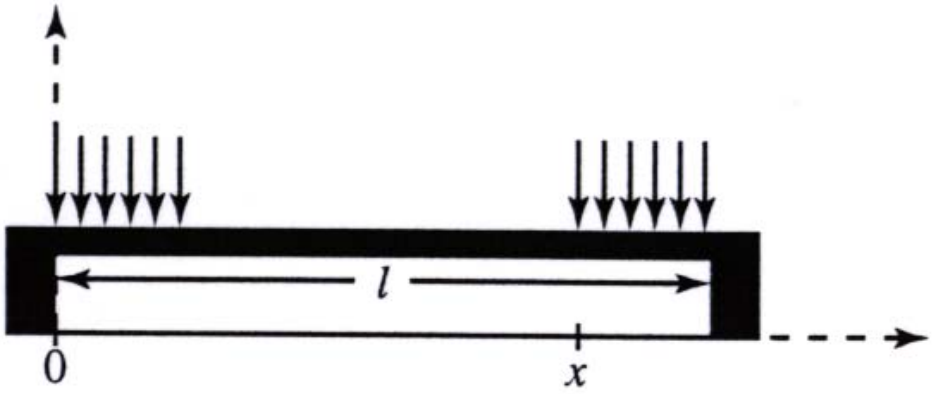

Fig. 5-10. Fixed-fixed beam with force evenly distributed about the edges of the beam [14]

then integration from x to l should be performed and the spring constant components take the form

$$k_1 = 4Ew\left(\frac{t}{l}\right)^3 \frac{1}{x/l\left(x/l-1\right)^2} \qquad (5.30\text{-}5.31)$$
$$k_2 = 8\sigma(1-\nu)w\left(\frac{t}{l}\right)\frac{1}{1-x/l}$$

Now the deflection curve can be plotted, provided Young's modulus and the stress magnitude are known. The latter is not always easy to find out precisely enough. The deflection curve allows to plot the CV-curve using a simple parallel-plate capacity formula, since the centre of the membrane, which forms the capacity, hardly changes its initial shape.

5.2.4 Effect of Holes in the Beam

Perforation holes used in MEMS switches and varactors have some effect on their internal stress and the effective Young's modulus. The perforation pattern (Fig. 5-11)

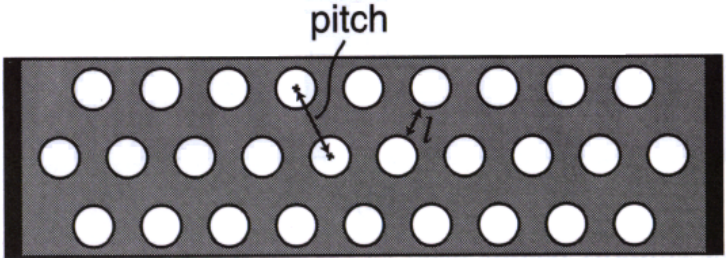

Fig. 5-11. Parameters for the ligament efficiency in a beam with holes [14]

is characterised by the ligament efficiency [14]

$$\mu = \frac{l}{pitch} \qquad (5.32)$$

The reduced residual stress is approximately

$$\sigma = (1-\mu)\sigma_0 , \qquad (5.33)$$

where σ_0 is the stress without perforation. The effective Young's modulus is reduced by 25% for μ = 0.625 [14]. As our basic configuration has μ = 0.642, the same reduction coefficient was used in the calculations. The effect of the holes on capacity is negligible if the diameter of the holes is less than 3-4g_0. The reason is due to the fringing fields that "fill" the area of the holes [14]. In our case the diameter was equal to 4g_0 and no significant deviation from the expected capacities was observed.

Notes on finite element modelling can be found in Appendix 3.

5.3 Optical Measurements

The optical measurements result in height-voltage curves, which can be simulated with the help of the analytical model. As was pointed out in section 5.2, the intrinsic stress is an unknown parameter. Thus comparison of model curves with experimental results can give us the stress. The three possible ways of actuation – through central electrode, through lower side electrodes, and through upper side electrodes – define three modes for the optical measurements, where only one of the electrode types is acting. All three types of experiments were performed. However, their analytical description is different. Whereas the analytical model can be a good approximation for the case of the central electrode, certain difficulties are met with side electrodes. The reason is that the model assumes the membrane to always stay parallel to the attracting electrodes. This is more or less valid for the case of the central electrode (since the membrane curvature is very small), but rather not valid for the case of the side electrodes, as was already pointed out in section 5.2. The details of the measurement procedure can be found in section 4.1.

Actually, the intrinsic stress is found from the results in the central mode. Experimental points and the fitting curve are shown in Fig. 5-12. Initial height of 3.5 μm results from the sum of the gap (designed 2.5 μm) and the membrane thickness (designed 1 μm), as the interferometer "sees" the membrane from above. The maximum deflection amounted to 0.77 μm, which is close to $g_0/3$ = 0.83. The reason, that the measured maximum deflection is normally smaller than the theoretical one, is that one measures at best the last but one step (and with the next step collapse takes place), and it is sometimes hard to decide what voltage step has to be chosen (it has to be smaller than the previous one, since most of the deflection happens close to collapse). Often several small voltage steps are made without a lengthy measurement to see a more or less significant height change – and the collapse comes before the measurement. The stress is found from both the pull-down voltage value and the visual points fitting (because it is often possible to notice the pull-down voltage, but no height measurement is possible any more – the membrane has already collapsed).

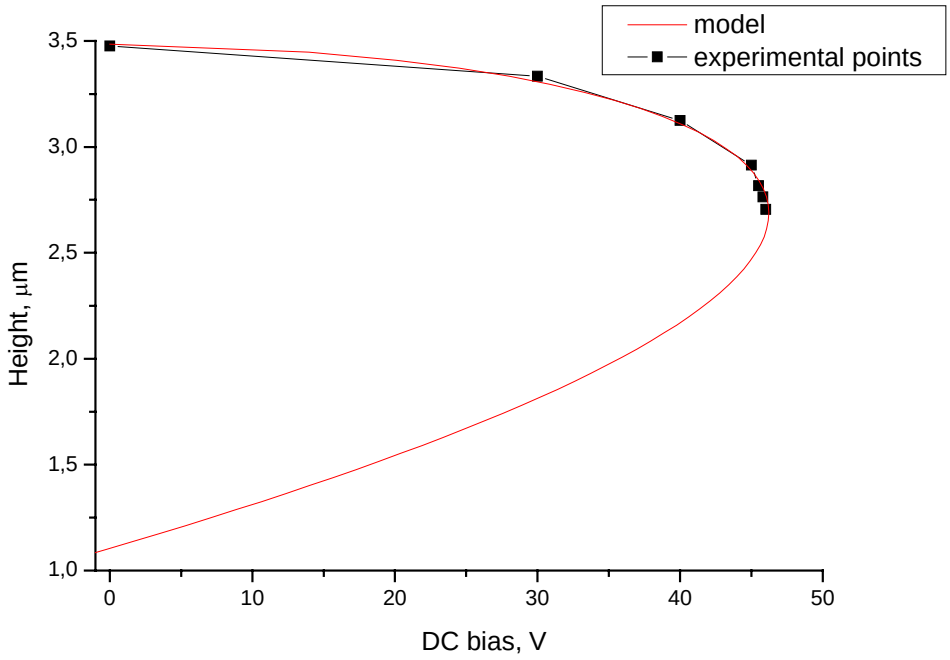

Fig. 5-12. Height-voltage curve when the central electrode is biased.

The measured pull-down voltage was 46.2 V DC, the fitted stress value for this analytical curve was 79.25 MPa. It is illustrative to compare magnitudes of spring constant components at this stress level. The first one, defined by material properties, is 1.4 N/m, whereas the second one, defined by the stress, is 46.3 N/m. Obviously, intrinsic stress completely dominates the mechanical behaviour of the structure under investigation. It is also interesting to see the influence of the dielectric layer. If one tries to fit the points without taking the dielectric into consideration, one arrives at ca. 65 MPa. FEM modelling delivered similar results (see Appendix 3)

In the next example, the membrane was actuated through lower side electrodes (Fig. 5-13). Again, the height starts at 3.5 μm as explained above. The measured deflection was only 0.64 μm – for the reason described above, but the measured pull-down voltage allowed to build the analytical curve.

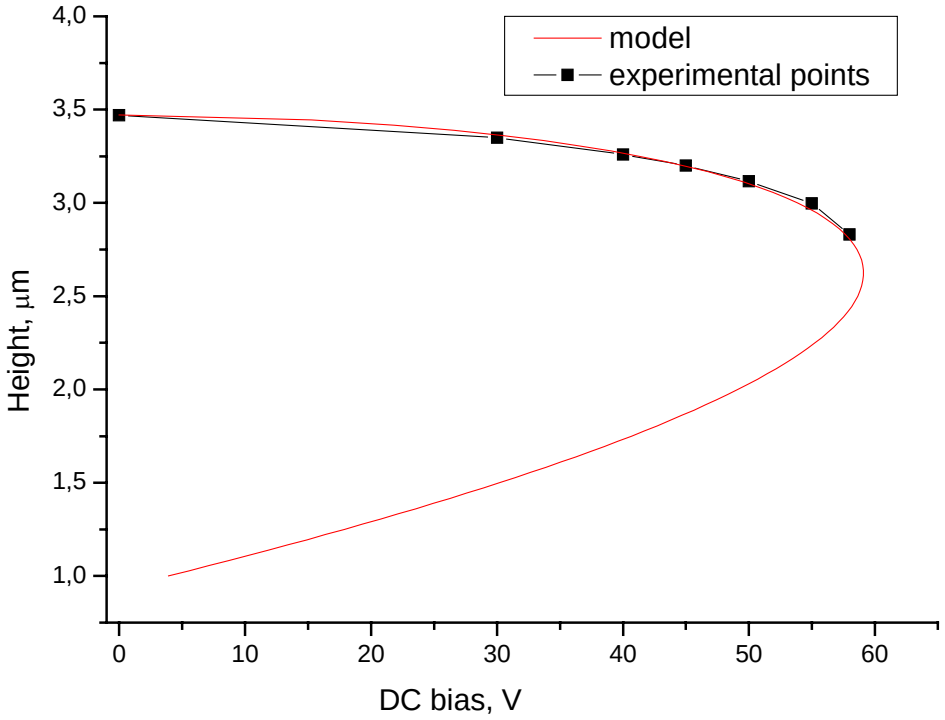

Fig. 5-13. Height-voltage curve when the lower electrodes are biased.

For the model, electrode length of $l/4$ = 125 μm was taken for sake of derivation simplicity (real length was 132 μm). Pull-down voltage of 59 V DC gives 130 MPa stress according to the model. From comparison with stress value found above we see that the model is a rather poor approximation in this case and requires some correction. One of the ways to introduce a correction is to assume that effectively only part of the electrode attracts the membrane, whereas the rest of the electrode (situated closer to the fixed end of the membrane) is neglected, i.e. to "shorten" the electrode. To result in stress value of 79.25 MPa one has to assume that only 62% of the electrode area (or length) works effectively for this configuration.

In the last mode upper side electrodes are used (Fig. 5-14). The situation is similar to the previous case, the difference is absence of dielectric. The initial height is in this case different from 3.5 μm. This is due to variations in gap and membrane thickness magnitudes over the wafer (values can be found in section 5.1). The gap to the upper electrode was 2.09 μm. The measured deflection amounted 0.57 μm, which is again smaller than the expected 1/3 of the initial gap.

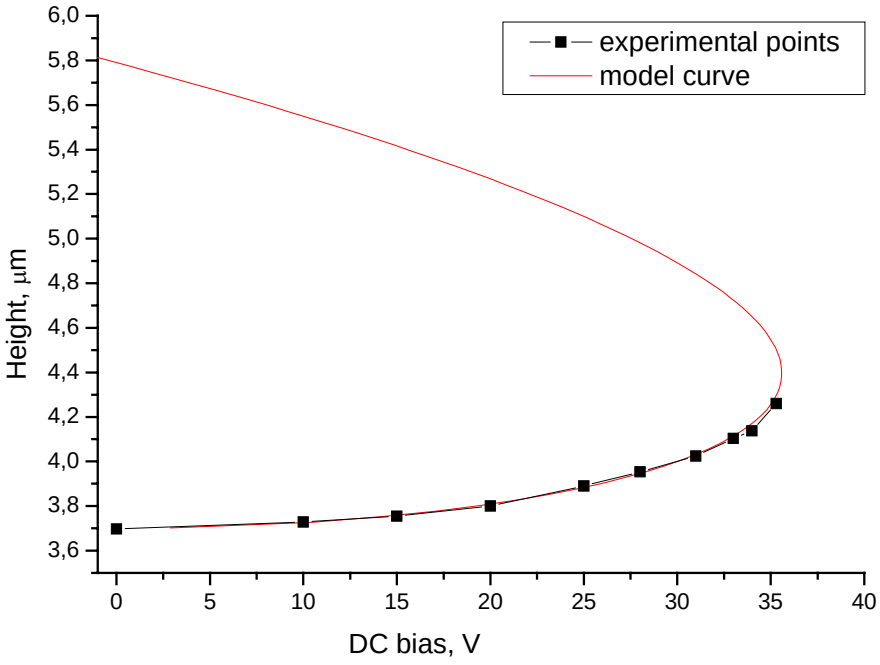

Fig. 5-14. Height-voltage curve when the upper electrodes are biased.

The electrode length was set in the model to $l/3$ = 167 μm (the real length was 150 μm and the gap to the suspension was 25 μm), and the electrode was assumed to start exactly above the membrane's fixed end, for similar reason as above. But at the same time the real area of the electrode was used in the calculation, where the perforation holes area was subtracted. Pull-down voltage of 35.6 V DC leads to stress value of 91 MPa. Area correction sets effective electrode length at 88%. The higher electrode effective length (as compared to the previous case) is believed to be due to larger length.

One can notice that the experimental points follow the analytical curves without any significant leveraged bending influence. This is due to the high tensile stress in the membrane, as will be shown in section 5.5.

5.4 Low-Frequency Measurements

Low-frequency measurements result in a CV-curve – one of the important characteristics of a varactor. It was already possible to perform low-frequency measurements together with the optical measurements (Fig. 5-15).

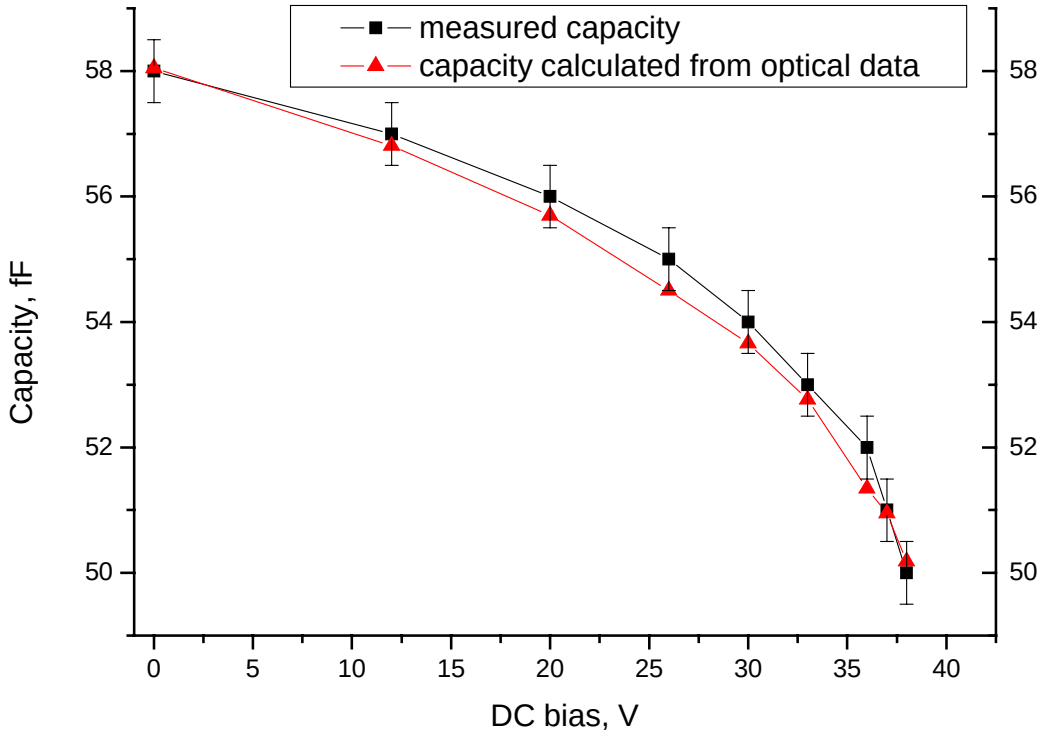

Fig. 5-15. CV-curve taken together with an optical measurement and a calculated curve based on optical data (parasitic capacity is not subtracted). Upper side electrodes are biased. Good coincidence shows that the capacity change is due to the membrane deflection, and not due to other reasons.

However, the setup described in section 4.2 provided higher resolution and faster measurements due to software, which automated voltage variation and capacity measurement (in optical measurements the voltage had to be changed manually). The details of the measurement procedure are described in section 4.2. Since only complete CV-curves (with maximum possible capacity change) were of interest, no CV-curves where the central electrode is biased were taken. As we saw in section 5.3, the pull-down voltage is higher than 40 V DC, which is the upper limit for the HP LCR-meter used in the experiments. The side electrodes were supplied with help of a separate voltage source with upper limit of 110 V DC, but the LCR-meter would not function correctly if needles connected to the separate voltage source were put on the signal line, where the capacity was measured. This mode is also not so important as for the optical measurements, since the designed actuation modes are through lower and upper side electrodes. Thus, only curves for these two modes will be presented here.

A typical CV-curve for the mode, where lower side electrodes were biased, is shown in Fig. 5-16. The starting capacity lies at 55.7 fF, whereas a capacity of about 36 fF is expected from the parallel-plate capacitor formula. The reason is the parasitic capacity of about 20 fF, which comes mainly from the substrate. As was described in section 4.2, the parasitic capacity is not necessarily constant and might vary with frequency or applied bias. But at the chosen signal frequency of 10 kHz this variation was negligible. The bias to lower electrodes was changed in steps by 0.1 V. It is obvious that measurement with such resolution would take more than 24 hours if optical setup were used.

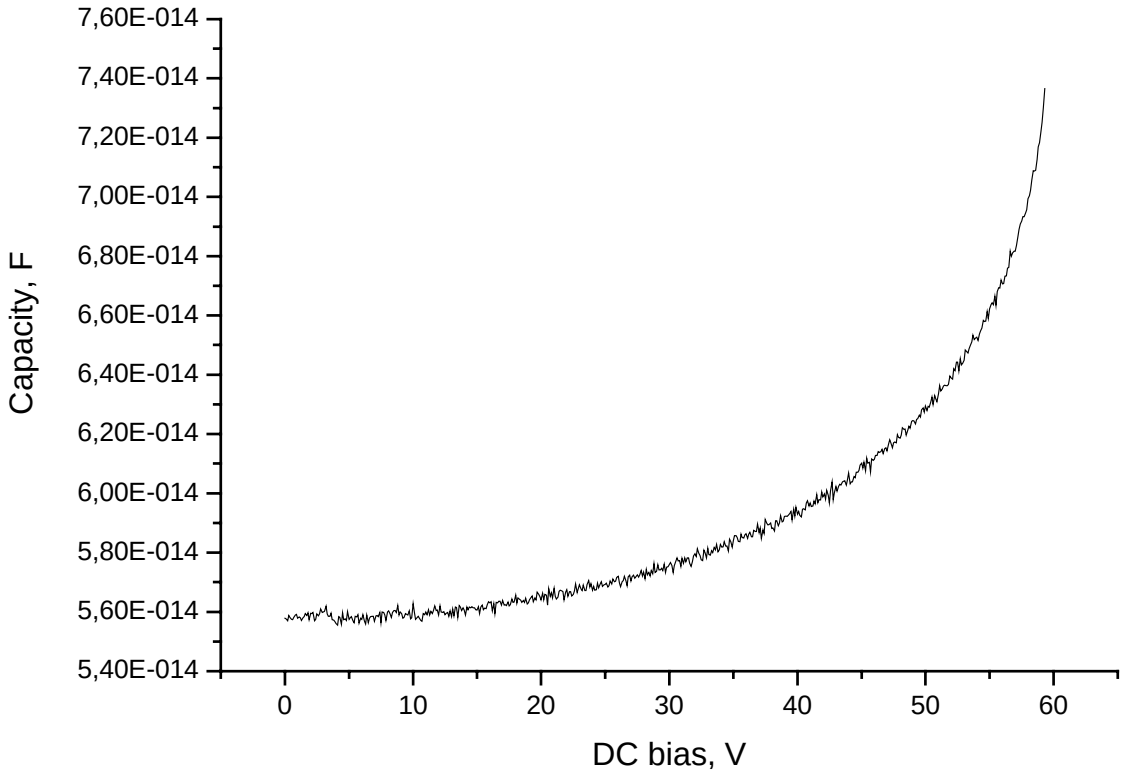

Fig. 5-16. A typical CV-curve of a parallel-plate varactors actuated through lower side electrodes.

The capacity change amounted to 18 fF at a pull-down voltage of 59.3 V DC.

Fig. 5-17 presents a typical CV-curve taken in the mode, where the upper side electrodes were biased. The initial capacity lies at 55.1 fF. The capacity change is 7.6 fF. Pull-up voltage was measured to be 37.8 V DC.

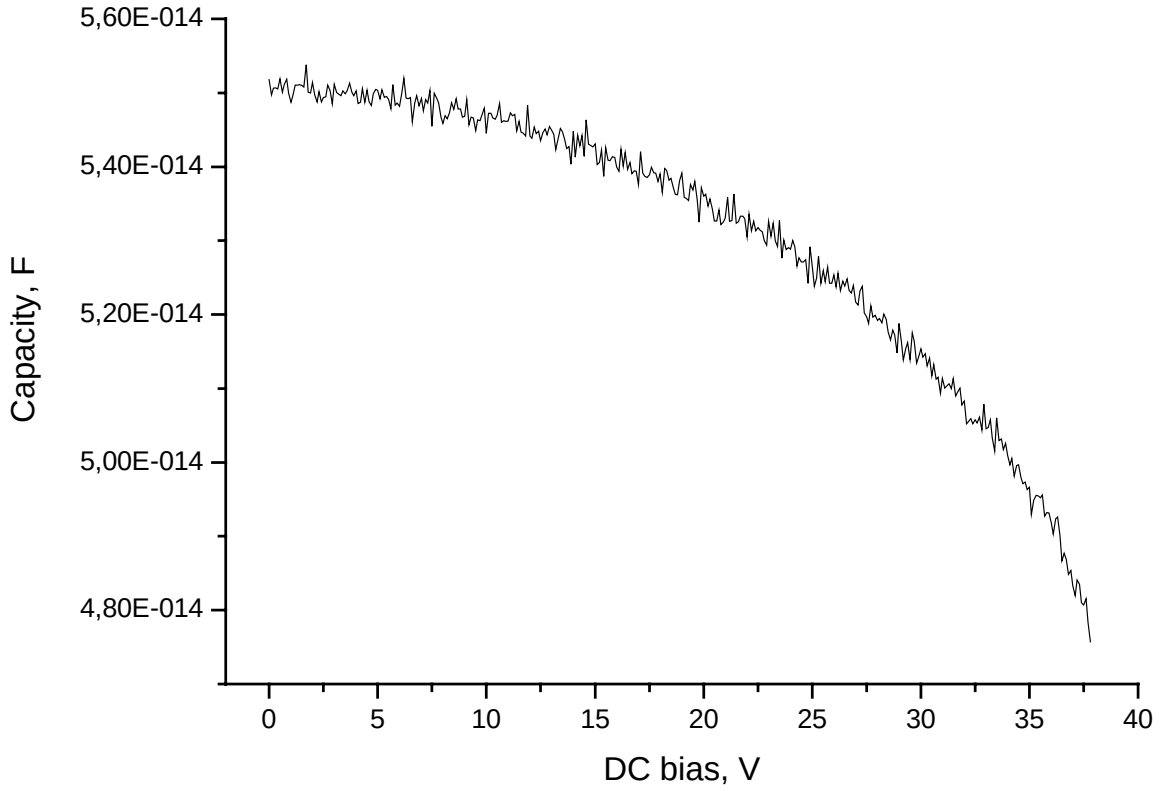

Fig. 5-17. A typical CV-curve of a parallel-plate varactor actuated through upper side electrodes.

Finally, both capacity changes result in the overall capacity change achievable with the varactor – 25.6 fF. The capacity change corresponds to a capacity ratio of 1.55 including parasitics, and 1.95 without parasitics. Even with parasitics, the theoretical capacity ratio of 1.5 is surpassed with this varactor.

Due to layer thickness variation mentioned in section 5.1, a variation of capacity values over the wafer was observed. The data are summarised in Table 5-2.

	Measured range	**Average**
Capacity ratio	1.51÷1.56	1.54 with parasitics
Maximum tuning voltage	59.3÷63.6 V	61.5 V
Capacity change	22.7÷27.1	25 fF
Parasitic capacity	18÷20 fF	19 fF

Table 5-2. Important varactor characteristics.

5.5 Main Problems

In this section main technological and functional problems met with parallel-plate varactor will be discussed. They are release stiction, high tensile stress, and dielectric charging.

5.5.1 Release Stiction

Release stiction is a well-known failure reasons in MEMS technology. Release stiction (the term is a short form of static friction) is a demonstration of capillary and adhesion forces during the drying phase of release wet etching. For the stiction to take place, the membrane first has to be pulled down (in a collapse manner) by the capillary forces of the remaining liquid. In the second step adhesion forces need to hold the membrane fixed at the adhering surface (Fig. 5-18 [36-37]). The schematic drawings show a side-view of an elastic beam (of thickness t and length l) fixed at two ends and suspended over a rigid substrate at height h. There is some liquid of initial volume V_l between the beam and the substrate during the first stiction step.

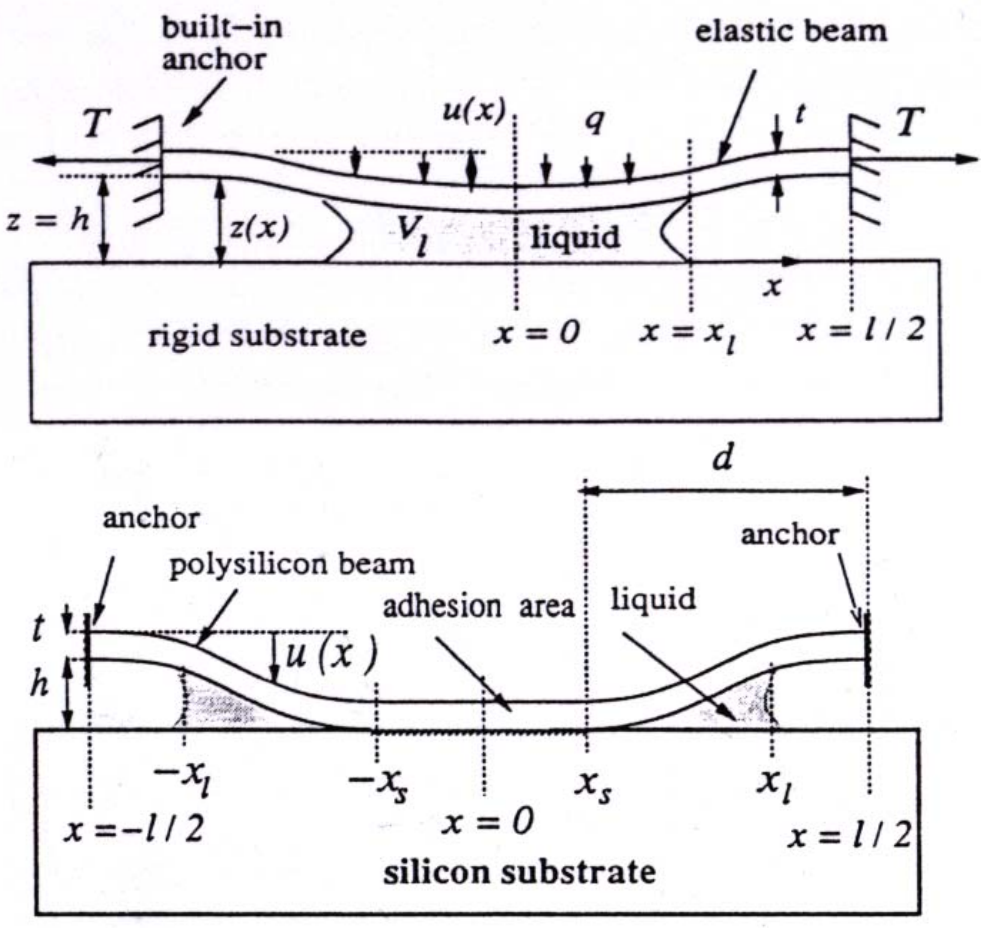

Fig. 5-18. Two steps of release stiction [36-37].

To describe release stiction mathematically, one can use the elastocapillary number N_{EC} [36] and the peel number N_P [37]. The elastocapillary number is defined so that if $N_{EC} > 1$, the beam is free, and if $N_{EC} < 1$, the beam is pinned. The elastocapillary number can be expressed as follows

$$N_{EC} = \frac{128EIh^2t^3}{15\gamma_l \cos\theta_c l^4\left(1+\frac{t}{w}\right)}\left(1+\frac{2\sigma l^2}{7Et^2}+\frac{108h^2}{245t^2}\right), \quad (5.34)$$

where E is the Young's modulus of the beam material, I – beam's moment of inertia, γ – surface energy per unit area at liquid-air interface, θ_c – the contact angle, w – the beam width, σ - internal stress in the beam. Unfortunately, the surface energy per unit area and the contact angle are not always known and have to be defined experimentally in order to make any predictions.

The peel number is defined so that the beam peels completely for $N_P > 1$ and is pinned for $N_P < 1$. The peel number can be expressed as follows

$$N_p = \left(\frac{128Eh^2t^3}{5\gamma_S l^4}\right)\left[1+\frac{4\sigma l^2}{21Et^2}+\frac{256}{2205}\left(\frac{h}{t}\right)^2\right], \qquad (5.35)$$

where γ_S is the interfacial adhesion energy per unit contact area. Again, this parameter is not always readily available. Theoretically, for release stiction to take place, both numbers need to be less than unity.

In our investigation, release stiction did not allow us to test cantilever structures and some bridge-based structures (see section 5.6.1) – all of them were pinned after the release etch. There are technological and design solutions to combat release stiction.

The radical solution for this problem is to change from wet etching to dry etching. It has to be kept in mind however, that a low-temperature dry etch process is desired, since any high-temperature processes induce material changes, e.g. internal stress change. Such a low-temperature process was unfortunately not available for our investigation.

Other solutions include critical point drying and freeze-dry release [14]. These technological methods to avoid release stiction demand special equipment, which is not always available and increases the final product cost. Below a design method will be discussed.

Intuitively (and as can also be seen from the formulas), stiction probability is reduced if the initial gap h or the spring constant of the beam (proportional to t and σ, and inversely proportional to l) are increased. It is obvious however (and can be checked with formulas from section 5.2.1) that the same design changes would lead to increased pull-down voltage (and consequently, the operating voltage – which is undesirable). This trade-off can be avoided with help of our suspension structures: tensile stress can be decreased during post-processing. The details are shown below.

5.5.2 High Tensile Stress

As we saw in section 5.3, no significant influence of the leveraged bending effect on membranes behaviour was observed. The reason for that is the high tensile stress in the tested membranes (Fig. 5-19 [32]).

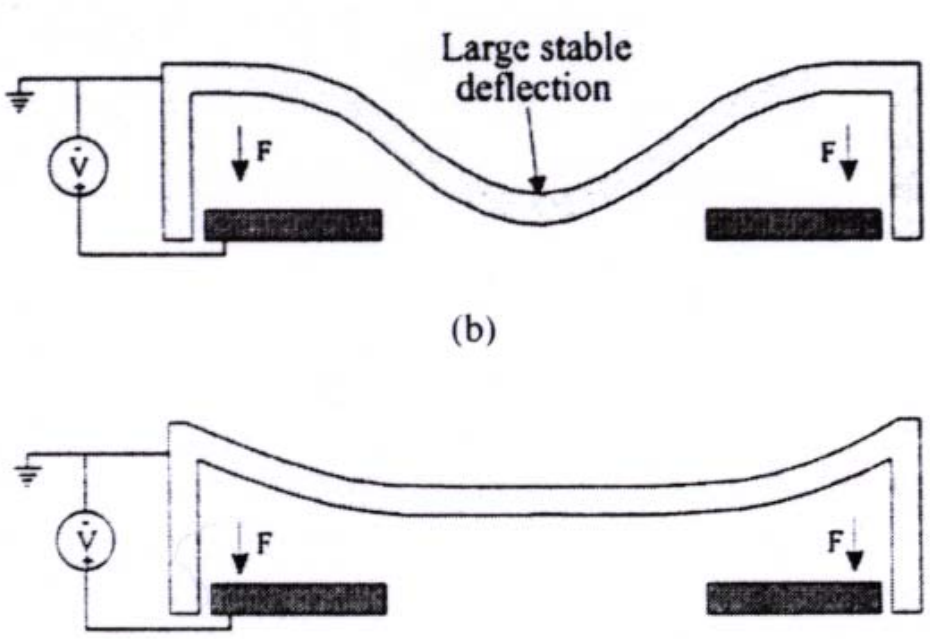

Fig. 5-19. Leveraged bending effect (top) attenuated by high tensile stress (bottom) [32]

In [32] a limit on tensile stress for the leveraged bending effect to take place is set according to the following formula

$$\sigma < \frac{Et^2}{2(1-\nu)l_{el}(l\ -l_{el})}, \qquad (5.36)$$

where ν is the Poisson's number, and l_{el} – side electrode length. For our basic configuration, stress smaller than 2.5 MPa is allowed by this model. The calculated actual stress of 79 MPa is much higher. Stress can be modified technologically, i.e. some process parameters have to be changed to achieve lower stress state. An interesting alternative is suggested by the special suspension structures used in this work. It was found that they do not completely compensate the rising compressive stress when the varactors are annealed. In a series of experiments, where profiles of membranes after annealing (2 hours) were investigated, a buckling effect at high temperatures was observed. The stress was calculated according to the Euler buckling model [30] (see Appendix 2 for details):

$$\sigma_0 = -\frac{E\pi^2}{L^2}\left(\frac{w_0^2}{4}+\frac{t^2}{3}\right), \qquad (5.37)$$

where σ_0 is the internal compressive stress causing buckling (after buckling occurs, the stress is equal to the critical value, see below), Young's modulus is taken as $E_{Ni}/(1-\nu^2)$ (this transform is used when changing from a beam to a membrane), and w_0 – buckling amplitude (amplitude of the membrane deflection). For buckling to take place at all, internal compressive stress must be larger by magnitude than the critical stress

$$\sigma_{crit} = -E\frac{\pi^2 t^2}{3L^2}, \qquad (5.38)$$

and this stress is present in all equilibrium buckling states. For our basic configuration, $\sigma_{crit} \approx$ -10 MPa. Fig. 5-20 shows the result of the measurements – calculated compressive stress in the membrane as a function of annealing temperature, critical stress level is shown as a dotted line.

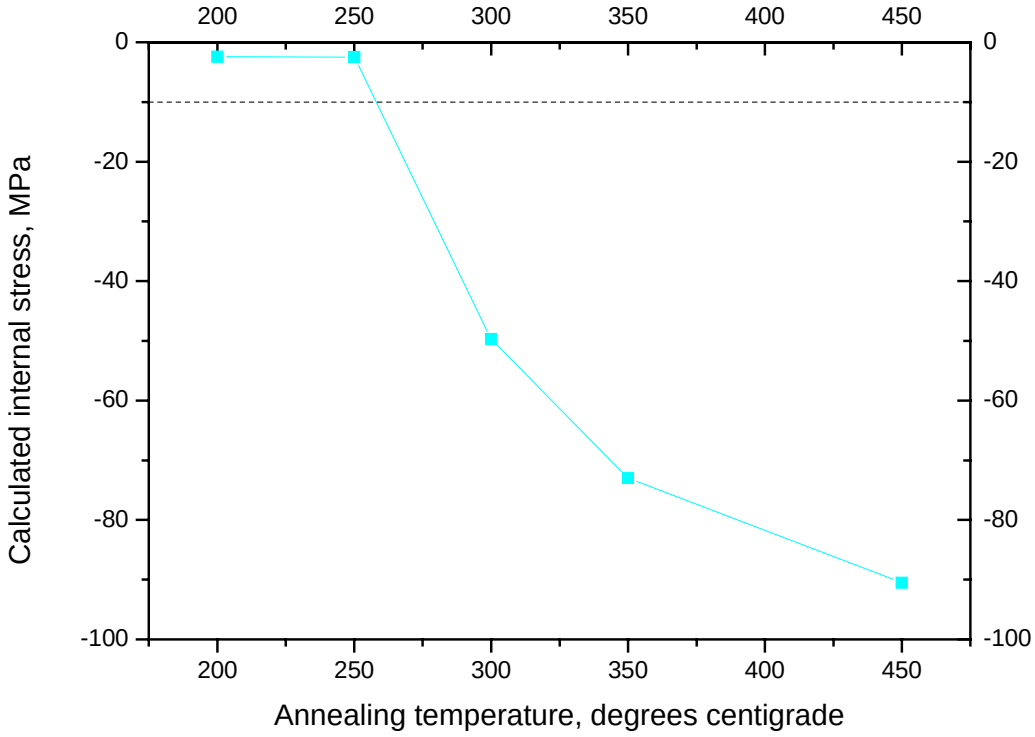

Fig. 5-20. Internal (compressive) stress vs. annealing temperature.

One can see that below the annealing temperature of 250°C the stress is above the critical level (no buckling was observed optically). The critical level is reached between 250°C and 300°C, and at 450°C a stress of -90 MPa was calculated according to the optically measured buckling amplitude. Keeping in mind that initially (without annealing) an internal stress of about 79 MPa was calculated, the suspension structure allows stress variation of 170 MPa between 20°C (room temperature) and 450°C. Obviously, annealing temperature below 300°C can be found to result in low tensile or slightly compressive stress (< 2.5 MPa) to allow leveraged bending to take place. However, the annealing procedure must be tuned well enough to keep stress level above -10 MPa, to avoid buckling.

5.5.3 Dielectric Charging

A dielectric layer was deposited on lower electrodes in the hope that it will prevent the device failure in case of accidental pull-down due to short-circuit. Testing has shown that even though the short-circuit is prevented, charging of the dielectric layer upon contact with the membrane results in a shift of the actuation voltage as large as 20 V. Charging consists of trapping of charge carriers on the surface, the interface and the bulk traps in the dielectric. It

strongly depends on the defect density of the used dielectric and therefore on the deposition process.

Charge trapping mechanisms in dielectric layers have been investigated for 20 years because they are essential to the proper operation of MOS transistors. There are three trapping areas in a MEMS capacitive device (switch or a varactor): The interface between the metal and the dielectric layer, the bulk traps inside the dielectric layer, and the surface-state traps on top of the dielectric layer (Fig. 5-21 [14]).

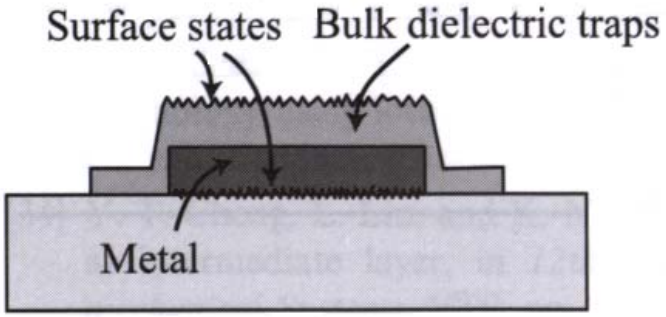

Fig. 5-21. Trapping areas in a capacitive MEMS device [14]

Several well-known properties of dielectric charging are as follows:

1) The charging of dielectrics is due to the application of stress, whatever its nature: mechanical, ionising, thermal, or electric field stress.
2) Electrons are trapped at low fields (2-5 MV/cm) and de-trapped at high fields, while trapped positive charges are typically observed at high fields (7-10 MV/cm).
3) Surfaces and interfaces, which are areas where defects are concentrated, will be areas where charges are preferentially trapped.
4) There is no direct relationship between an insulator conductivity and its charging properties. The trapped electrostatic charge is not only due to the insulating nature of the material (ionic or covalent), but is due to defects, either from its crystallographic structure or from defects due to tooling (dislocation, nonstoichiometry), or due to radiation under ionising beams (electron, photon, or ion bombardment of SiO_2).
5) Dielectrics will break down at any high electric field, provided that they are stressed long enough. The breakdown will always occur beyond a certain amount of injected charge [14].

For an actuation voltage of 30-60 V and a dielectric thickness of 1500 Å, the electric field can be as high as 2-4 MV/cm in the dielectric layer. Under these high field conditions, it is possible for charges to tunnel into the dielectric either by Frenkel-Poole emission or by a whole set of other mechanisms. Once a charge is injected into the surface states and dielectric layer and is subjected to a large electric field, it can be transported inside the dielectric using a conduction model. The recombination time for these charges is very long, of the order of seconds to days [14].

The measured shift in actuation voltage is not really an important drawback, since the varactors are actually designed to operate at voltages smaller than the pull-down voltage. But if pull-down is not completely excluded, dielectrics less prone to charging should be looked for, or the dielectric surface should be made smaller – for instance, structured into islands. Another solution is to decrease the actuation voltage (and simultaneously the electric field

between the plates). However, this can be problematic if wet etching is used (due to release stiction), and if high-power RF signals are expected (and so called self-actuation might take place). One can also change from DC bias to AC bias. However, AC bias applied to side electrodes might affect the capacitive behaviour of the substrate.

Unfortunately, dielectric charging does not only take place upon contact with the membrane. Considerable charging begins when the dielectric is subjected to strong electric field between the plates without contact. Demonstrations of contactless dielectric charging are illustrated below. The measurements were performed with the optical setup. The result of the first measurement is shown in Fig. 5-22. Shown is the height of the membrane above the sensing electrode measured several times in a row with steps of approx. 5 min. A voltage of 50 V was constantly applied to the lower side electrodes covered with dielectric. We can see that the height grows. The reason for that is most probably the growing charge in the dielectric, which leads to a decrease of the force applied to the membrane.

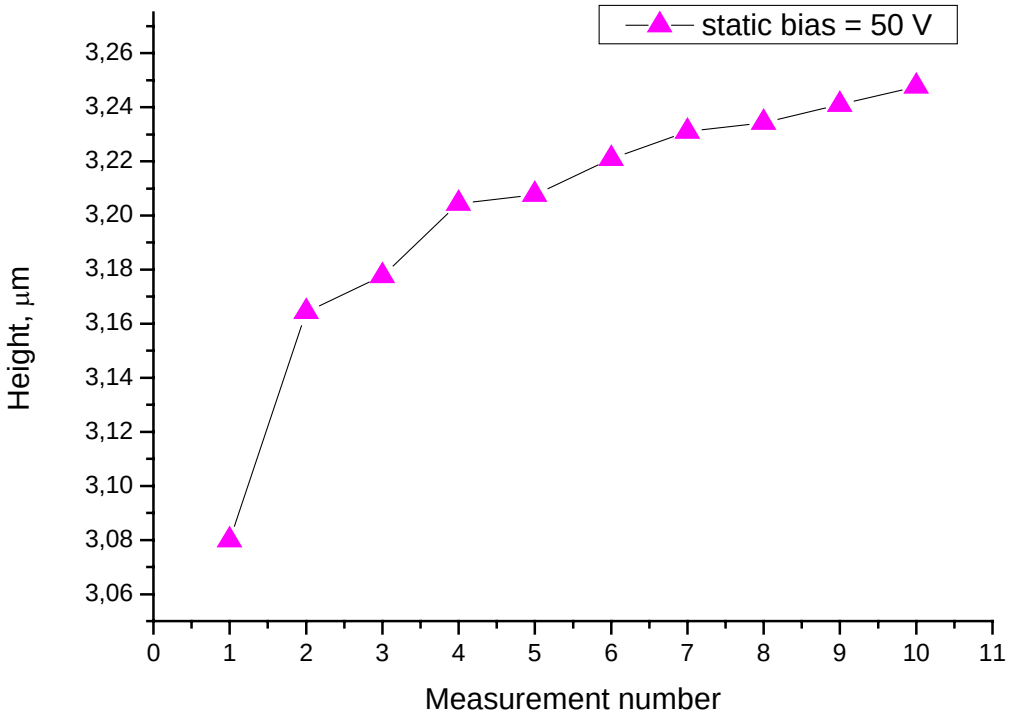

Fig. 5-22. Membrane centre height measured several times under 50 V DC applied to lower side electrodes (covered with dielectric). Height increases due to electrostatic force reduction, which is probably caused by charges trapped in dielectric.

Another example is obtained by biasing the lower side electrodes (covered with dielectric) with voltages of different polarity. As shown in Fig. 5-23, first the dielectric was subject to a positive bias, and then to a negative bias. Negative charges trapped in the dielectric and at its interface effectively increase the electrostatic force, when negative bias is applied. Thus one observes lower actuation voltage in the second experiment.

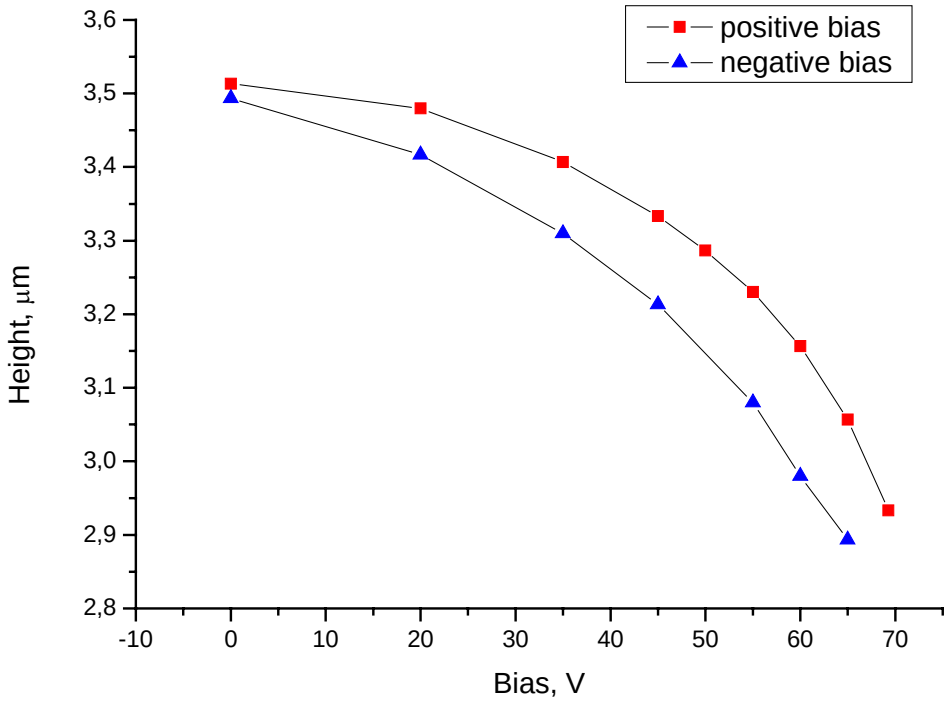

Fig. 5-23. Height-voltage curves with bias applied to lower side electrodes (covered with dielectric). Change of the polarity leads to lower actuation voltage.

We have to conclude that calculating the intrinsic stress from measurements where a dielectric is involved (as in section 5.3) is approximate rather than exact. Dielectric charging might make tensile stress appear larger by magnitude than it actually is. For exact calculations, devices without any dielectric layers should be taken.

An analytical description of the dielectric charging problem is given in [38-40]. The structure (Fig. 5-24) is modelled as shown in Fig. 5-25.

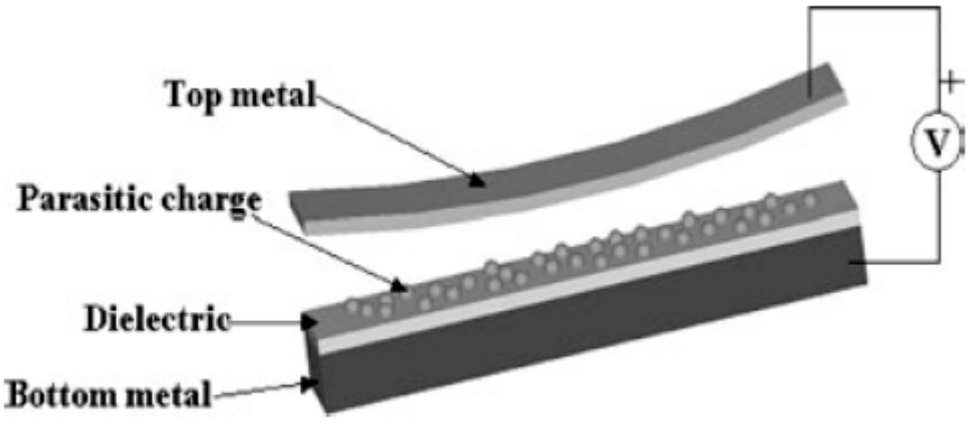

Fig. 5-24. Schematic of MEMS structure in consideration [40]

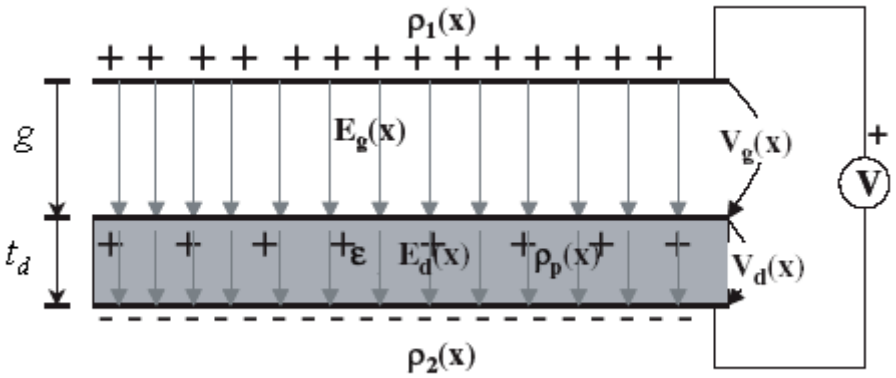

Fig. 5-25. Electrostatic model of the considered structure [40]. ρ_i is the charge density per unit area, E_i – electric field.

The applied voltage V divides into

$$V = V_g + V_d \quad (5.39)$$

The potential differences are as follows

$$V_g = E_g(g - z) \quad (5.40)$$

$$V_d = E_d t_d \quad (5.41)$$

The electric fields in the gap and in the dielectric are

$$E_g = -\frac{\rho_1}{\varepsilon_0} \quad (5.42)$$

$$E_d = \frac{\rho_2}{\varepsilon_0 \varepsilon} \quad (5.43)$$

and, taking the electrical neutrality $\rho_1 + \rho_2 + \rho_p = 0$ into account,

$$E_d = -\frac{\rho_1 + \rho_p}{\varepsilon_0 \varepsilon} \quad (5.44)$$

Finally, the applied voltage can be expressed as

$$V = V_g + V_d = -\frac{\rho_1}{\varepsilon_0}(g - z) - \frac{\rho_1 + \rho_p}{\varepsilon_0 \varepsilon} t_d = -\rho_1 \left[(g - z) + \frac{t_d}{\varepsilon_0 \varepsilon} \right] - \rho_p \frac{t_d}{\varepsilon_0 \varepsilon} = V_{reg} + V_p, \quad (5.45)$$

where V_p is the voltage shift (with respect to normally expected pull-down voltage) caused by the parasitic charge in the dielectric. If we apply it to the pull-down voltage, then

$$V_{pull-down}^{total} = V_{pull-down}^{reg} + V_p, \quad (5.46)$$

where $V_{pull-down}^{reg}$ is the pull-down voltage according to Eq. 5.12, and

$$\left|V_p\right| = \frac{\rho_p}{C_d}, \qquad (5.47)$$

where C_d is the dielectric capacitance per unit area.

Now we can assess the charge density in the dielectric based on the optical measurements from section 5.3 and low-frequency measurements from section 6.4.1. In section 5.3 a tensile stress of ca.79 MPa was calculated according to Eqs. 5.28-5.29 and 5-12. According to Eq. 6.1-6.2 and 5-12, a tensile stress of 44 MPa is calculated in section 6.4.1. If we assume the latter stress level, we can calculate the pull-down voltage for the case considered in section 5.3 according to Eq. 5-12. This calculation gives a pull-down voltage of 35.3 V. According to Eq. 5.46, V_p = 10.9 V. Assuming C_d equal to 34.9 nF/cm^2, $\rho_p = 0.38\times10^{-6}$ C/cm^2 = 2.4×10^{12} e/cm^2. This value lies in the range of 3.9×10^{11} to 3.2×10^{12} e/cm^2 reported in [38] ($0.4\div5\times10^{12}$ e/cm^2 are given in [14]).

To solve the charging problem one can look for dielectrics with negligible charging or simply get rid of them (since they play only an auxiliary role in parallel-plate varactors). Conditions for negligible charging are given in [41]. Equation for charge σ of interface charge layer i changing with time is as follows:

$$\sigma_i(t) = N_0 q \frac{\tau_{i,2}}{\tau_{i,1}+\tau_{i,2}}\left(1-\exp\left[-\frac{\tau_{i,1}+\tau_{i,2}}{\tau_{i,1}\tau_{i,2}}t\right]\right), \qquad (5.48)$$

where N_0 is the amount of available traps, q – the elementary charge, $\tau_{i,1}$ – time constant for charging, and $\tau_{i,2}$ – time constant for discharging. In equilibrium

$$\sigma_i(t\to\infty) = N_0 q \frac{\tau_{i,2}}{\tau_{i,1}+\tau_{i,2}}, \quad (5.49)$$

and so negligible charging is obtained if simultaneously

1) N_0 is small (a defect-free dielectric)
2) $\tau_{i,2}$ is so large compared to $\tau_{i,1}$ that no substantial amount of charge is permanently trapped
3) $\tau_{i,1}$ is so large that equilibrium is never reached and the amount of trapped charge stays low during the whole life of the device.

Some investigative efforts should be made exploring various dielectric materials suitable for RF MEMS devices. Usually dielectric charging is assessed through the actuation voltage shift created by the charges in dielectric [39-40]. In [40] a test device for MEMS reliability investigation and dielectric performance study was proposed (Fig. 5-26).

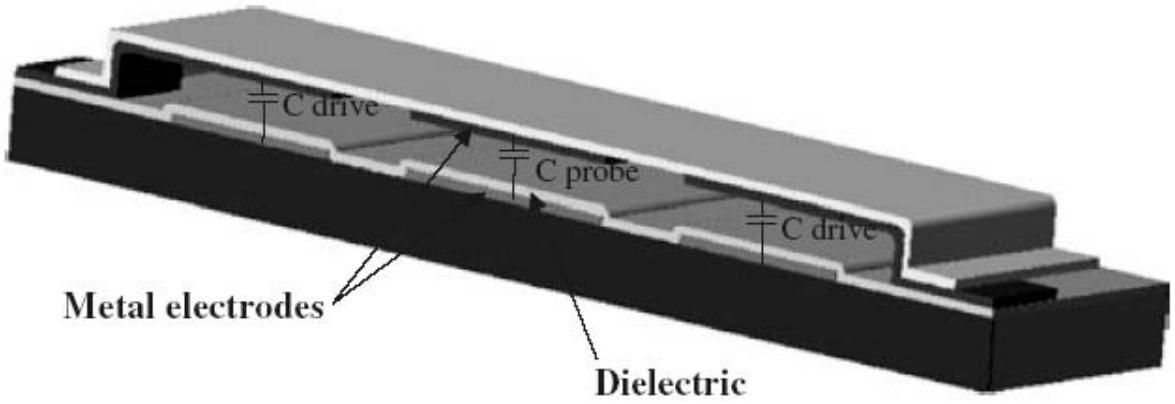

Fig. 5-26. Proposed two-port dielectric charge test structure [40]

This device is a modification of a two-port variable capacitor to be fabricated in the metal/oxide process. The two-port device allows for control of the contact region of the floating capacitor C_{probe} while the actuation voltage is applied to the drive capacitor C_{drive}. The ability to vary voltage, contact area and contact time over the C_{probe} region allows for controlled charge injection. Following a release of the C_{drive} drive voltage, the injected charge and charge retention could be quantified by measuring the pull-in voltage shift using C_{probe} as the drive actuation capacitance [40]. Obviously, this test device does not take dielectric charging without contact into account, which might be a disadvantage.

One could also imagine using one of the methods applied to MOS-capacitor investigations to study dielectric charging. For instance, the voltage ramp method can be used for that purpose [42]. In this method, a voltage ramp generator is used to apply a time varying bias. The resulting displacement current is measured with an electrometer [43]. To quantitatively describe this method, we need the relationship between linear ramp voltage, displacement current, and differential capacitance:

$$I = \frac{dQ}{dt} = \frac{dQ}{dV}\frac{dV}{dt} = C\frac{dV}{dt} \qquad (5.50)$$

Choosing a linear voltage ramp $V = \alpha t$,

$$\frac{dQ}{dt} = \alpha C \qquad (5.51)$$

A modification of this method called “slow ramp method” uses time steps of the order of seconds. Schematic of a measurement setup is shown in Fig. 5-27.

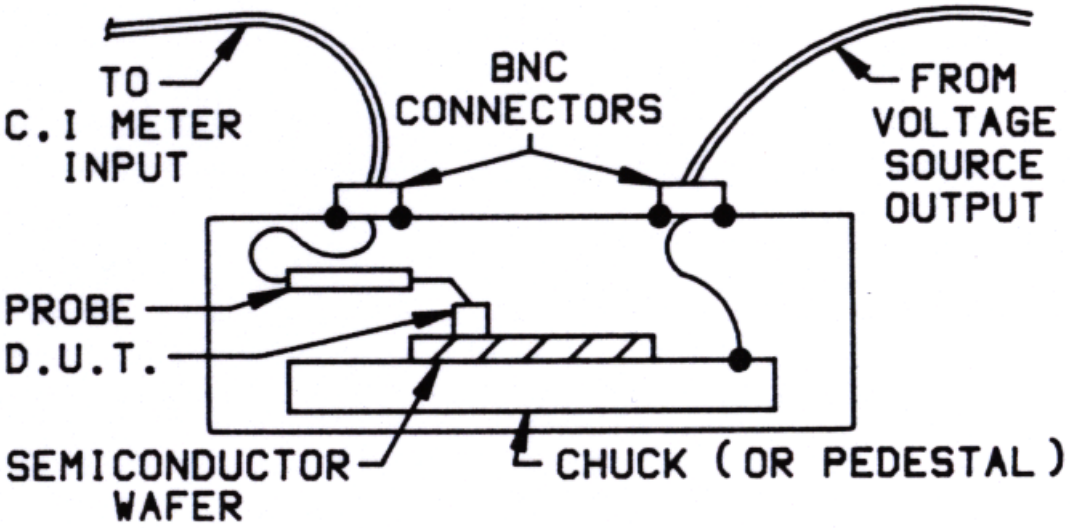

Fig. 5-27. Measurement setup for device on a semiconductor wafer [44]

The device depicted in Fig. 5-28 can be used for such measurements. The current input can be connected to the electrode, and the voltage output to the static bridge structure. This configuration minimises the effects of stray capacitance and noise [44].

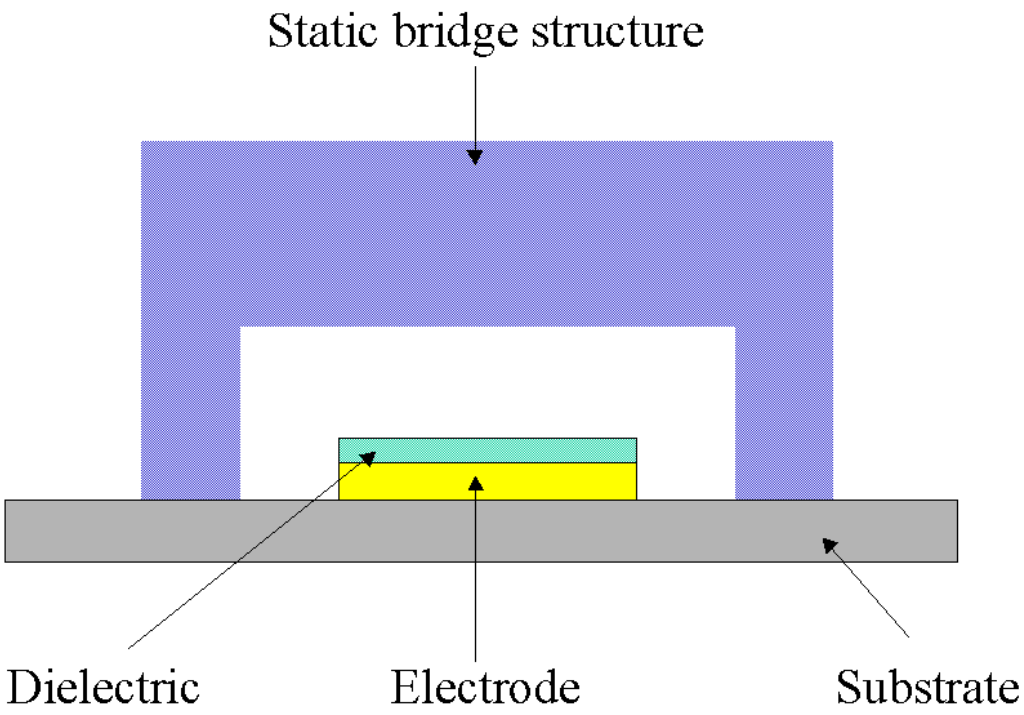

Fig. 5-28. Proposed test device for voltage ramp method.

Another possibility is to use a structure as depicted in Fig. 5-29. In this case a (low-resistivity) Si substrate plays the role of one of the capacitor plates, and the other capacitor plate is directly connected to the measuring device and can be adjusted along the vertical axis. To

prevent accidental intimate contact of the movable electrode with the dielectric (and to set the minimum distance between them), stoppers can be utilised (e.g., deposited polymer), which have a larger thickness than the dielectric. The wafer might also be diced before the measurements.

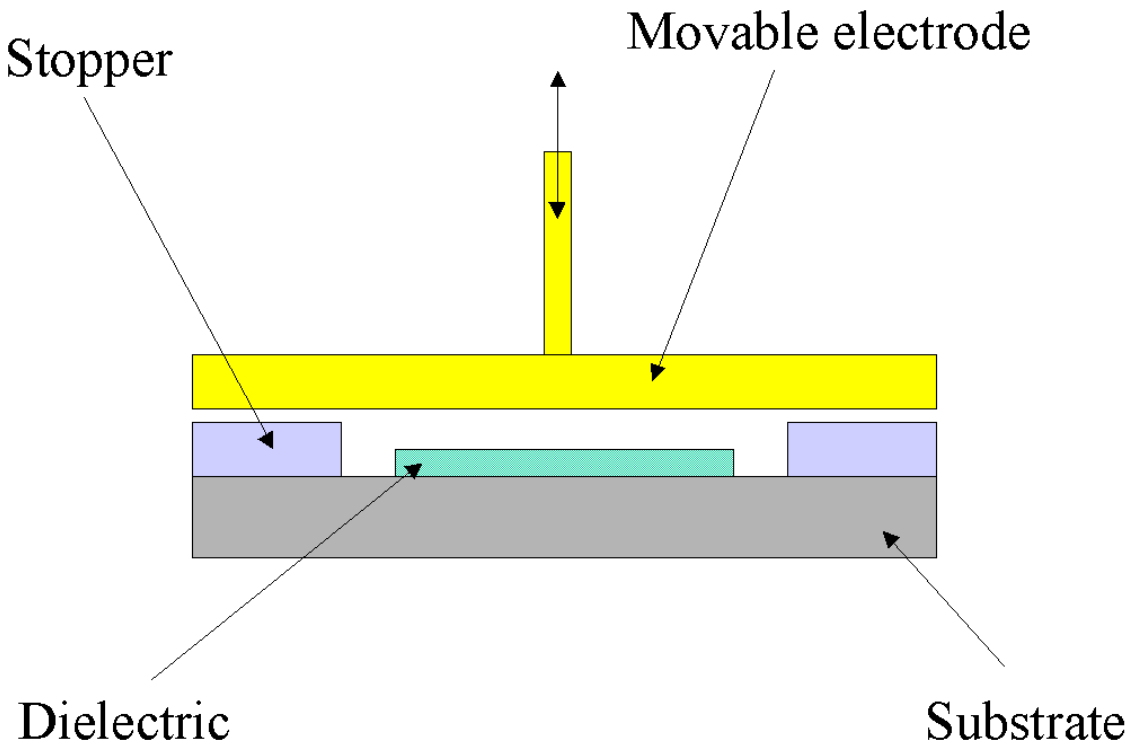

Fig. 5-29. Proposed test device for voltage ramp method.

The charge can be calculated from the measured current, and the capacity from the charge and bias according to Eq. 5.50. The capacity in case of charging will depend on the applied bias, contrary to the ideal case, when the capacity is independent of the bias.

The method requires currents in the picoampere range [43]. Starting from this condition, we can assess the needed dielectric area. Assuming no charge before applying voltage,

$$I = \frac{\Delta Q}{\Delta t} = \frac{\rho \cdot A}{\Delta t} \Rightarrow A = \frac{I \cdot \Delta t}{\rho}, \qquad (5.52)$$

where Δt is the time needed for the dielectric to charge, and ρ is the charge density. Estimating I = 10 pA, Δt = 10 sec, and $\rho = 0.38\times10^{-6}$ C/cm^2, we obtain about 2.6×10^{-4} cm^2, or a square of 162×162 μm. The gap between the electrodes should be in the micrometer or sub-micrometer range to be able to test the dielectric under strong field conditions (of the order of MV/cm). With a gap of 1 μm one would require 100 V to achieve 1 MV/cm.

5.6 Ways of Improvement and Implementation

As was stated in section 5.4, an average capacity ratio of 1.54 at a maximum tuning voltage of 61.5 V DC was achieved with the basic configuration of parallel-plate varactors. Generally, higher capacity ratios and lower actuation voltages are desired (although there is an obvious

limit set by actuation due to RF signal). Several ways to improve the mentioned characteristics are proposed qualitatively and test results are shown.

5.6.1 Capacity Ratio

Within the design of our parallel-plate varactor only one way to increase the capacity ratio can be deduced – increase of the gap to the upper electrodes. If nothing else is changed, this is accompanied by an increase of the actuation voltage, as can be seen from Eq. 5.8 and 5.12 from section 5.2. The additional solution, tensile stress control with suspension structures, was described in section 5.5. The capacity ratio can also be substantially increased, if the two-level membrane concept (see section 2.4) is introduced into the existing design.

To find another way, one needs to remember that one of the limiting factors for C_r is the parasitic capacity. As was mentioned in section 5.4, the capacity ratio is reduced from 1.95 to 1.55 due to parasitic capacity from the substrate. One can think of increasing the C_{var}/C_{par} ratio, where C_{var} is the varactor capacity, and C_{par} the parasitic capacity. This can be achieved either with reducing the parasitic capacity (e.g., through thinning of the substrate under the varactor), or by increasing the varactor capacity. In the latter case, according to Eq. 5.9 from section 5.2, one can play with the dielectric thickness/constant (as far as technology and dielectric charging allow), plates area can be enlarged, or the gap can be reduced. Varactors with extended plate area were tested. To realise this, the membrane was widened in the middle from 100 μm to 180 μm (Fig. 5-30).

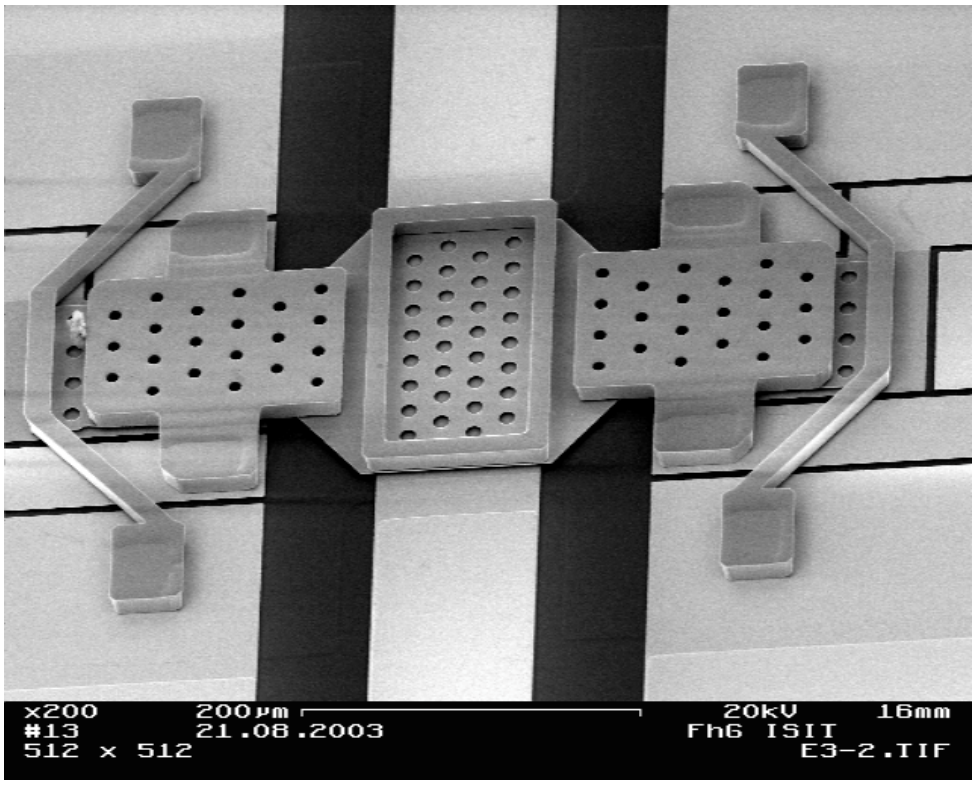

Fig. 5-30. SEM photo of a parallel-plate varactor with extended plate area.

Obviously, changing the membrane width only in the middle required no other design changes, which would be necessary otherwise (e.g., if the whole membrane width were changed, the suspension structures and the electrodes geometry would have to be changed as well). One can see additional feature of this modification – a square frame made of a thick Ni

layer around the centre of the membrane. This was an attempt to combat the increased release stiction (Eq. 5.34 in section 5.5 shows some dependence on width, and therefore a wider membrane leads to a higher stiction probability). Really, it worked: same structures without frame were pinned after the release etch, whereas structures as shown in Fig. 5.30 were free. The area modification allowed us to increase the capacity ratio from 1.54 to 1.65.

5.6.2 Actuation Voltage

Voltages of 60-70 V represent the upper limit of allowed voltages in microsystems technology [45]. Usually voltages lower than 40-50 V are desired. Eqs. 5.8 and 5.12 from section 5.2 show how varactor parameters should be changed in order to achieve lower actuation voltages.

The membrane length extension was tested. Simultaneously, electrode length was increased to strengthen the effect. Dimensions differing from the basic configuration are listed in Table 5-3.

Membrane	Length	600 μm
Lower side electrodes	Length	183 μm
Upper side electrodes	Length	200 μm

Table 5-3. Dimensions of modified parallel-plate varactor.

This allowed to reduce the maximum actuation voltage (for lower side electrodes) from 61.5 V to 46.3 V. Below, CV-curves of varactors, where both capacity and voltage modifications were implemented, are shown (Figs. 5-31, 5-32). The overall capacity change was 50 fF, which corresponds to capacity ratio of 1.653.

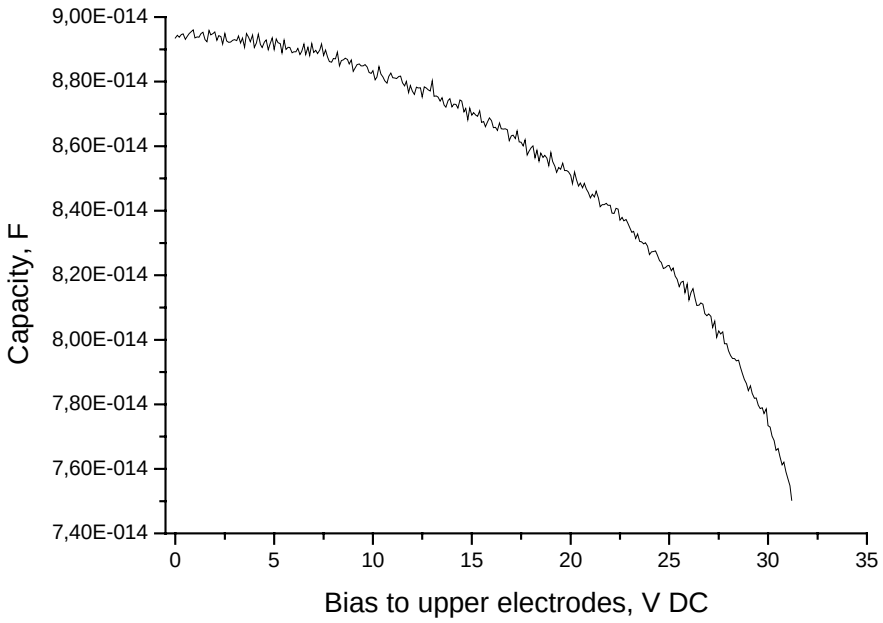

Fig. 5-31. CV-curve of a modified parallel-plate varactor. Bias is applied to upper electrodes. Pull-up voltage is 31.2 V DC.

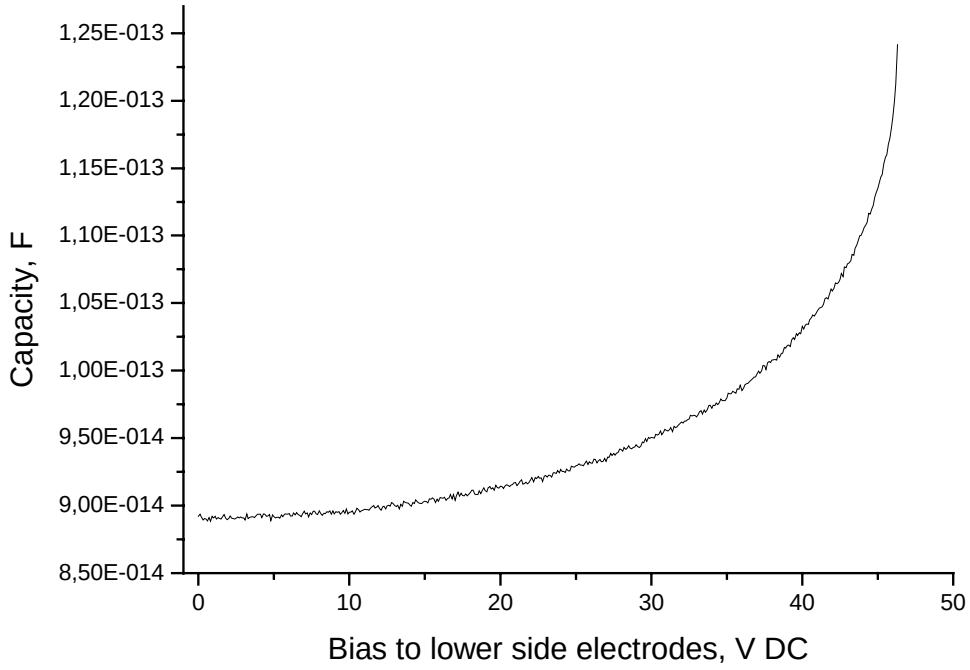

Fig. 5-32. CV-curve of a modified parallel-plate varactor. Bias is applied to lower side electrodes. Pull-down voltage is 46.3 V DC.

One could argue that increasing the area by 1.8 times should lead to a capacity change increase of 1.8 times, i.e. $25 \times 1.8 = 45$ fF. However, 50 fF lies within the variation range set by the technological layer thickness variation.

5.7 Summary

We designed, manufactured and tested the first all-metal parallel-plate varactor of three-plate design known up to date (it is also the second parallel-plate varactor of three-plate type reported at all). Its main characteristics are summarised in Table 5-4 (the measurements were performed at 10 kHz).

Capacity ratio	1.65 with parasitics
Actuation voltage	0-46.3 V DC
Capacity change	50 fF

Table 5-4. Main characteristics of the developed parallel-plate varactor.

The varactor *Q* value is expected to be high due to highly conductive Ni used as structural material.

Main problems met with this varactor type were release stiction due to wet release etching used, high intrinsic tensile stress, and dielectric charging. Solutions for the problems are proposed, as well as a method and test structures for dielectric charging investigation.

6. S-Shape Varactors

In this section design and testing of S-shape varactors will be presented. An intrinsic feature of S-shape varactors is the intimate contact of the movable membrane with the dielectric layer, which separates it from the fixed electrode.

6.1 Precursor

The first attempt to create an S-shape varactor within MELODICT project was design of a varactor called in this work the pre-formed varactor (to distinguish it from the other S-shape varactors) [46] (Fig. 6-1)

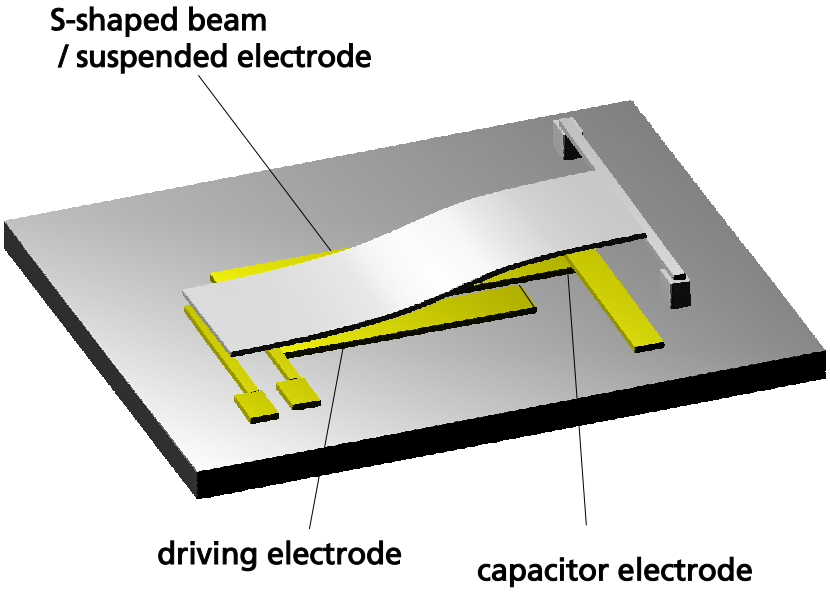

Fig. 6-1. Schematic view of a wide-range tunable capacitor with S-shaped actuator – the pre-formed varactor [46]

One end of the S-beam is fixed on the substrate, the other at an elevated torsion beam. With underlying electrodes the beam is continuously pulled to the substrate in a zipping motion. Thus, the capacitance between the beam and the capacitor bottom electrode is increased linearly in a wide range. Due to the S-shape, there is always a small driving gap and low voltages are sufficient. The shape is fabricated by creating a sacrificial photo-resist layer with continuously variable thickness using the graytone lithography.

Several years ago FhG-ISIT developed a special photolithographic process called graytone lithography which enables to transfer almost any kind of surface profile into photoresist [47]. The UV-exposure intensity can be varied in an almost analog way by changing the diameters of the pinholes in the photomask. Provided that each pinhole in the photomask is less in diameter than the resolution limit of the optical projection system the photomask structures work in the diffraction regime. The projection system however stops the higher diffraction orders and only the zero-order passes the objective and enters the photoresist. The zero order only contains intensity information but no information about the respective structure of the diffracting pinhole. Based on about 400 different pinholes the intensity can be spatially varied in order to achieve the desired photoresist-profile.

Fig. 6-2 shows the process flow for the fabrication of an S-shape actuator, which is a modification of a process described in [47]. First the signal and ground lines are produced by gold electroplating followed by deposition and patterning of an isolating layer (a). Then lithography and electroplating are used to form Ni support posts (b). Thick photoresist is spun on, which serves as a sacrificial layer (c). Graytone lithography transfers an S-shape profile into the photoresist (d). A flexible membrane is produced again by Ni electroplating on top of the sacrificial layer (d). In the final step the sacrificial layer is removed to release the actuator membrane (e).

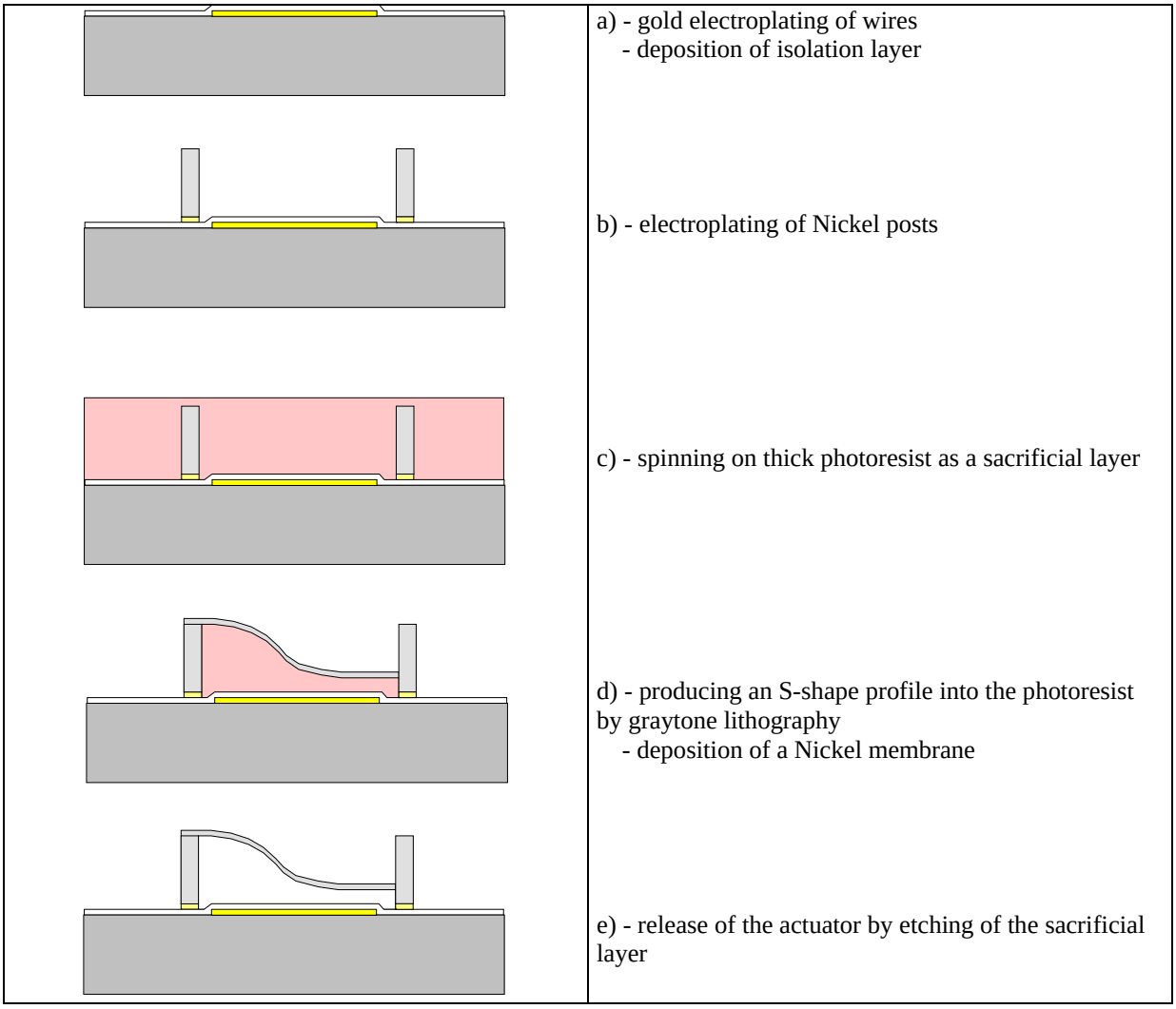

Fig. 6-2. Fabrication process of a pre-formed S-shape varactor.

Unfortunately, the proposed structure was not realisable on available technological equipment: the plasma temperature for dry etching was too high for the Ni varactor structures to tolerate the induced stress. Additionally, very large roughness of Ni surface due to high-T etching process made them hardly usable.

This forced us to change design and technology, as will be described in what follows.

6.2 Design

Two types of S-shape varactors were designed and investigated: a bridge-type varactor and a two-phase varactor.

6.2.1 Bridge-Type Varactor

In essence, the bridge-type varactor is a simple bridge-type structure (very similar to parallel-plate varactor described in section 5) with actuating electrode situated below the whole length of the membrane. The electrode simultaneously acts as the second varactor plate. A schematic side-view and actuation principle is shown in Fig. 6-3.

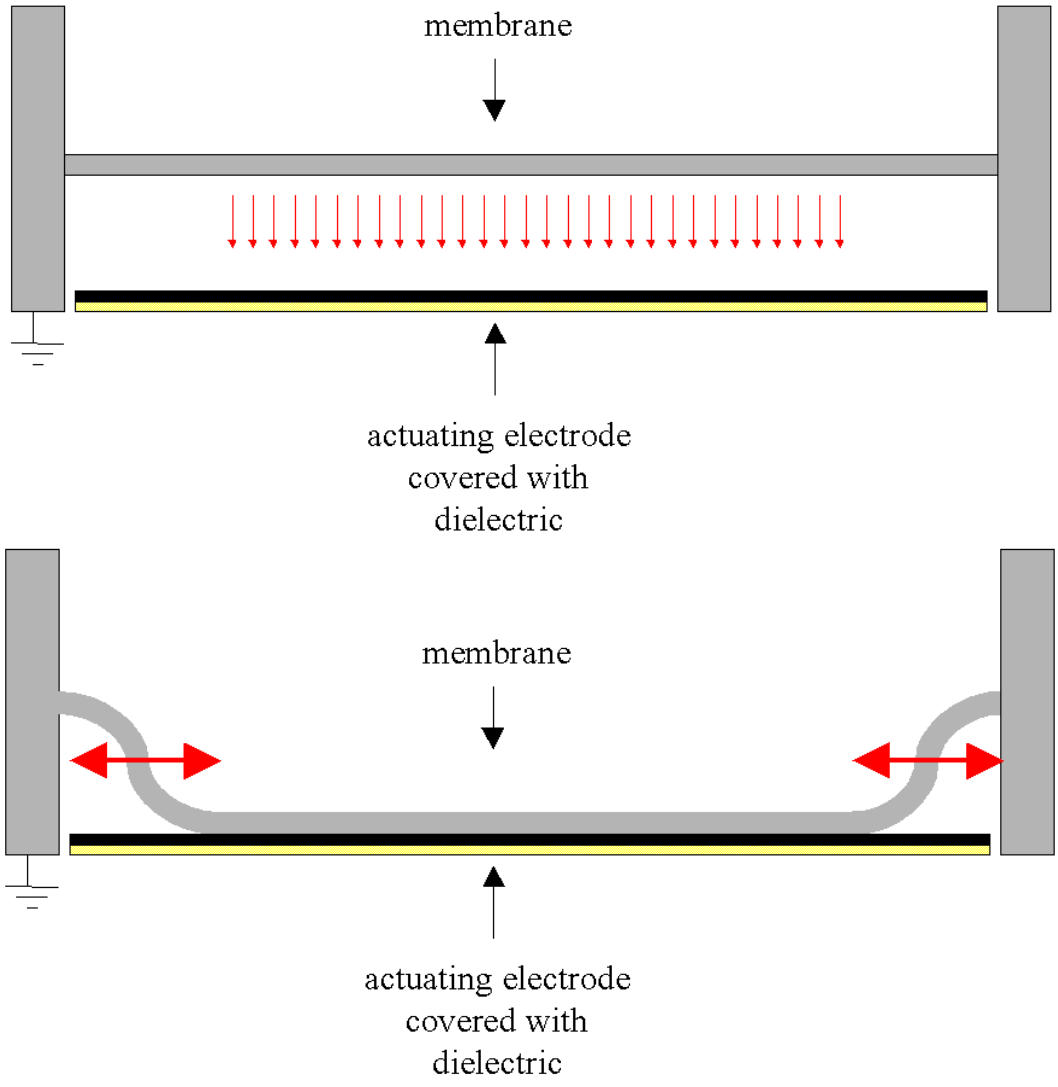

Fig. 6-3. Schematic side-view and actuation principle of the bridge-type S-shape varactor. Initial state (top) and working state (bottom).

A movable membrane is suspended between two posts (special suspension structures are omitted for sake of simplicity) above the long actuation electrode covered with dielectric (length and width of the membrane are equal to those of the electrode). The dielectric layer is unavoidable in this case (contrary to the parallel-plate varactor case), since pull-in is an

intrinsic feature in this case. When a bias is applied to the electrode, the grounded membrane gets attracted and finally falls onto the electrode after pull-in. This immediately leads to formation of two S-shaped parts in the membrane – at both ends. If now the bias applied to the electrode is varied, the attachment length of the membrane also varies, changing the capacity. It is schematically shown in Fig. 6.3 as movement of the S-shaped segments towards the centre and back. Dimensions of the basic configuration are given in Table 6-1.

Membrane	Thickness	1 μm
	Length	600 μm
	Width	100 μm
	Perforation hole diameter (ligament efficiency)	10 μm (0.642)
	Young's modulus (Ni)	170 GPa
Electrode	Width	100 μm
	Length	600 μm
	Dielectric thickness	200 nm
	Dielectric constant (Si_3N_4)	7.5
	Gap	2.5 μm

Table 6-1. Dimensions for the basic configuration of the bridge-type S-shape varactor.

Thickness variation is the same as in presented in Table 5.2 (section 5.1). Below an SEM photo of such a varactor is shown (Fig. 6-4).

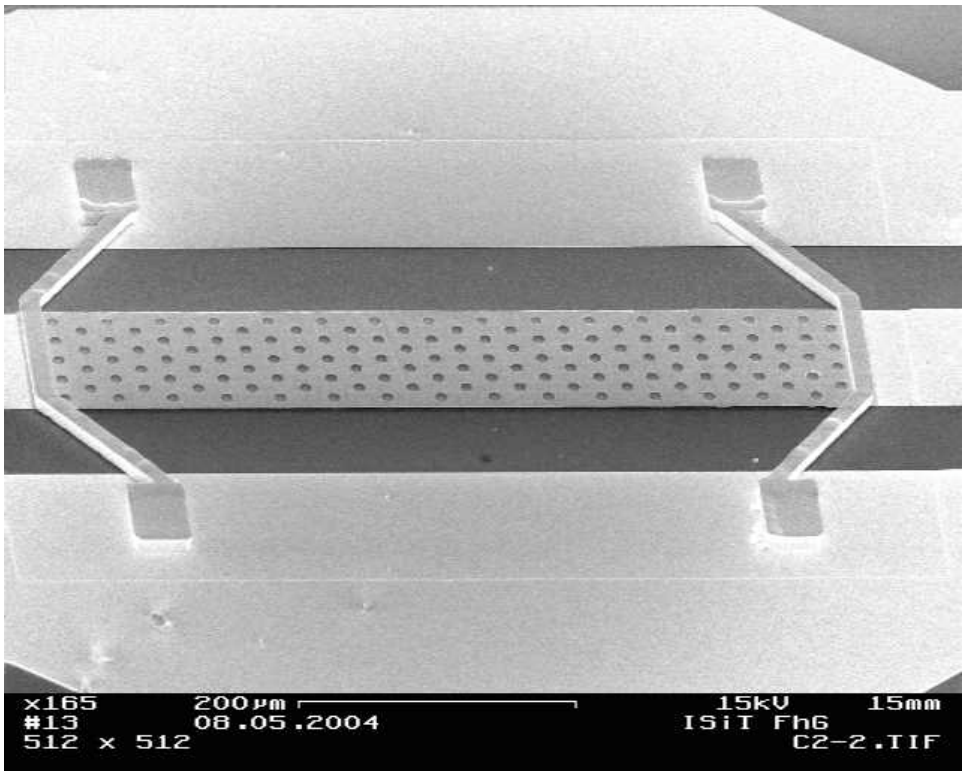

Fig. 6-4. SEM photo of a bridge-type S-shape varactor.

6.2.2 Two-Phase Varactor

The idea of the two-phase S-shaped varactor was inspired by [48], where a simulation of a continuously deflected micromirror was presented (Fig. 6-5)

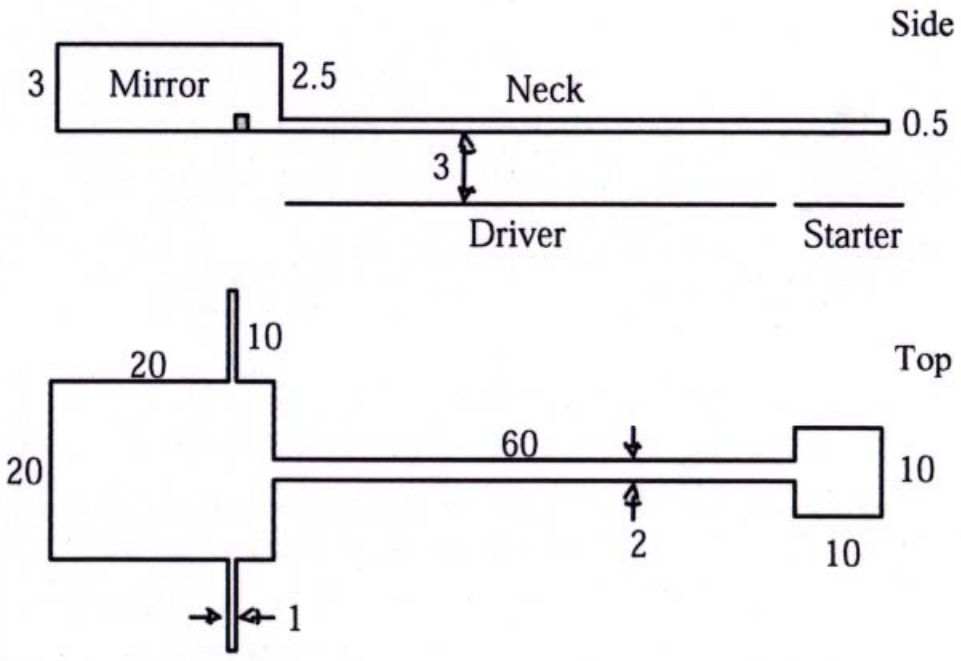

Fig. 6-5. Schematic side- and top views of the continuously deflected micromirror. All numbers in μm [48]

The neck is supposed to be pulled down first by the starter electrode till the end of the neck is attached to the starter. The rest of the neck forms an S-shape and can be continuously attracted or released by the driver electrode. This continuous movement makes the mirror deflect.

In our work this principle was modified to result in a two-phase varactor. Schematic top- and side-views are shown in Fig. 6-6. The varactor membrane consists of two functional parts: the starter-membrane and the working membrane. Below them the corresponding electrodes are situated – the starter-electrodes and the working electrode (Fig. 6-6, top). In the first actuation phase, the starter-membrane is attracted by the starter-electrodes and finally gets attached to them after a pull-down. The actuated starter-membrane brings the end of the working membrane in contact with the working electrode. As a result, the working membrane obtains an S-shape and can be moved with the help of the working electrode (Fig. 6-6, bottom). This brings the desired capacity change.

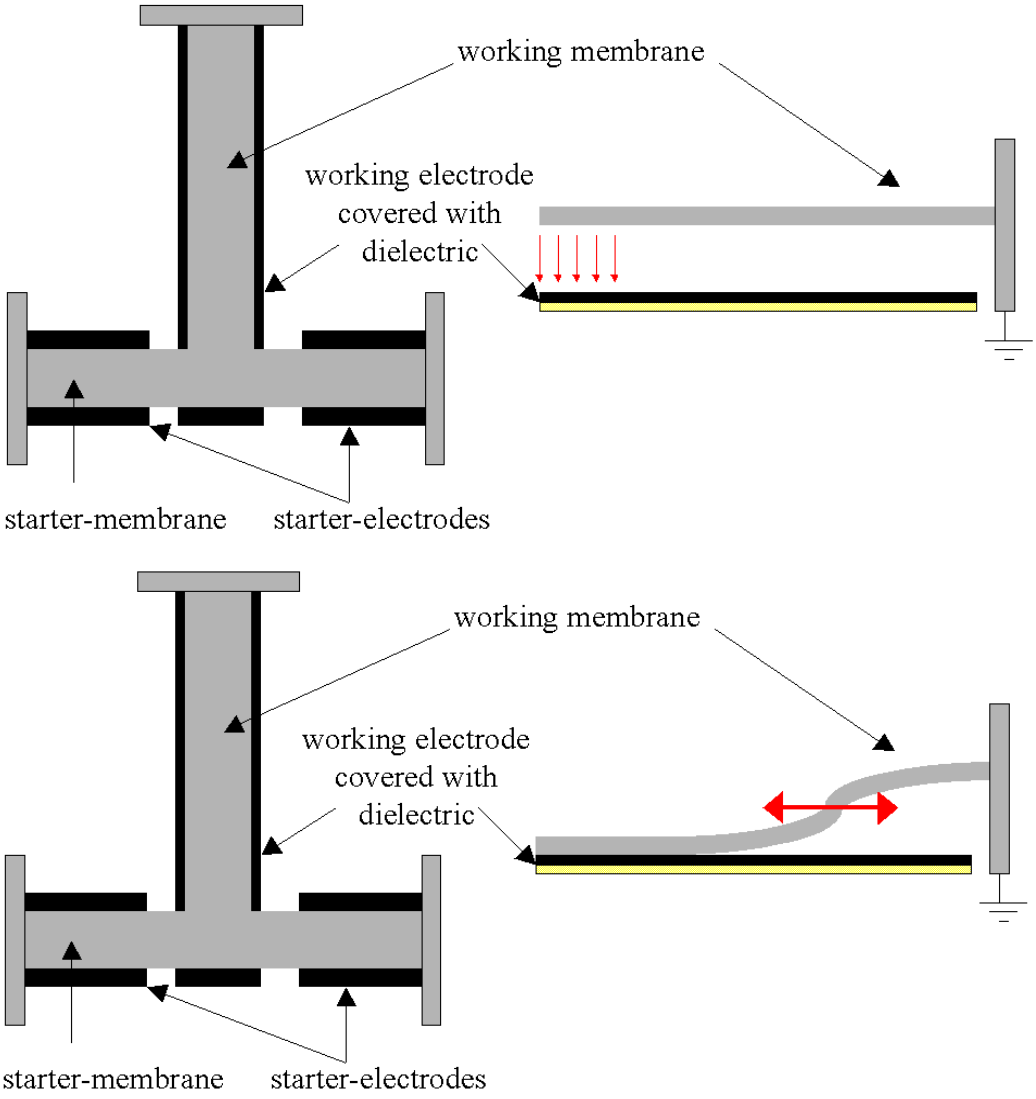

Fig. 6-6. Schematic top- and side views of the two-phase S-shape varactor before (top) and after (bottom) the pull-in of the starter membrane

Dimensions of two-phase S-shape varactor are summarised in Table 6-2.

Working Membrane	Thickness	1 μm
	Length	500 μm
	Width	100 μm
	Perforation hole diameter (ligament efficiency)	10 μm (0.642)
	Young's modulus (Ni)	170 GPa
Starter Membrane	Length	600 μm
	Width	100 μm
Starter electrodes	Length	182 μm
	Gap	2.5 μm
	Dielectric thickness	200 nm
	Dielectric constant (Si_3N_4)	7.5

Table 6-2. Dimensions of two-phase S-shape varactor

The thickness variation is the same as presented in Table 5.2 (section 5.1). Fig. 6-7 shows an SEM photo of a manufactured device. The joint configuration (between the working and the starter membranes) was designed to minimise the starting capacity, i.e. when only the starter membrane is actuated.

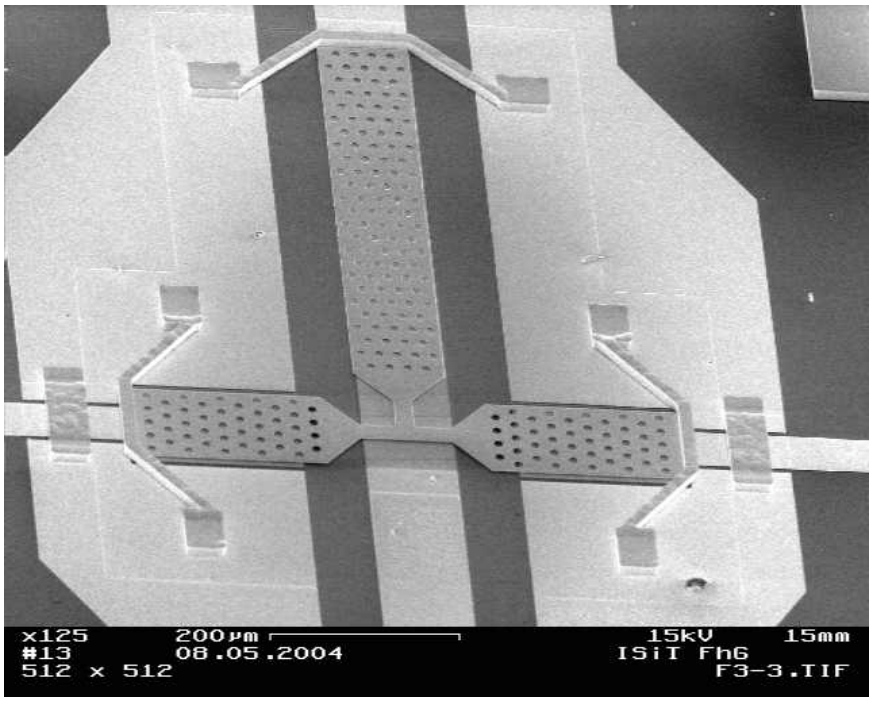

Fig. 6-7. SEM photo of a two-phase S-shape varactor.

6.3 Modelling

Available analytical expressions for the bridge-type varactor will be presented, as well as a discussion regarding the two-phase varactor.

6.3.1 Analytical Modelling For a Bridge-Type Varactor

Analytical considerations analogous to presented in section 5.2 allow to predict the pull-down voltage of a bridge-type S-shape varactor (or find its internal tensile stress, if the pull-down voltage is known, as in our investigation normally is). Eqs. (5.9-5.12) are valid. If the force is distributed along the whole membrane length, then, similar to consideration in section 5.2.3, an integration from *l/2* to *l* should be performed, and the result is

$$k_1 = 32Ew\left(\frac{t}{l}\right)^3 \qquad k_2 = 8\sigma(1-\nu)w\left(\frac{t}{l}\right) \qquad (6.1\text{-}6.2)$$

After the pull-down occurs, the membrane can perform a zipping motion if the applied force is varied (Fig. 6-8).

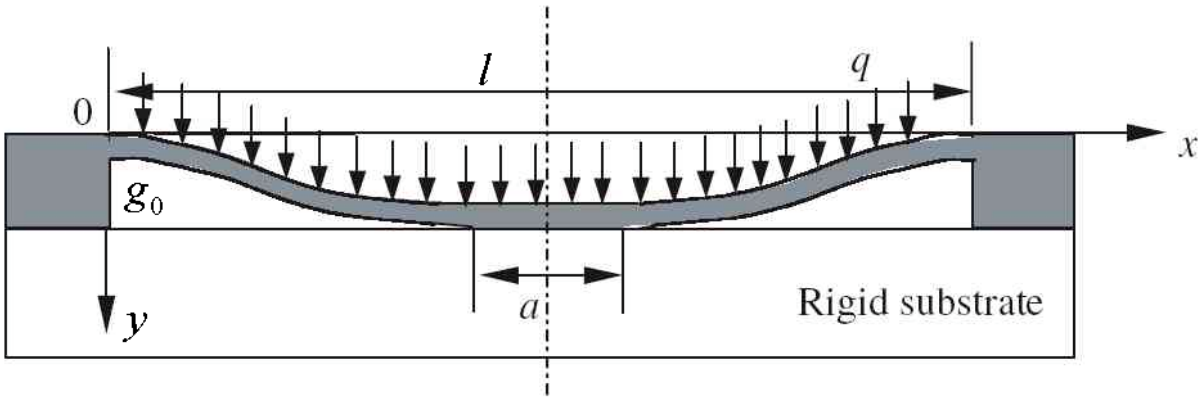

Fig. 6-8. Plate after pull-in [49].

In [49] an expression for contact length (part of the plate in contact with the underlying surface) of a zipping rectangular plate is given:

$$\left(\frac{l}{2}-\frac{a}{2}\right)^4=\frac{6Ewg_0t^3}{q(1-\nu^2)}, \qquad (6.3)$$

where a is the contact length, q is the force per unit length applied to the plate, and the rest of notation is the same as in section 6.2. It is important to notice that the applied force in [49] is the same along the plate, whereas the real electrostatic force (see Eqs. 4.4 and 4.10) depends on the gap between the plate and the plate. Thus Fig. 6-8 could only serve as an approximation. In general, the system can be described analytically, but solved only numerically [30].

There is a lower boundary for the electrostatic force, below which the membrane will return to its original position. The voltage corresponding to this threshold force is often called the release voltage or hold-down voltage. An expression for the hold-down voltage is given in [14]:

$$V_h=\sqrt{\frac{2k_e}{\varepsilon\varepsilon_0 A}(g_0-g)\left(g+\frac{t_d}{\varepsilon_r}\right)^2} \qquad (6.4)$$

$$k_e(g_0-g)\equiv k(g_0-g)+k_s(g_0-g)^3 \qquad (6.5)$$

$$\varepsilon=\begin{cases}1 & (g\neq 0)\\ 0.4-0.8\ (g=0)\end{cases} \qquad (6.6)$$

where k_e is the equivalent spring constant taking into account the stretching component, k_s - the stretching component only applicable to fixed-fixed beams, ε accounts for the reduction in the parallel-plate capacitance due to the roughness of the metal-to-dielectric interface, and the rest of notation is the same as before. Eq. 6.4 is not accurate at $g \cong 0$. The reason is that the mechanical restoring force for the membrane in intimate contact with a dielectric layer is actually not well understood due to adhesion and repulsion forces between the metal and dielectric layers. Thus Eq. 6.4 is rather an approximate assessment of the reduction of the

voltage, required to hold the membrane of a switch down, from the pull-down value. Notes on finite element modelling can be found in Appendix 3.

6.3.2 Qualitative Consideration of a Two-Phase Varactor

While the so called pre-formed structure (see section 6.1) could not be produced with our technology, it was still helpful to perform simulation of this structure. The performed simulation [46] can help to understand the functioning of the two-phase varactor. From the design of the pre-formed varactor, it has some initial gap (0.5 μm in the simulated case; other dimensions are: length – 500 μm, thickness – 1.5 μm, gap at the upper end – 10.5 μm) between the lower end of the membrane and the underlying electrode (Fig. 6-9)

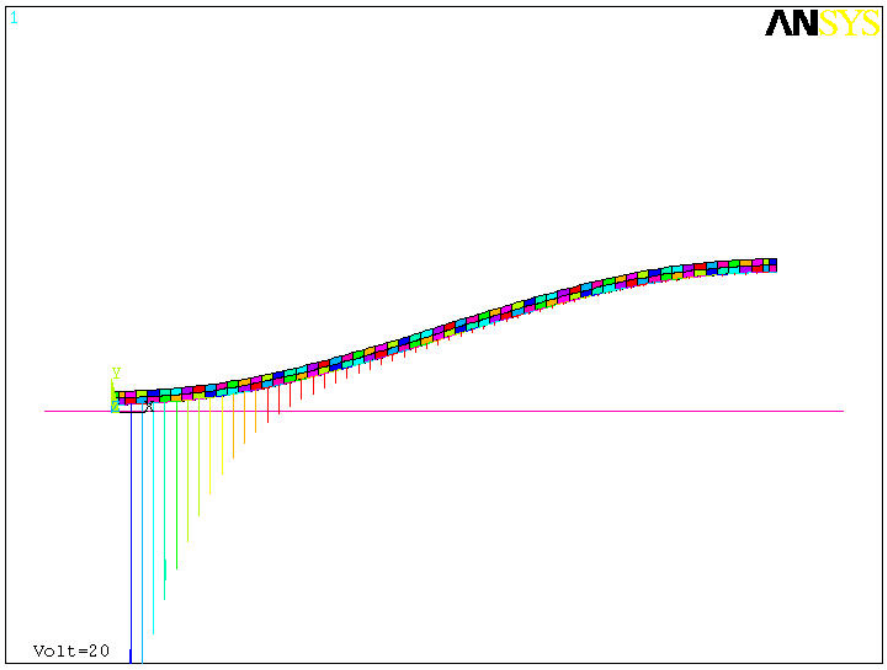

Fig. 6-9. ANSYS screenshot of the modelled (in 2D) pre-formed varactor. The scaling of the vertical axis is exaggerated to show the thickness. The horizontal line corresponds to the level of dielectric covering the electrode. Initial gap at the lower end of the membrane is visible. Vertical lines represent the applied electrostatic force [46]

On the simulated CV-curves (Fig. 6-10) one can clearly see the hysteresis. An important conclusion is that even a small gap at the lower end of the S-shape membrane (instead of zero gap) would lead to hysteretic behaviour (and no continuous curve through the whole actuation voltage range).

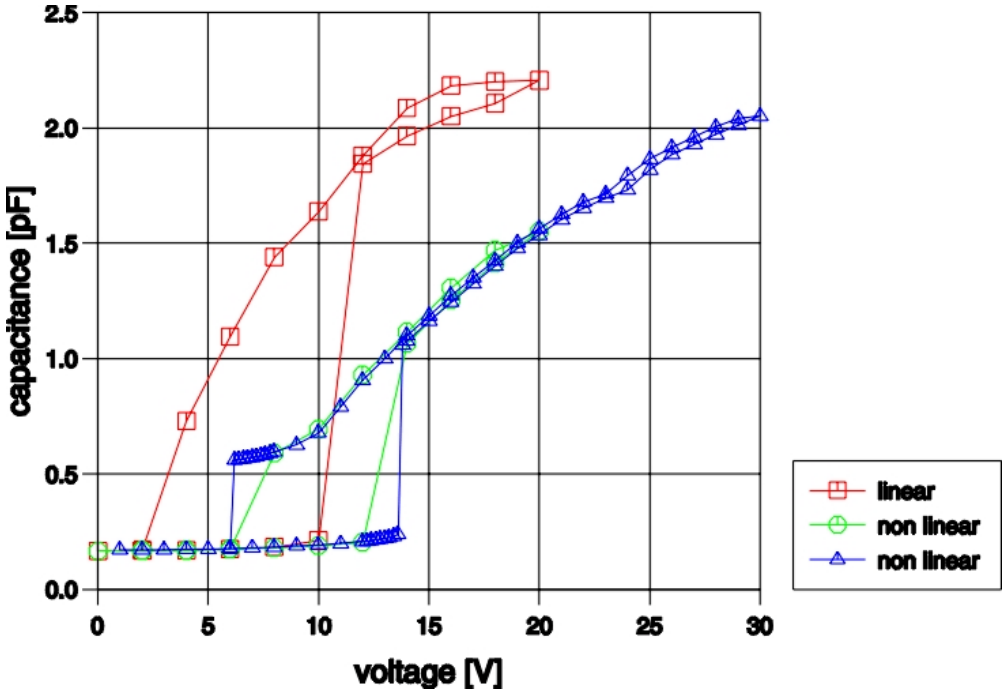

Fig. 6-10. Simulated with different options CV-curves for the pre-formed varactor. Hysteretic character of the curves is seen [46]

6.4 Low-Frequency Measurements

Keeping in mind dielectric charging problems described in section 5.5.3, one could expect to meet them with S-shape varactors, since they are of contact type (there is contact between the movable membrane and the dielectric in working state). The problems were readily seen (see section 6.5.1) and actuation signal was changed from DC to AC (the amplitude of the sensing signal was varied). This limited the measurements to some extent, since maximum effective amplitude of 20 V AC (i.e. the amplitude of the sine function was $20\times\sqrt{2}$ V) was available with the LCR-meter. In all measurements the whole hysteresis curve was scanned: first the voltage was increased from 1 V to 20 V, and then decreased back to 1 V.

6.4.1 Bridge-type Varactor

A typical hystersis curve is shown in Fig. 6-11. Red arrows show the direction of voltage change. Initial capacity amounts to 238 fF, which is the expected capacity plus 25 fF of the parasitic capacity. The capacity change before the pull-in is about 45 fF, whereas 50% capacity change is expected from the theoretical consideration. The reason we do not see the whole 50%-capacity change is that the largest part of it falls upon the “last volts” before the pull-in. In our case, as the pull-in happens between 19 V and 19.5 V, it is obviously in this range, but the step of 0.5 V does not allow us to see it. After all, this capacity change is not of practical interest in S-shape varactors. It is the “back-curve” which is of importance (see section 2.4).

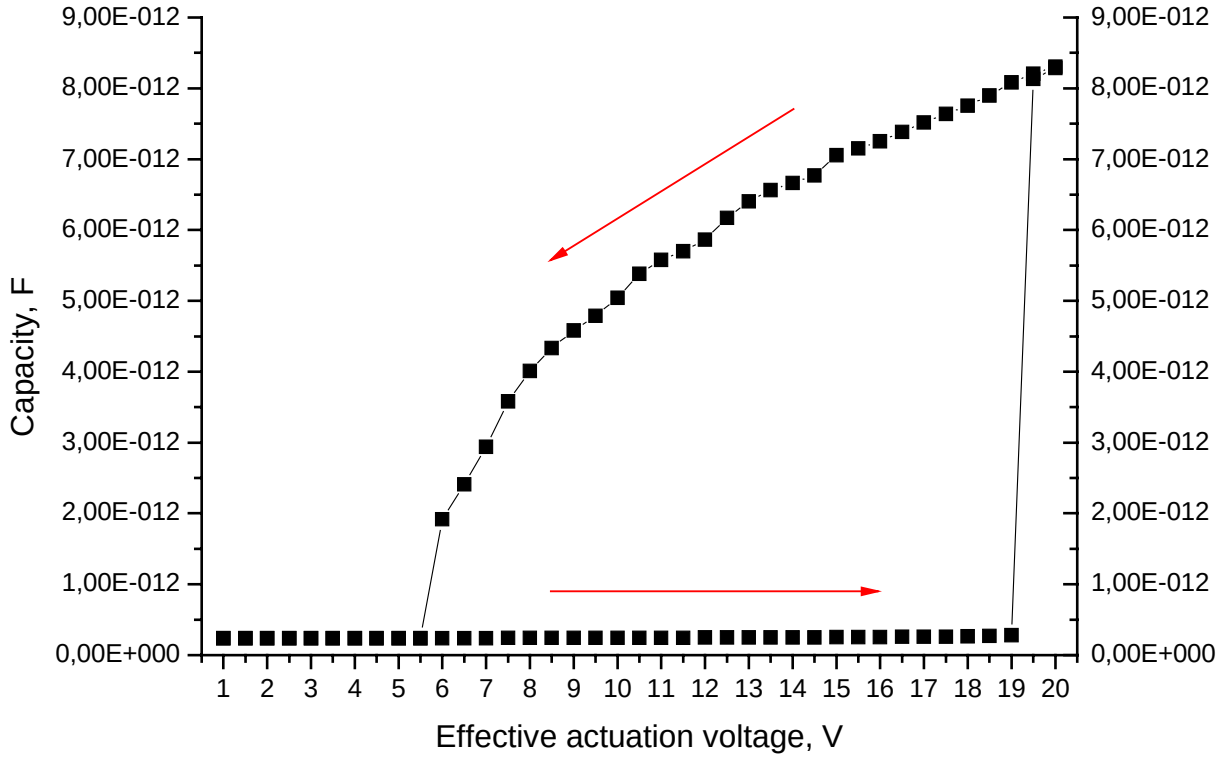

Fig. 6-11. CV-curve of a bridge-type S-shape varactor. Arrows show the increase (left to right) and decrease (right to left) of the applied actuation voltage.

The maximum capacity achieved in our experiment was 8.3 pF at 20 V of effective actuation voltage. The minimum, as can be seen from the plot, was 1.9 pF at 6 V. Together they result in capacity ratio of 4.36. It might be possible to reduce the minimum capacity (and enlarge the capacity ratio), if the voltage step is reduced, but this would be a minor change to the already presented result.

The pull-down voltage value corresponds to a tensile stress of ca. 44 MPa, which is considerably lower than that obtained from optical measurements in section 5.3. This might be attributed to the dielectric charging effect present in optical measurements, as was pointed out in section 6.3. Much less dielectric charging is expected when using an AC signal for actuation, so we expect the value of 44 MPa to be closer to the real stress level. Notes on FEM modelling can be found in Appendix 3.

In one of the measurements we pinned the centre of the membrane in a bridge-like varactor with a contact needle (see section 4.2) to see what happens. Pinning showed an interesting result - a nearly continuous curve for the whole capacity range. The maximum capacity did not change significantly, but the reachable minimum capacity went down to allow for capacity ratio of 9.4 (Fig. 6-12).

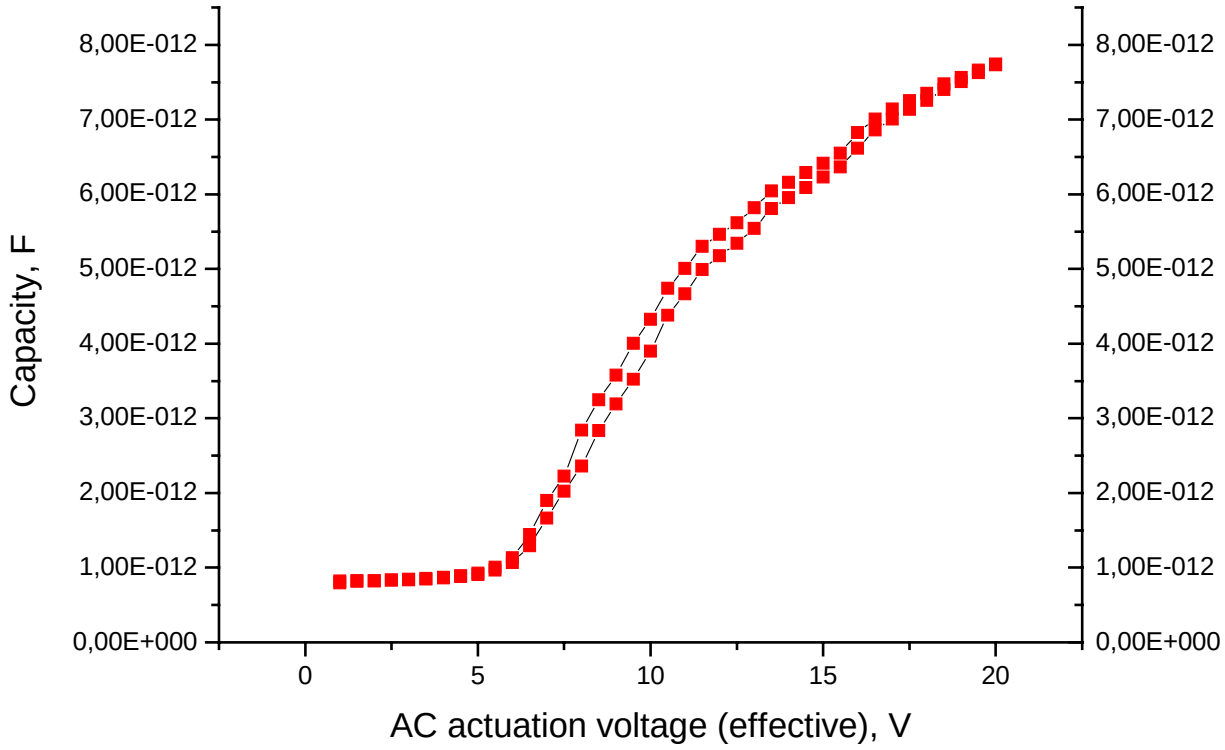

Fig. 6-12. CV-curves of a bridge-type varactor with the membrane free (black) and pinned in the mid (red).

This lead us to the idea of minimising the starting capacity in an S-shape varactor (see section 6.6).

6.4.2 Two-phase Varactor

The idea of the two-phase varactor is to get rid of the pull-down in the working part of the system, and to let the capacity vary continuously through the whole range of the actuation voltage. First, the starter membrane is actuated and pulled down. Then an actuating AC voltage is applied to the working electrode. The result of AC voltage variations is presented in Fig. 6-13. The curve is not completely continuous, there is a step in it. This can be explained as a pull-down of the working membrane due to a residual gap between the end of the working membrane and the working electrode. Probably, the actuation of the starter electrodes did not result in an intimate contact between the end of the working membrane and the working electrode, but in a small residual gap between them, which immediately leads to a pull-down phenomenon (see section 6.3.2).

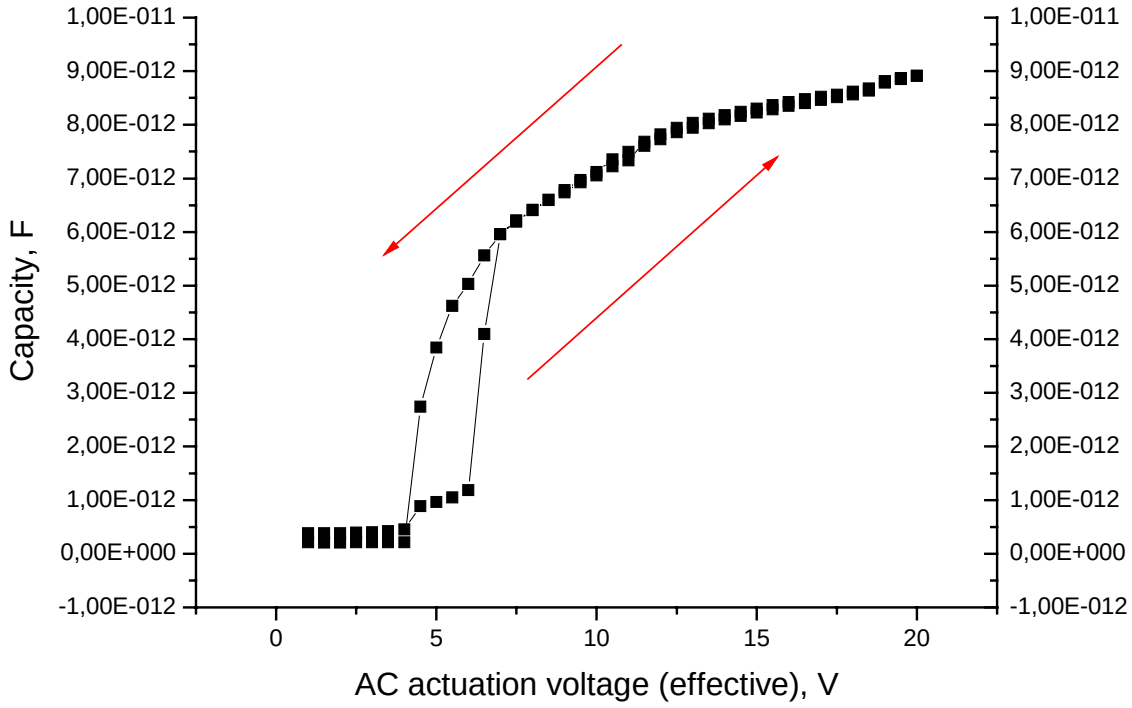

Fig. 6-13. CV-curve of a two-phase S-shape varactor. Arrows show the increase (left to right) and decrease (right to left) of the applied actuation voltage.

Though a completely continuous CV-curve was not achieved, the capacity ratio resulting from the back-curve is 3.29 (C_{max} = 8.9 pF, C_{min} = 2.7 pF). This is smaller than the capacity ratio obtained with the bridge-type varactor.

6.5 Main Problems

When manufacturing and testing S-shape varactors, we met the following problems: release stiction (already discussed in section 5.5), dielectric charging (which forced us to change from DC to AC actuation), reduced capacity, and in-use stiction. The latter three will be discussed below.

6.5.1 Dielectric Charging

Dielectric charging under DC-actuation posed a large problem for the S-shape varactors. Intimate contact of the membrane with the dielectric is part of the working principle, unlike for the parallel-plate varactor. Charging will be illustrated on the two-phase varactor example. In the case of starter electrodes (Fig. 6-14), charging lead to a very high hold-down voltage of 105 V, whereas the pull-down voltage was only about 40 V. Application of AC voltage to the starter electrodes resulted in serious capacity variation depending on frequency and amplitude of the applied signal. The substrate must be responsible for this effect.

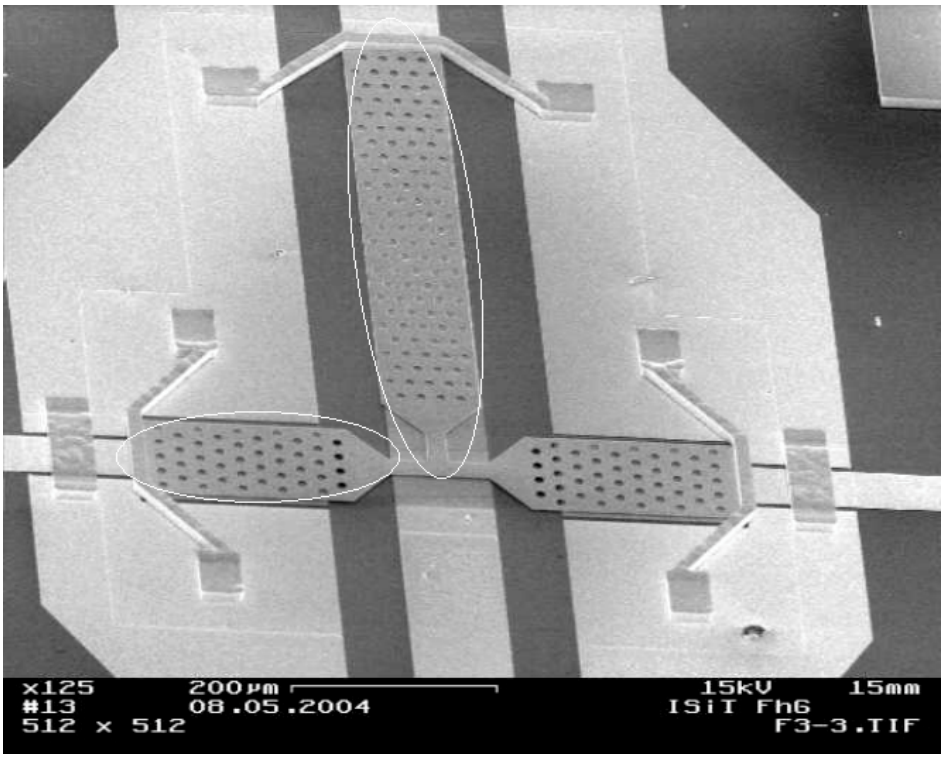

Fig. 6-14. Dielectric charging affected starter and working electrodes in two-phase varactors.

The working electrode could not function in the designed way at all, when supplied with DC voltage. In Fig. 6-15 a CV-curve of a two-phase varactor supplied with DC voltage can be seen. This was the reason to change to AC voltage, where charging is much less pronounced.

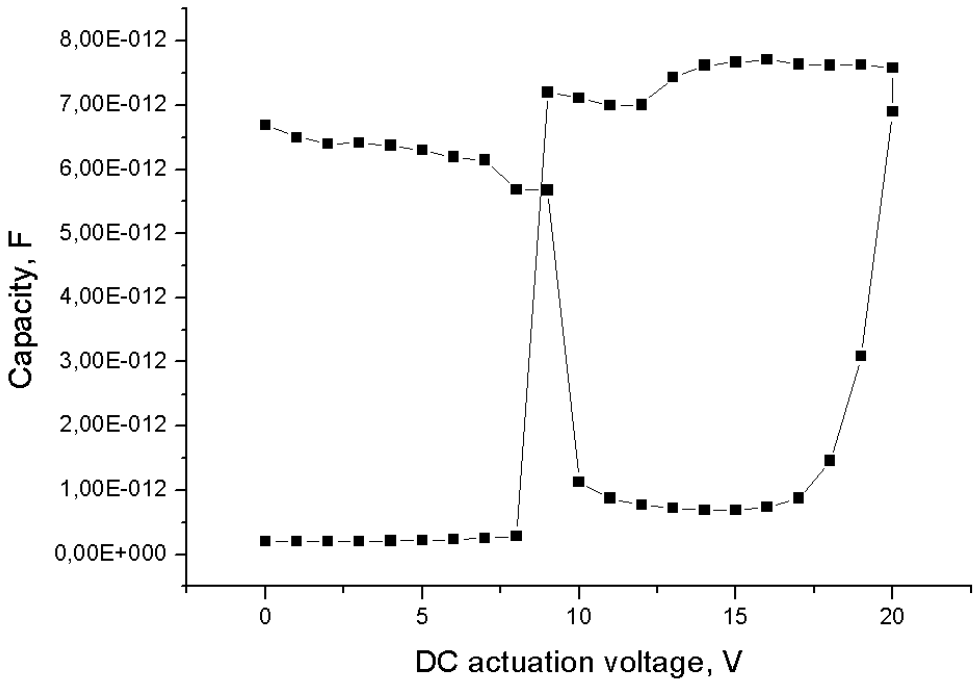

Fig. 6-15. CV-curve of a two-phase varactor when supplied with DC actuation voltage.

There seem to be two solutions to this problem if one wants to use DC voltage: to look for a dielectric with negligible charging or to decrease the dielectric area (trade-off – reduced absolute capacity). The latter can actually be combined with the former, since dielectric charging poses a serious problem for high-*C* MEMS varactors and switches (see section 5.5.3).

6.5.2 Reduced Capacity

According to the simple parallel-plate capacity formula like Eq. 2.1, one would expect higher capacity values than those reported in sections 6.4.1 and 6.4.2. Let us consider the bridge-type varactor from section 6.4.1. With the help of a video-camera (see section 4.2) one could see that at an applied voltage of 20 V, about 50 μm of the membrane length at each end were still free. That means that about 500 μm of the membrane length were in contact with dielectric. Taking the surface area reduction due to perforation holes (see section 3.2) into account, one calculates 14.3 pF, whereas only 8.3 pF are seen in Fig. 6-11. Thus the measured capacity is only 58% of the expected value. More accurate measurements were performed with the help of the optical setup (see section 4.1). From the interferometer profiles of S-shape varactors one could read the length of the membrane part in contact with dielectric and compare it with the capacity measured with LCR-meter. Fig. 6-16 shows capacity per unit of membrane length data obtained for different actuation voltages. The average value amounts to 17.7 fF/μm.

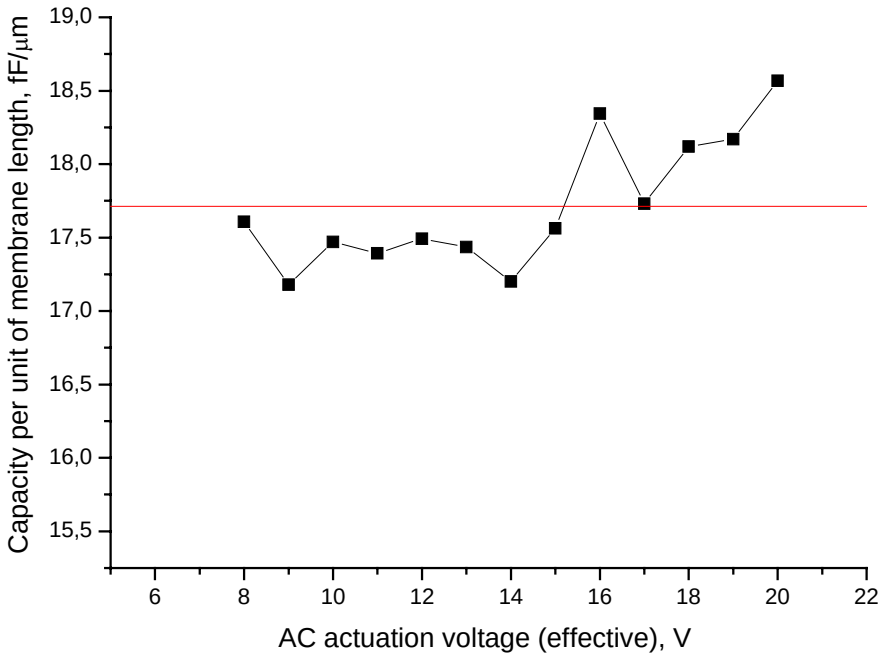

Fig. 6-16. Capacity per unit of membrane length for different actuation voltages. Average level is shown with red line.

The same parameter calculated (as above) for the ideal case is 28.4 fF/μm, i.e. the real capacity is 62% of the ideal value.

The reason for the capacity reduction is the roughness of the surfaces in contact – Ni surface and SiN surface. Roughness values were measured with a Dektak profilometer. The outer Ni

surface was measured due to difficulties related to measuring the inner surface (which contacts the dielectric in reality), and their similarity is assumed. The profiles are shown in Fig. 6-17.

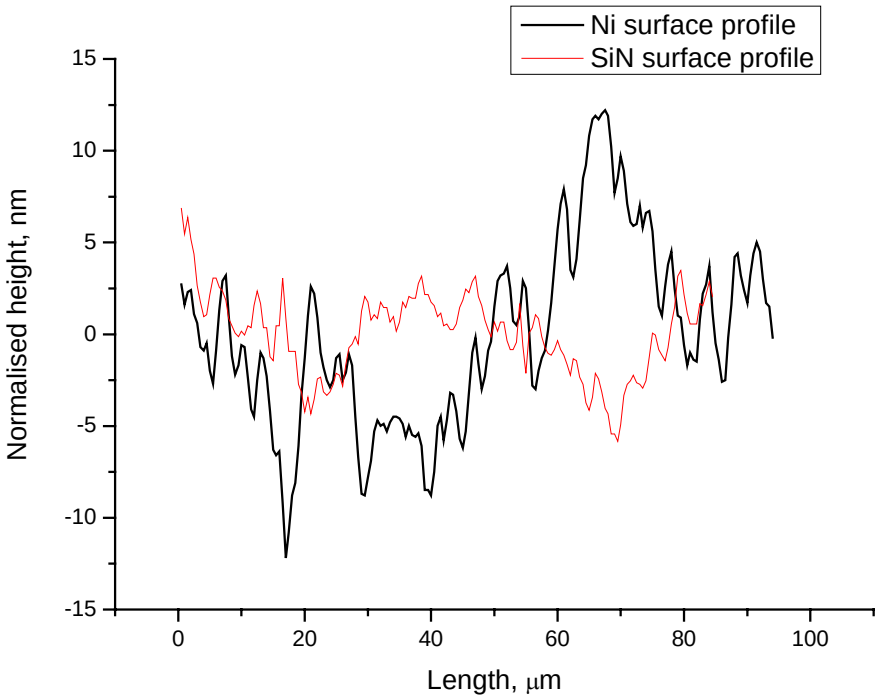

Fig. 6-17. Surface profiles of Ni and SiN measured with a profilometer.

One can immediately see that the Ni surface is much rougher than dielectric surface. To assess the distance between the surfaces when they come into contact with each other, we first used a graphical method. The curves were moved with respect to each other to obtain the minimum and the maximum possible separation. The results are shown in Fig. 6-18 and 6-19.

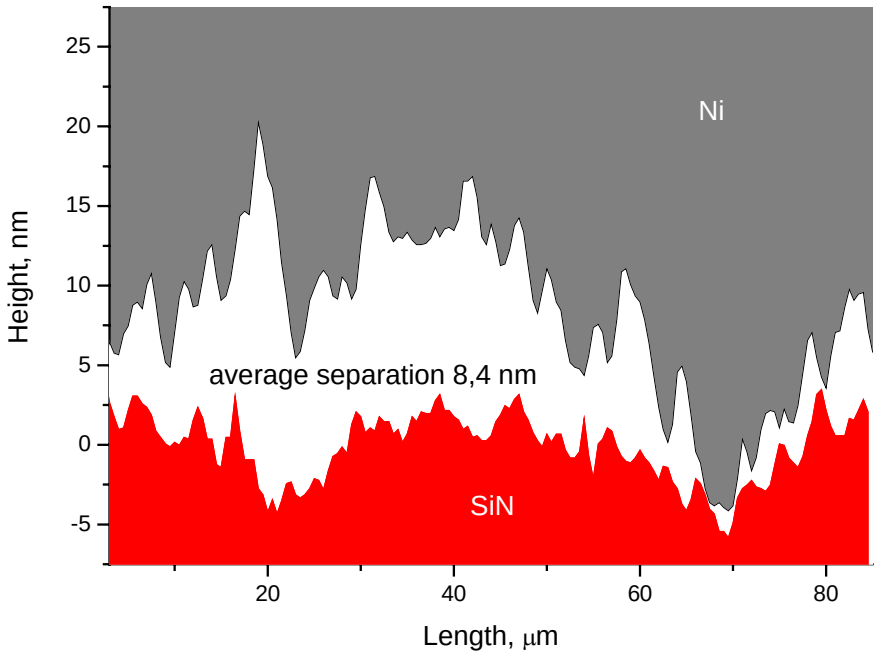

Fig. 6-18. Combination of curves from Fig. 6-17 with minimum separation between surfaces.

Combining the curves to achieve minimum separation between the surfaces lead to average separation distance of 8.4 nm.

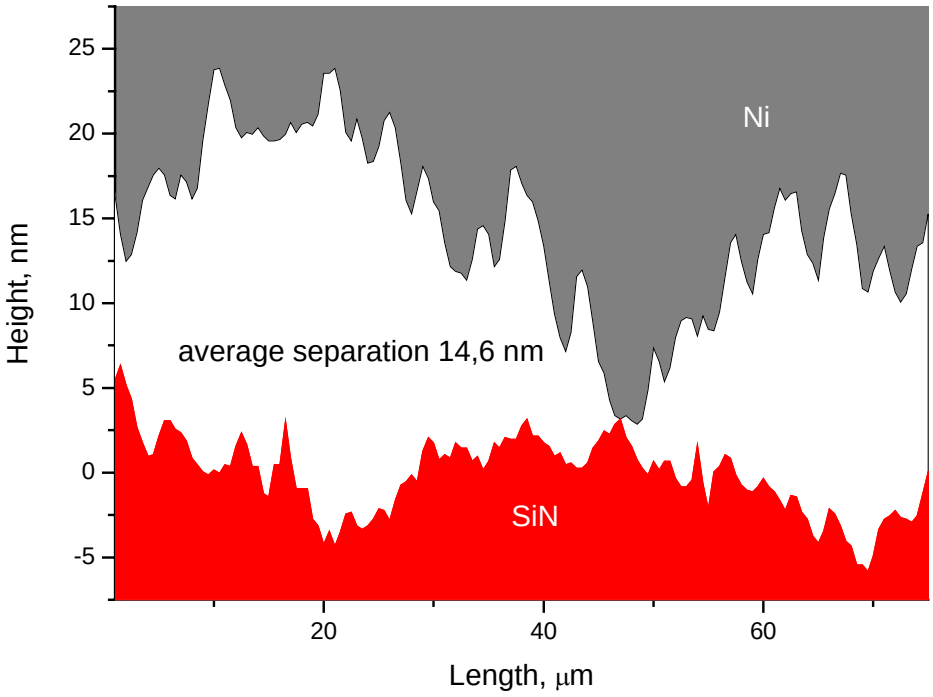

Fig. 6-19. Combination of curves from Fig. 6-17 with maximum separation between surfaces

Combining the curves to achieve maximum separation between the surfaces lead to average separation distance of 14.6 nm.

To assess the separation analytically, one often assumes that one of the surfaces is perfectly flat, and the other is rough [14] (which is close to the situation observed here). The variation parameter in this case is the contact area. If it is assumed to be 50% of the total area, then the resulting capacity is

$$C_{rough} = C_{gap} + C_{nogap} = \frac{1}{2}\frac{\varepsilon_0 A}{\left(g + \frac{t_d}{\varepsilon}\right)} + \frac{1}{2}\frac{\varepsilon_0 \varepsilon A}{t_d} = \frac{\varepsilon_0 A}{2}\left(\frac{1}{g + \frac{t_d}{\varepsilon}} + \frac{\varepsilon}{t_d}\right) \quad (6.7)$$

If one compares the ideal capacity with C_{rough}, one obtaines

$$\frac{C_{rough}}{C_{ideal}} = \frac{1}{2}\left(1 + \frac{1}{1 + \frac{\varepsilon \cdot g}{t_d}}\right) \quad (6.8)$$

$$g = \frac{t_d}{\varepsilon}\left(\frac{1}{2\frac{C_{rough}}{C_{ideal}} - 1} - 1\right) \quad (6.9)$$

With given parameters the separation should be 80.2 nm, which is rather unrealistic even if we assume that the inner Ni surface is considerably rougher than the outer one. A better approximation is achieved if 0% contact area is assumed (which is realistic if one takes a look at the roughness plots). In this case

$$g = \frac{t_d}{\varepsilon}\left(\frac{1}{\frac{C_{rough}}{C_{ideal}}} - 1\right) \quad (6.10)$$

and the calculation delivers a separation value of 15.5 nm, which is very close to the maximum separation obtained with graphical method.

6.5.3 In-Use Stiction

This problem will also be illustrated with the example of the two-phase varactor. In-use stiction reveals itself in that part of the working membrane (Fig. 6-20) that stays in contact with the working electrode even when no voltage is applied to it.

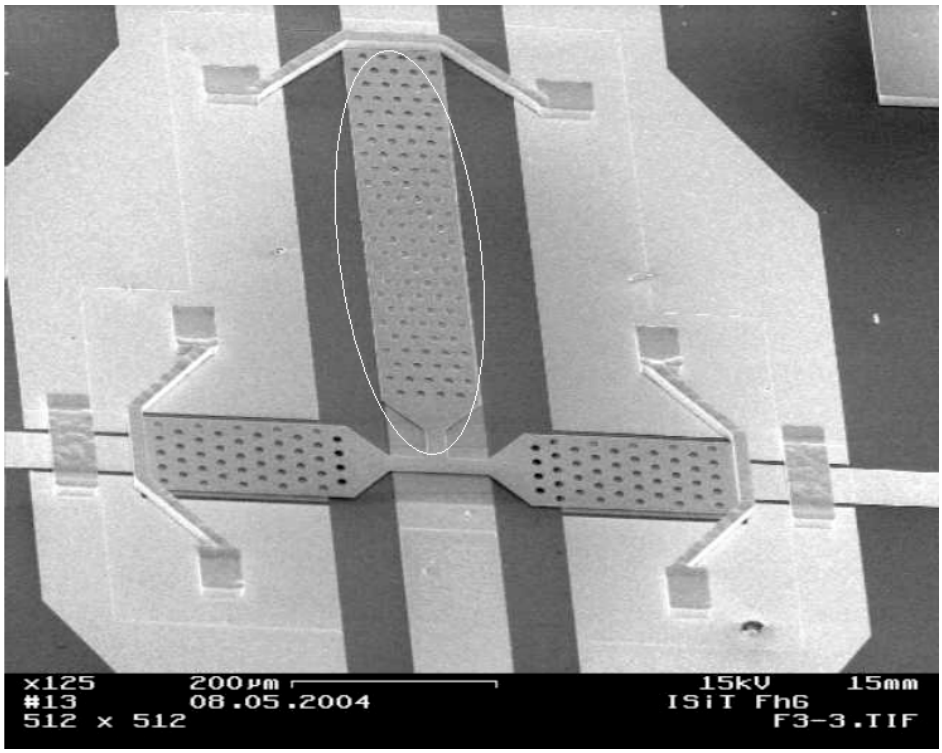

Fig. 6-20. In-use stiction affects the working membrane.

On the CV-curve one can see a residual capacity at the end of the back-curve (Fig. 6-21).

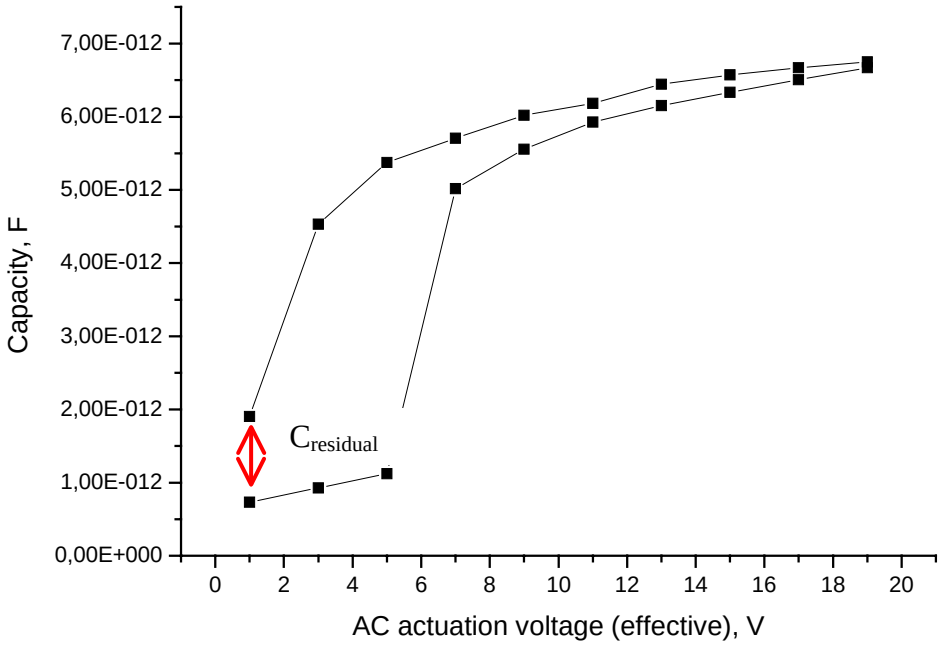

Fig. 6-21. In-use stiction is seen in CV-curves as residual capacity when the voltage is reduced to the initial value.

Researchers see several reasons for the in-use stiction: capillary forces (if operated in environment with humidity), van der Waals forces, electrostatic forces (in case of charging), H-bond forces [39], and even the elusive Casimir force [50].

Capillary forces can be eliminated in a humidity-free environment. Solutions also include decrease of dielectric area (i.e., the contact area) with trade-off of decreased capacity, and increase of membrane stiffness with trade-off of increased actuation voltage.

6.6 Ways of Improvement

Although the S-shape varactors demonstrate considerable capacity ratios, they are still below the targeted values of $C_r = 10$.

6.6.1. Bridge-Type Varactor

The actuation voltage of 20 V used in our experiments is low enough to set the voltage reduction as a secondary improvement target. The primary goal is to enlarge the capacity ratio. As was pointed out in section 6.4.1, it could be done through reducing the minimum capacity. One could speculate that it is possible simply through narrowing the membrane in its central part, which forms the minimum capacity. However, this would also reduce the mechanical stiffness of the membrane, and a 3D simulation is needed to prove this method.

6.6.2. Two-Phase Varactor

Annealing experiments already discussed in section 5.5.2 suggest an interesting auxiliary actuation mechanism for the starter-membrane of the two-phase varactor. As we experienced from the annealing measurements, the membranes gain compressive stress upon annealing at elevated temperatures. We also noticed that the membranes first tend to buckle downwards, and only then – upwards. The first effect can be explained as a consequence of asymmetric (in vertical direction) fixation conditions. The latter must be due to snapping of the membrane when the buckling amplitude gets larger than the gap to the substrate. The first-step buckling (when the buckling amplitude is smaller than the gap to the substrate) can be used to either reduce the actuation voltage of the starter membrane, or to completely replace the electrostatic actuation of the starter membrane. The latter means that a certain annealing temperature has to be found, at which buckling brings the centre of the starter membrane in contact with the underlying layer (and simultaneously – the end of the working membrane in contact with the working electrode, thus creating the S-shape of the working electrode). One could argue that annealing also increases the compressive stress in the working membrane. But we should keep in mind that the working membrane is not a fixed-fixed membrane. It is fixed at one end, but has certain freedom of lateral movement at the joint with the starter membrane, which allows to release at least some of the arising stress.

However, the described buckling of the starter membranes was not observed in our experiments. We think that this is due to specific design of our starter membrane, where the central part is narrower (and therefore mechanically weaker) than the rest of the membrane. This leads to stress relaxation in this central part, whereas the rest of the membrane has lower compressive stress.

6.6.3 Cross-Like Structure

Measurement with the needle described in section 6.4.1 gave us a hint how to reduce the minimum capacity. This can be achieved with a cross-like structure. Fig. 6-22 shows a schematic top-view of the proposed structure.

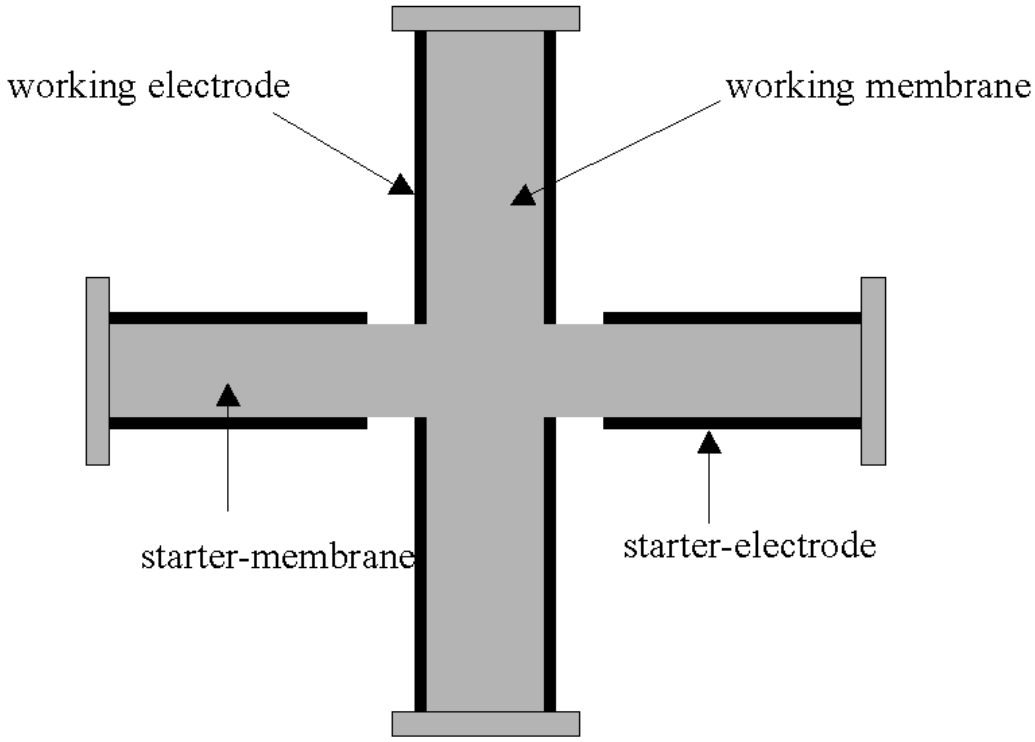

Fig. 6-22. Schematic top-view of the proposed cross-like structure.

It is to some extent a hybrid of already developed S-shape varactors. It includes a starter-membrane, which should be pulled down with starter-electrodes, and which should bring the centre of the working membrane down like the needle. Thus we hope to get a smaller minimum capacity and increase the capacity ratio.

6.7 Summary

Two types of S-shape varactors were designed, fabricated, and tested for the first time. Some modelling considerations are presented. They allowed to correct the internal stress value obtained in section 5.3. In low-frequency measurements (10 KHz) they showed high capacity ratios: 4.36 and 3.29 for the bridge-type and the two-phase type, respectively, at low actuation voltage of 20 V of equivalent voltage. The results are summarised in Table 6-3.

	Bridge-Type Varactor	**Two-Phase Varactor**
Capacity ratio	4.36	3.29
Actuation voltage	0-20 V equivalent	0-20 V equivalent
Capacity change	6.4 pF	6.2 pF

Table 6-3. Main characteristics of the developed S-shape varactors.

The varactors are actually capable of higher capacity ratios, but the maximum actuation voltage was limited by the measurement equipment. The capacity ratio is very sensitive to the minimum capacity value. Thank to high absolute capacity values (several picofarads), the parasitic capacity could hardly affect the characteristics. Problems met when fabricating and testing the devices are described with tested and possible solutions. Concept of a cross-like structure aimed at increasing the capacity ratio in excess of 4.36 is presented.

7. Conclusion

In the work presented three surface micromachined all-metal electrostatically driven varactors were designed, fabricated, and tested at low frequency (10 kHz): a parallel-plate varactor and two S-shape varactors. In the design of all the varactors special suspension structures were used, which allow control of the internal stress in membranes of the varactors.

A capacity ratio of 1.65 (including parasitics) was achieved with the parallel-plate varactor at a maximum actuation voltage of 46.3 V DC (absolute capacity values of the order of tens of femtofarads). A capacity ratio of 4.36 (including parasitics) was achieved at a maximum AC actuation voltage equivalent to 20 V DC (absolute capacity values of the order of picofarads) with bridge-type S-shaped varactor, and a capacity ratio of 3.29 at the same actuation conditions with the two-phase S-shape varactor. The latter two capacity ratios are not limited by the devices themselves, but rather by the actuation voltage limit set by the equipment used.

Several problems, typical for MEMS, were encountered during investigation. Among them are release stiction (typical for wet release etch), high tensile stress in the membranes, roughness of the contacting surfaces, and in-use stiction due to complex attracting forces at the metal-dielectric interface. Ways to avoid some of them were discussed. Probably the severest one is the dielectric charging under strong field conditions. It leads to actuation voltage shifts in the case of parallel-plate varactors and can prohibit functioning of S-shape varactors. An AC actuation allows reduction of dielectric charging as compared to DC actuation. However, often DC actuation is desired, and therefore dielectrics not prone to charging have to be found. A method for such an investigation was proposed, along with possible test structures.

All the described varactors have surpassed the lower target value for the capacity ratio - C_r = 1.3. However, none of the devices could demonstrate a capacity ratio close to the upper target ratio C_r = 10. Methods to increase the capacity ratio for all varactor types are proposed. It seems that the S-shape varactors have more potential in this respect than the parallel-plate varactors. Not only do they provide a higher capacity ratio, but also higher capacity values. The actuation voltage is also lower for S-shape varactors, but it can also be decreased in the case of the parallel-plate varactors. Although parallel-plate varactors are not very likely to achieve the aimed for capacity ratio, they could find application in systems, where only fine tuning and small capacities are required. The advantage of parallel-plate varactors is the absence of a contact between surfaces, which could provide large life-times. On the contrary, S-shape varactors intrinsically require a contact of working surfaces, which can be a limiting factor for the varactors life-time. The investigation performed indicates that capacity ratios of about ten are possible to achieve with S-shape varactors. For that the applied actuation voltage should be increased above 20 V and the minimum capacity should be reduced. However, further work is required for a realisation of it.

Appendix 1. Stress Modelling

Here we will describe the mathematical details of the derivation.

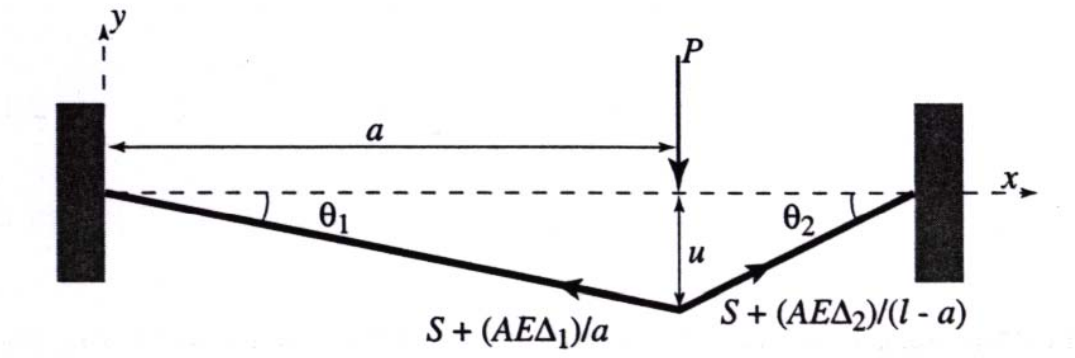

Fig. A1-1. Beam modelled as a stretched wire with concentrated vertical load *P* [14].

We will start from the point, where the applied force is equated to the vertical (transverse) components of the stress-induced force.

$$P = S_t^1 + S_t^2 \quad \text{(A1.1)}$$

From geometrical consideration (Fig. A1-1),

$$\left.\begin{aligned} S_t^1 &= \left(S + \frac{AE\Delta_1}{a}\right)\sin\theta_1 \\ \sin\theta_1 &= \frac{u}{\sqrt{a^2+u^2}} \end{aligned}\right\} S_t^1 = \left(S + \frac{AE\Delta_1}{a}\right)\frac{u}{\sqrt{a^2+u^2}}$$

$$\left.\begin{aligned} S_t^2 &= \left(S + \frac{AE\Delta_2}{a}\right)\sin\theta_2 \\ \sin\theta_2 &= \frac{u}{\sqrt{(l-a)^2+u^2}} \end{aligned}\right\} S_t^2 = \left(S + \frac{AE\Delta_2}{a}\right)\frac{u}{\sqrt{(l-a)^2+u^2}} \quad \text{(A1.2-A1.3)}$$

Now the stress components due to stretching are neglected

$$S_t^1 + S_t^2 = \frac{Su}{\sqrt{a^2+u^2}} + \frac{Su}{\sqrt{(l-a)^2+u^2}} \quad \text{(A1.4)}$$

Next, small *u* is assumed and the terms under root signs are simplified

$$\frac{Su}{\sqrt{a^2+u^2}}+\frac{Su}{\sqrt{(l-a)^2+u^2}}=Su\frac{l}{a(l-a)}=\frac{Sul}{a(l-a)}=P\Rightarrow$$
$$\Rightarrow u=\frac{Pa(l-a)}{Sl} \qquad \text{(A1.5)}$$

Finally, to find the deflection of the beam centre, similarity of triangles is used (Fig. A1-2)

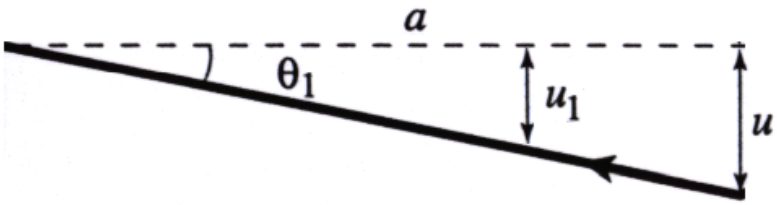

Fig. A1-2. Similar triangles from Fig. A1-1.

If u_1 is the deflection at the beam centre (at $l/2$) then taking the found expression for u into account

$$\frac{u_1}{u}=\frac{l/2}{a}\Rightarrow u_1=\frac{ul}{2a}=\frac{Pa(l-a)}{Sl}\frac{l}{2a}=\frac{P(l-a)}{2S} \qquad \text{(A1.6)}$$

And finally changing from u to y

$$y(l/2)=-\frac{P(l-a)}{2S} \qquad \text{(A1.7)}$$

Appendix 2. Buckling Modelling

A simple beam, which is clamped at both ends under compressive intrinsic stress σ_0, is studied (Fig. A2-1). Analytical (exact) formulas for the amplitudes w_0 are presented for the ground state [30]

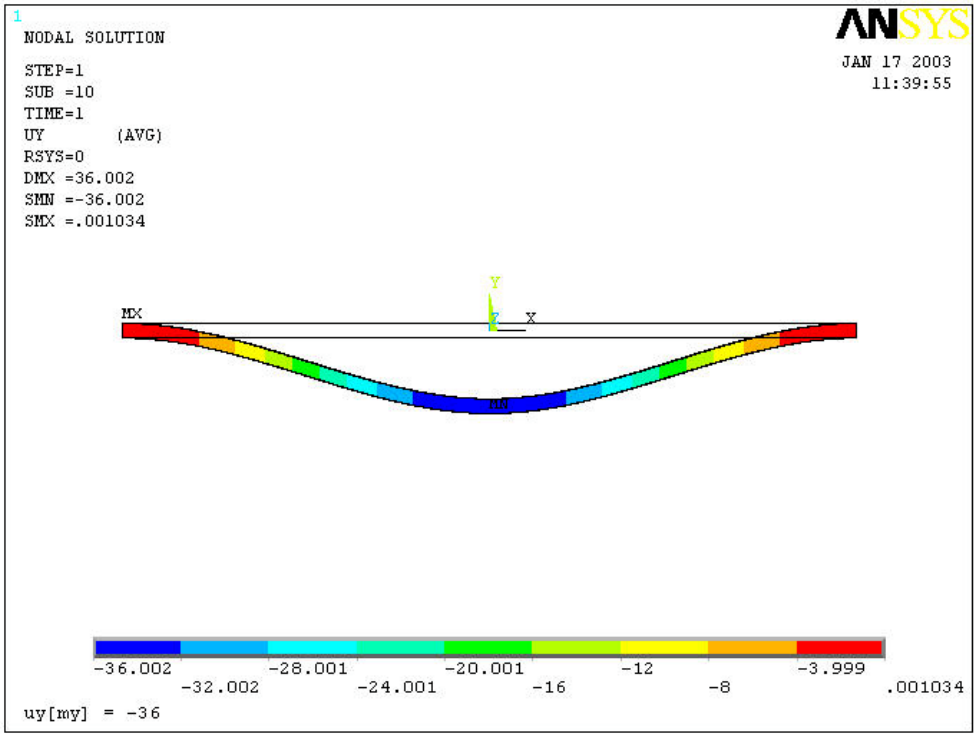

Fig. A2-1. Buckling of a beam under compressive stress. Screenshot of ANSYS FEM simulation. Colours correspond to different deflections, given in microns below [30]

The Bernoulli beam model is used to calculate the buckling behaviour of the beam. So one has to solve the differential equation for the lateral deflection y.

$$E\,I\,y''''(x) + F_a y''(x) = 0 \qquad \text{(A2.1)}$$

with the boundary conditions for a clamped beam are

$$y(\pm L/2) = y'(\pm L/2) = 0 \qquad \text{(A2.2)}$$

E is Young's elasticity modulus, $I = bt^3/12$ the area inertia moment of the beam's cross section, b is the width, t is the thickness of the beam (resp. the membrane). F_a is the axial force, i.e. the force, which the beam exerts onto the anchor points. F_a is an unknown quantity depending on the intrinsic stress σ_0 and the lateral deflection $y(x)$, F_a and σ_0 are defined positive for compressive stress.

A buckling solution is a nonzero solution of (Eqs. A2.1- A2.2), which is found for certain values of F_a, the first one, i.e. the solution with the lowest F_a, or ground state occurs for $\kappa = 2\pi$, where κ (kappa) is the dimensionless axial force

$$\kappa = L\sqrt{\frac{F_a}{E\,I}} \quad \text{(A2.3)}$$

For this ground state the deformation is:

$$y_0(x) = \frac{w_0}{2}\left(1+\cos\frac{2\pi\ x}{L}\right) \quad \text{(A2.4)}$$

The amplitude w_0 is calculated as

$$w_0 = \frac{2L}{\pi}\sqrt{\frac{\sigma_0}{E}-\frac{\pi^2 t^2}{3L^2}} = 0.6366\,L\sqrt{\frac{\sigma_0}{E}-3.290\frac{t^2}{L^2}} \quad \text{(A2.5)}$$

The result (Eq. A2.5) can be obtained using the stress-strain relation:

$$-\frac{F_a}{t\,b} = -\sigma = E\left(\varepsilon-\alpha\,\Delta T\right) = E\varepsilon-\sigma_0 \quad \text{(A2.6)}$$

Note that in our convention compressive stress is counted positive. In (Eq. A2.6) the strain ε is the relative length increase:

$$\varepsilon = \frac{\Delta L}{L} = \frac{1}{2L}\int_{L/2}^{L/2}(y_0'(x))^2\,dx = \frac{\pi^2\,w_0^2}{4L^2} \quad \text{(A2.7)}$$

Inserting Eq. A2.7 and A2.3 with $\kappa = 2\pi$ into Eq. A2.6 results into Eq. A2.5. An alternative method to derive Eq. A2.5 uses the principle, that the amplitude w_0 should minimise the elastic energy $U_{elastic}$, which has the form

$$U_{elastic} = \frac{EI}{2}\int_{-L/2}^{L/2} y_0''(x)^2 dx + \frac{L\,tb}{2}E\left(\varepsilon-\frac{\sigma_0}{E}\right)^2 \quad \text{(A2.8)}$$

Setting the derivative of $U_{elastic}$ in respect to w_0 to zero, leads again to the same result (Eq. A2.5) for the ground state amplitude w_0.

To have a non imaginary amplitude in Eq. A2.5, the intrinsic stress σ_0 must be larger than the critical stress

$$\sigma_{crit} = E\frac{\pi^2 t^2}{3L^2} \quad \text{(A2.9)}$$

Thus buckling occurs, if $\sigma_0 > \sigma_{crit}$. The critical stress has another property: it is the stress σ that in the buckled beam is present (see Eq. A2.6). This means that buckling leads to a reduction of the compressive stress from σ_0 *to* σ_{crit}.

Appendix 3. FEM Simulation

Here finite element modelling [30] of the parallel-plate varactor and the bridge-type S-shape varactor is described. Complete 3D structures (without perforation holes) as well as their simplifications are considered.

A3.1 Parallel-Plate Varactor

The bridge is suspended at the end of the suspension beams (see light blue markers in Fig. A3-1.). This suspension was intended to compensate for stress in the membrane due to thermal expansion. If instead the same membrane would be suspended at the ends of the membrane (a simple fixed-fixed bridge, modelled analytically in sections 6.2 and 7.3.1), the membrane can not so easily relax and the resulting collapse voltage would be considerably larger (or the stress - smaller). The stress is modelled as shrinkage of the structure upon homogeneous cooling. The effect of perforation holes is included into the material properties.

The stress compensation structures were optimised for the membrane length of 500 µm. For longer membranes the stress compensation works insufficiently leading to remaining tensile stress and larger collapse voltages. For shorter membranes the stress may be even overcompensated resulting into remaining compressive stress. For a membrane length of 450 µm this compressive stress even leads to buckling as can be seen in Fig. A3-1.

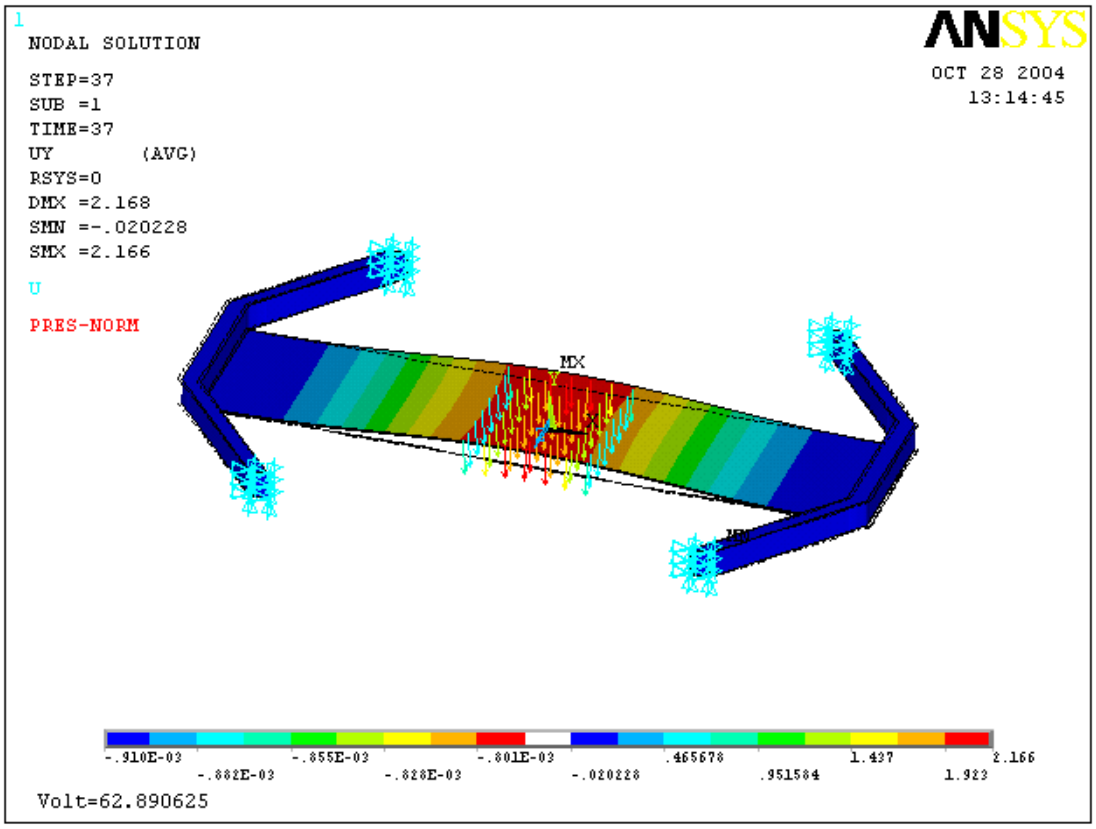

Fig.A3-1: Buckled parallel-plate varactor with membrane length 450 µm. The length of the arrows indicates the electrostatic force, which depend of the local gap. The intrinsic tensile stress here is –300 MPa.

Additionally to complete 3D model, also 3D fixed-fixed simple bridge was simulated (compare with Fig. A3-3). The results for the pull-down voltage at different stress levels are presented in Table A3-1.

Intrinsic tensile stress, MPa	**$V_{pull\text{-}down}$, V (stress compensating suspension)**	**$V_{pull\text{-}down}$, V (simple bridge)**
0	11.82	13.7
30	12.45	37.9
100	13.7	65.2
300	16.8	110
1000	23.8	198

Table A3-1. Stress-voltage data for parallel-plate varactor with membrane length 500 μm.

One observes that the collapse voltage for the complete model is nearly independent of intrinsic stress. This has as a consequence that there exists no intrinsic stress which would lead to collapse voltage of 46 V (see section 6.3), at least at reasonable values below 1000 MPa. Results for the simple bridge model are similar to those obtained through analytical calculation.

The conclusion is that either some material properties or the stress level (thermal history in terms of the simulation) are different for the membrane and for the suspension structures (they were assumed to be the same in the complete model simulation).

A3.2 Bridge-Type S-shape Varactor

The bridge-type S-shape varactor was modelled similar to the parallel-plate varactor (Fig. A3-2). As mentioned above, the compensation structure did not compensate the tensile stress in the membrane due to the membrane length different from the optimal one.

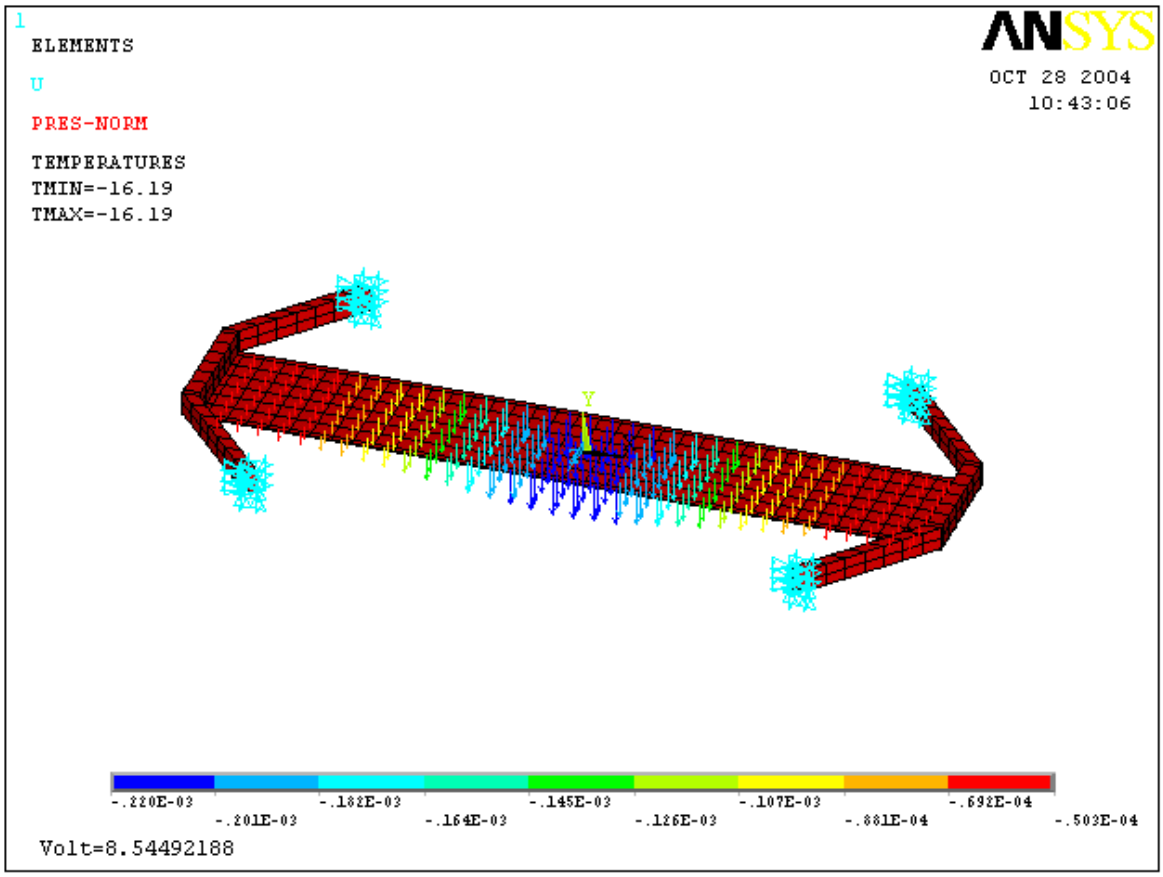

Fig. A3-2. Bridge-type S-shape varactor with membrane length 600 µm. The plot shows the bridge beginning to collapse, the length of the arrows indicate the electrostatic force, which depend of the local gap.

In the shown example the intrinsic stress was -30 MPa, which corresponds to ΔT =-16 degrees centigrade leading to a shrinkage, the applied voltage was 8.5 V. For a simple fixed-fixed bridge (Fig. A3-3) FEM simulation gives pull-down voltage of 20.2 V at –30 MPa, which is similar to the analytical results (see section 7.4.1).

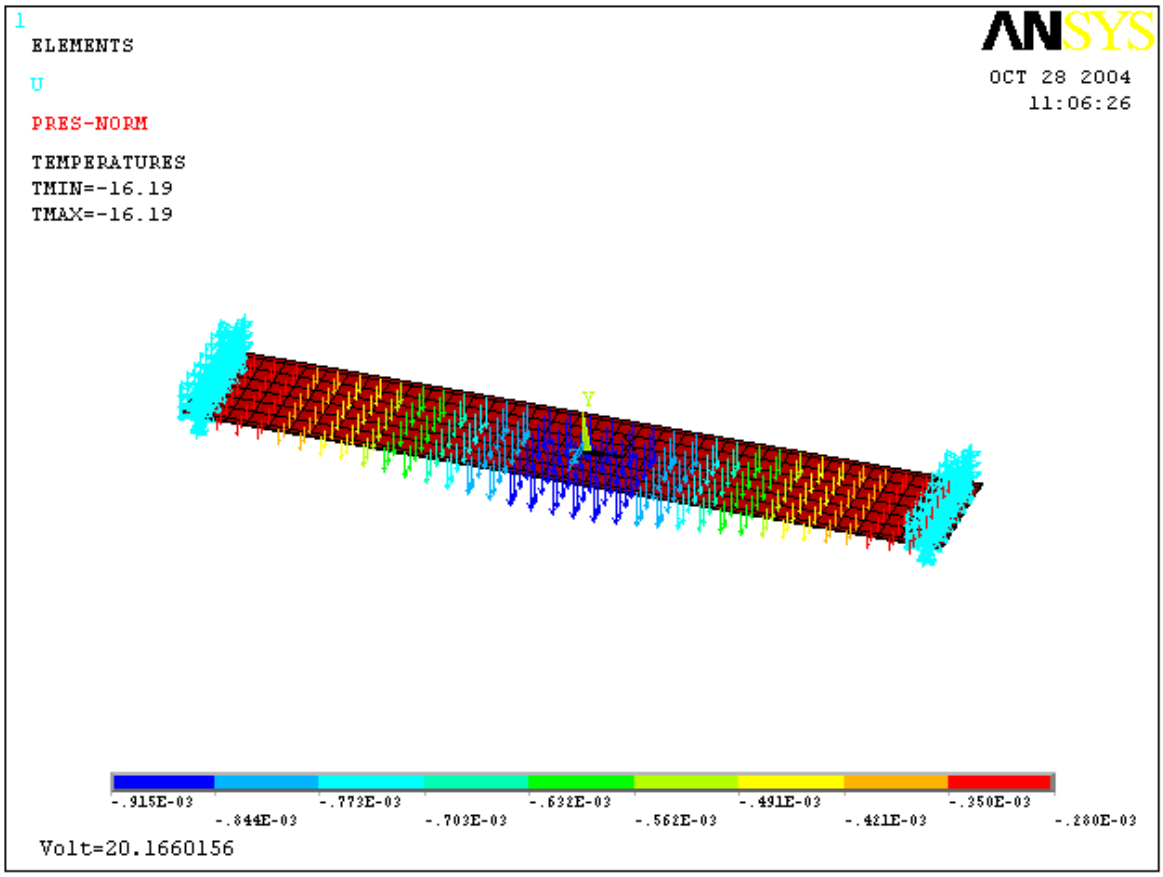

Fig. A3-3. Bridge-type S-shaped varactor modelled as a simple fixed-fixed bridge.

Stress-voltage data for the bridge-type varactor are summarised in Table A3-2.

Intrinsic tensile stress, MPa	**$V_{pull\text{-}down}$, V (stress compensating suspension)**	**$V_{pull\text{-}down}$, V (simple bridge)**
0	5.9	6.8
30	8.5	20.2
300	20.1	59.1

Table A3-2. Stress-voltage data for S-shaped varactor with membrane length 600 µm.

We could also obtain a CV curve for this varactor type (Fig. A3-4). The stress here is set to 300 MPa. There is only qualitative similarity of the modelled curve to the experimental one, probably due to the reasons already mentioned in section 7.3.1.

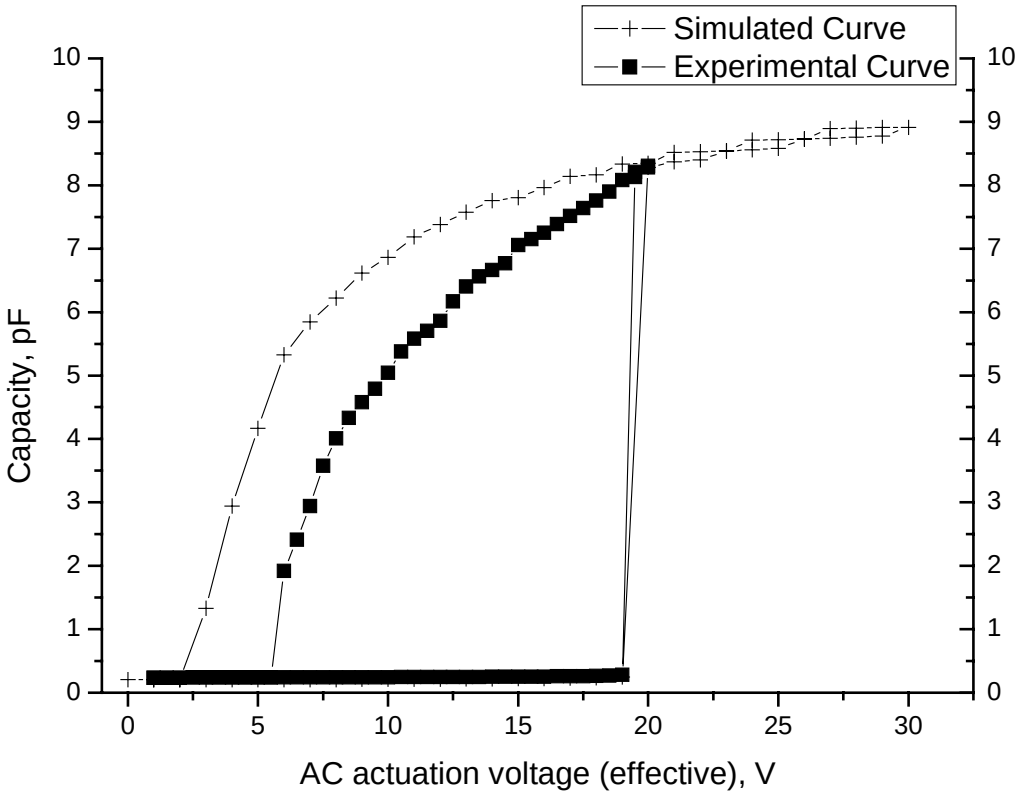

Fig. A3-4. Comparison of the simulated CV-curve with the experimental one.

The final conclusion is that FEM simulation of the complete structures meets difficulties. They are probably related to inhomogeneous stress distribution in the structure or difference in material properties between the membrane and the suspension structures. Additional difficulty is posed by the complicated mechanical restoring force for the membrane in intimate contact with a dielectric layer. It is actually not well understood due to adhesion and repulsion forces between the metal and dielectric layers.

Literature

[1] P. Collander, Packaging Technologies Cellular Phones, Adv. Microelectron., 26, 1999, pp. 13-16

[2] P. Mannion, Cellular/PCS Systems Take the Globe by Storm, Electron. Des., September 1999, pp. 63-68

[3] N. Pulsford, Passive Integration Technology: Targeting Small Accurate RF Parts, RF Des., November 2002, pp. 40-48

[4] H. A. C. Tilmans, W. De Raedt, and E. Beyne, MEMS for Wireless Communications: "From RF-MEMS Components to FR-MEMS-SiP", J. Micromech. Microeng., 13 (2003), pp. 139-163

[5] G. van de Walle, Integration of Passive components: an Introduction, Philips J. Res., 51-3, 1998, pp. 353-361

[6] R. R. Tummala, et al. SoP: The Microelectronics for The 21st Century with Integral Passive Integration, Adv. Microelectron., 27, 2000, pp. 13-19

[7] P.R. Gray and R.G. Meyer, Future Directions in Silicon ICs for RF Personal Communications, IEEE Custom Integrated Circuits Conf. (Santa Clara, CA), 1995, pp.83-90

[8] C. T.-C. Nguyen, Transceiver Front-End Architectures Using Vibrating Micromechanical Signal Processors, Dig. of papers Topical Meeting on Silicon Integrated Circuits in RF Systems, 12-14 September 2001, pp. 23-32

[9] N. Maluf, An Introduction to Microelectromechanical Systems Engineering, Artech House Publishers, 2000

[10] M. Madou, Fundamentals of Microfabrication, CRC Press, 1997

[11] H. De Los Santos, Introduction to Microelectromechanical (MEM) Microwave Systems, Artech House Publishers, 1999

[12] D. J. Young, MicroElectroMechanical Devices and Fabrication Technologies for Radio-Frequency Analog Signal Processing, PhD thesis, University of California, Berkeley, 1999

[13] E. Pedersen, RF CMOS Varactors for Wireless Applications, Industrial PhD thesis, Aalborg University, 2001

[14] G. M. Rebeiz, RF MEMS. Theory, Design, and Technology, John Wiley and Sons, 2003

[15] MELODICT (Micromachined Electromechanical Devices for Integrated Wireless Communication Transceivers) project, EU Funded, IST-1999-10945, 2000

[16] J.-B. Yoon and C. T.-C. Nguyen, A high-Q tunable micromechanical capacitor with movable dielectric for RF applications, Technical Digest, IEEE Int. Electron Devices Meeting, San Francisco, California, Dec. 11-13, 2000, pp. 489-492.

[17] J. J. Jao, S. Park and J. DeNatale, High Tuning Ratio MEMS Based Tunable Capacitors for RF Communications Applications, Proceedings of Solid-State Sensors and Actuators Workshop, pp. 124-127, 1998

[18] S. Seok, W. Choi, and K. Chun, A Novel Linearly Tunable MEMS Variable Capacitor, J. Micromech. Microeng., No. 12, pp. 1-5, 2002

[19] H. Nieminen et al., Microelectromechanical Capacitors for RF Applications, J. Micromech. Microeng. 12 (2002) S 1-10

[20] A. Dec and K. Suyama, Micromachined Electro-Mechanically Tunable Capacitors and Their Applications to RF IC's, IEEE Transactions on Microwave Theory and Techniques, Vol. 46, No. 12, December 1998

[21] J. Zou, Ch. Liu, J. Schutt-Aine, J. Chen, and S.-M. Kang, Development of a Wide Tuning Range tunable Capacitor for Wireless Communication Systems, Technical Digest of International Electron Devices Meeting, pp.403-6, 2000

[22] G. V. Ionis, A. Dec, and K. Suyama, "A Zipper-Action Differential Micro-Mechanical Tunable Capacitor", Proceedings of MEMS Conference 2001, August 24-26, Berkeley, USA

[23] J. R. Gilbert and S. D. Senturia, Two-Pahse Actuators: Stable Zipping Devices Without Fabrication of Curved Structures, Proceedings of Solid-State Sensor and Actuator Workshop, pp. 98-100, June 1996

[24] Z. Feng, H. Zhang, K. C. Gupta, W. Zhang, V. M. Bright, and Y. C. Lee, MEMS-Based Series and Shunt Variable Capacitors for Microwave and Millimeter-Wave Frequencies, Sensors and Actuators A Vol. 91, pp.256-265, 2001

[25] J. Y. Park, Y. J. Lee, H. J. Nam, and J. U. Bu, Micromachined RF MEMS Tunable Capacitors Using Piezoelectric Actuators, in Proceedings of IEEE MTT-S Symposium, Vol.3, pp.2111-2114, May 2001

[26] F. De. Flaviis, D. Chang, N. G. Alexandropoulos, and O. M. Stafsudd, High Purity Ferroelectric Materials by Sol-Gel Process for Microwave Applications, IEEE MTT-S International Microwave Symposium Digest, vol.1, p.99-102, 1996

[27] R. Ott and R. Wördenweber, Improved designs of tunable ferroelectric capacitors for microwave applications, Applied Physics Letters, vol.80, no.12, p.2150- 2, 25 March 2002

[28] S. W. Kirchoefer et al., Microwave Properties of Sr0.5Ba0.5TiO3 Thin Film Interdigitated Capacitors, Microwave and Optical Technology Letters 18(3): 168-171, 1998

[29] R. L. Borwick et al., A High-Q, Large Tuning Range, Tunable Capacitor for RF Applications, in IEEE International Conference on Microelectromechanical Systems, January, 2002, pp. 669-672

[30] Dr. M. Weiss, FhG ISiT, private communication

[31] N. Hoivik, M. A. Michalicek, Y. C. Lee, K. C. Gupta, V. M. Bright, Digitally Controllable Variable High-Q MEMS Capacitor for RF Applications, IEEE MTT-S International Microwave Symposium Digest Piscataway, NJ, USA, vol.3, pp.2115-18, 2001

[32] E. S. Hung and S. D. Senturia, Extending the Travel Range of Analog-Tuned Electrostatic Actuators, J. of Microelectromechanical Systems, VOL. 8. NO. 4, December 1999

[33] B. Yaworsky and A. Detlaf, Handbook on Physics, Physical and Mathematical Literature Publishing Company, Russian Academy of Sciences, 1996 (in Russian)

[34] L. D. Landau and E. M. Lifshitz, Theory of Elasticity 7, Physical and Mathematical Literature Publishing Company, Russian Academy of Sciences, 2001 (in Russian)

[35] R. J. Roark and W. C. Young, Formulas for Stress and Strain, 6th edition, McGraw-Hill, New York, 1989

[36] C. H. Mastrangelo and C. H. Hsu, Mechanical Stability and Adhesion of Microstructures Under Capillary Forces – Part I: Basic theory, J. of Microelectromechanical Systems, VOL. 2, NO. 1, March 1993

[37] C. H. Mastrangelo and C. H. Hsu, Mechanical Stability and Adhesion of Microstructures Under Capillary Forces – Part II: Experiments, J. of Microelectromechanical Systems, 2, 1, March 1993

[38] J. Wibbeler, G. Pfeiffer, and M. Hietschold, Parasitic Charging of Dielectric Surfaces in Capacitive Microelectromechanical Systems (MEMS), Sensors and Actuators A, 71 (1998), 74-80

[39] W. M. van Spengen, R. Puers, and I. De Wolf, A Physical Model to Predict Stiction in MEMS, J. Micromech. Microeng., 12 (2002) 702-713

[40] M. Hill et al., Performance and Reliability of Post-CMOS Metal/Oxide MEMS for RF Application, J. Micromech. Microeng., 13 (2003) 131-138

[41] W. M. van Spengen, MEMS Reliability. Stiction, Charging and RF MEMS, PhD thesis, Catholic University Leuven, Belgium, 2004

[42] Dr. H. Bernt, FhG ISiT, private communication.

[43] E. H. Nicollian, J. R. Brews, MOS (Metal Oxide Semiconductor) Physics and Technology, John Wiley & Sons, 1982

[44] Keithley Model 595 Quasistatic CV Meter, Instruction Manual, 1986

[45] Dr. T. Lisec, FhG ISiT, private communication

[46] MELODICT documentation, Deliverable 5, 2001

[47] U. Hofmann et al., SPIE proceedings; Vol. 3878; 1999; page 29 –38

[48] J. R. Gilbert and S. D. Senturia, Two-Phase Actuators: Stable Zipping Devices without Fabrication of Curved Structures, Solid-State Sensor and Actuator Workshop, June 1996, Hilton Head S.C. pp. 98-100

[49] F. Yang, Contact Deformation of a Micromechanical Structure, J. Micromech. Microeng., 14 (2004) 263-268

[50] J.-N. Ding, S.-Z. Wen, and Y.-G. Meng, Theoretical Study of the Sticking of a Membrane Strip in MEMS under the Casimir Effect, J. Micromech. Microeng., 11 (2001) 202-208